Single and Dual-Wavelength Lasing in the 800-820 nm and 1460-1520 nm Bands in a Tm:ZBLAN Fibre Laser

Blaise Frison

Master of Engineering

Department of Electrical and Computer Engineering

McGill University

Montreal, Quebec

December 14th 2012

A thesis submitted to McGill University in partial fulfillment of the requirements of the degree of Master of Engineering

DEDICATION

I dedicate this work to my late grandfather, Lionel. His courage and determination will be an inspiration for my whole life.

ACKNOWLEDGEMENTS

First of all, I would like to thank my professor, Lawrence, for his guidance, assistance and patience. I have learned a great deal with his help.

I would also like to thank OE-land for the material and the help they provided for my research.

I have received inestimable help from my colleagues in the Photonics System's Group. I would like to thank Abdul for teaching me the basic skills of fibre handling and for assisting me in many experiments. I also extend my gratitude to Philip, whose dedication, time and ingenuity made my experiments possible. Finally, I want to thank Chams who gave me much advice.

I am grateful to my family who helped me and supported me in my difficult moments. I thank my mother and father, Anne and Philippe, for their presence and their support. I would like to thank my sister, Héloïse, for sharing her experience and accompanying me in my efforts. I thank Kevin for being a good friend. I thank my grandmother Françoise for her kindness and presence.

I thank Lu for listening to my worries and encouraging me.

I thank Susan for making me smile and forget everything about my research when I needed it.

ABSTRACT

Tm^{3+} ions provide amplifications in a wide variety of wavelength bands, including 480 nm, 810 nm, 1480 nm, 1900 nm, and 2300 nm. This thesis presents the characteristics of lasers fabricated with Tm:ZBLAN fibre as the gain medium.

First, a single wavelength linear cavity fibre laser at 810 nm is presented. Dual-wavelength lasing and bistable behaviour are demonstrated in single cavity lasers, while dual-wavelength lasing, bistable behaviour and wavelength switching are demonstrated in cascaded cavity lasers.

Second, single wavelengths fibre lasers at 1480 nm in linear and ring cavities are presented. A maximum power of 340 mW at 1476 nm was obtained. Dual-wavelength lasing at 1476 nm and 1487 nm is shown in cascaded cavity lasers.

Finally, using bi-directional pumping in a cascaded cavity, dual wavelength lasing at 1487 nm and 1487.6 nm, with a record narrow spacing of 0,6 nm, is achieved.

ABRÉGÉ

Le gain des ions de Tm^{3+} peut être utilisé dans un variété de bandes de longueurs d'ondes, incluant entre autres 480 nm, 810 nm, 1480 nm, 1900 nm et 2300 nm. Ce mémoire présente les caractéristiques de lasers fabriqués avec des fibres de Tm:ZBLAN comme médium de gain.

Premièrement, un laser à fibre à longueur d'onde simple à 810 nm, fabriqué avec une cavité linéaire est présenté. Une oscillation à longueurs d'ondes doubles et une opération bistable sont démontrées dans des lasers à cavités simples, puis une oscillation à longueurs d'ondes doubles, une opération bistable et une inter-version de longueur d'onde sont démontrées dans des lasers à cavités en cascade.

Ensuite, des lasers à fibre à longueurs d'ondes simples à 1480 nm, dans des cavités linéaires et annulaires sont présentés. Un maximum de 340 mW à 1476 nm a été obtenu. Des oscillations à 1476 nm et 1487 nm, obtenues avec des lasers à cavités en cascade, sont montrés.

Finalement, un laser à 1487 nm et 1487,6 nm, avec l'aide d'une cavité en cascade pompée bi-directionnellement, est démontré, atteignant un écart record de 0.6 nm.

TABLE OF CONTENTS

DEDICATION ii

ACKNOWLEDGEMENTS iii

ABSTRACT iv

ABRÉGÉ v

LIST OF TABLES ix

LIST OF FIGURES x

1 Introduction 1

2 Ion Doping 4

2.1 Glasses 4
2.1.1 Definition 4
2.1.2 Glass Stability 5
2.1.3 Ion doping 6
2.1.4 Comparison with Crystals 7
2.2 Rare Earths 7
2.2.1 Introduction 7
2.2.2 Electronic Transitions 8
2.2.3 Spectral Broadening 10
2.2.4 Energy Level Decay Rates 11
2.2.5 Doping Methods 13
2.2.6 Properties of Some Ions 14
2.3 Conclusion 26

3 Fibre Fabrication 27

3.1 Fibre Bragg Gratings 27
3.1.1 Introduction 27

3.1.2 Silica based FBGs . . . 28
3.1.3 Fluoride based FBGs . . . 31
3.1.4 Conclusion . . . 33
3.2 Fibre Materials . . . 33
3.2.1 Silica . . . 33
3.2.2 ZBLAN . . . 36
3.2.3 Chalcogenides . . . 41
3.2.4 Tellurite . . . 42
3.3 Fabrication Methods . . . 43
3.3.1 Silica Fibres Fabrication . . . 43
3.3.2 Fluoride Glass Synthesis . . . 45
3.3.3 Fluoride Fibre Fabrication . . . 48
3.4 Conclusion . . . 51

4 Lasing at 810 nm . . . 52

4.1 Introduction . . . 52
4.2 Applications . . . 52
4.2.1 First window of telecommunications . . . 52
4.2.2 Terahertz Generation . . . 54
4.3 Experimental Methodology . . . 55
4.4 Amplified Spontaneous Emission . . . 57
4.5 Lasing Investigation Methodology . . . 58
4.6 Single Wavelength Lasing . . . 60
4.6.1 Configuration . . . 60
4.6.2 Results . . . 62
4.7 Dual-wavelength lasing . . . 64
4.7.1 Configurations . . . 64
4.7.2 Results . . . 65
4.8 Conclusion . . . 70

5 Lasing at 1480 nm . . . 72

5.1 Introduction . . . 72
5.2 Applications . . . 75
5.2.1 Extension of the Third Window into the S-band . . . 75
5.2.2 Pumping EDFAs . . . 75
5.2.3 Terahertz Generation . . . 76
5.3 Amplification . . . 77

5.3.1 Methodology 77
5.3.2 Spectral measurements 78
5.3.3 Gain characteristics at 1460 nm 84
5.3.4 Conclusion 84
5.4 Single wavelength lasing 87
5.4.1 Methodology 87
5.4.2 Ring Cavity Lasers 89
5.4.3 Linear Cavity Lasers 90
5.4.4 Optimized Linear Cavity Laser 92
5.4.5 Summary 93
5.5 Dual-Wavelength Lasing 95
5.5.1 Methodology 95
5.5.2 Dual-Wavelength Lasing at 1476 nm and 1487 nm 95
5.5.3 Dual-Wavelength Lasing at 1487 and 1487.6 nm 99
5.6 Conclusion 104

6 Conclusion and Future Work 106

References 109

LIST OF TABLES

Table		page
2–1	Electronic transitions of the Er^{3+} ion	15
2–2	Electronic transitions of the Tm^{3+} ion	20
2–3	Electronic transitions of the Nd^{3+} ion	24
4–1	Comparison between three short-reach communications methods.	53
4–2	Cross sections of various absorption transition of Tm^{3+} in ZBLAN host.	58
4–3	Output characteristics of the third telecommunication window lasers that have been tested.	70
5–1	Output characteristics of the various S-band lasers that have been tested.	94

LIST OF FIGURES

Figure page

2–1 Energy levels of the Er^{3+} ion. 16

2–2 Energy levels of the Tm^{3+} ion. 21

2–3 Visible emission from Tm^{3+} ions. 23

2–4 Energy levels of the Nd^{3+} ion. 25

2–5 Energy levels of the Yb^{3+} ion. 26

4–1 A mechanical splicing between a length of SMF-28 and a length of Tm:ZBLAN fibre. 56

4–2 Configuration used to measure the ASE from the Tm:ZBLAN fibre . 57

4–3 ASE obtained by pumping 22.5 cm of Tm:ZBLAN fibre with 17 mW at 790 nm. 58

4–4 ASE obtained by pumping 1.1 m of Tm:ZBLAN fibre at 1064 nm. . . 60

4–5 Linear cavity configuration used to achieve single wavelength lasing. 61

4–6 Output power obtained with 43 cm of Tm:ZBLAN with a linear cavity. 63

4–7 Spectra obtained from the laser shown in Fig. 4–5. 63

4–8 Dual-wavelength fibre laser configurations 64

4–9 Hysteresis behaviour of the output power of the single cavity configuration shown in Fig. 4–8a. 65

4–10 Evolution of the output spectrum of the single cavity as a function of P_{pump}. 66

4–11 Hysteresis behaviour of the output power of the cascaded cavity configuration shown in Fig. 4–8b. 67

4–12 Output powers obtained for both wavelengths with the cascaded cavity configuration. 68

4–13 Evolution of the output spectrum of the cascaded cavity as a function of P_{pump}. 69

5–1 Spectrum of the $^3F_4 \rightarrow ^3F_2$ ESA in Tm:ZBLAN. 74

5–2 GSA spectrum of Tm:ZBLAN. 74

5–3 Gain spectra for various lengths of EDFAs 76

5–4 Configuration that was used to measure the gain of various lengths of Tm:ZBLAN. 78

5–5 Gain spectra for various lengths of Tm:ZBLAN at P_{input} = -31.8 dBm. 79

5–6 Absorption and emission spectra of Tm:ZBLAN 80

5–7 Spectrum for the 85 cm length of Tm:ZBLAN fibre with P_{pump} fixed at 2090 mW 82

5–8 Gain for the 85 cm length of Tm:ZBLAN fibre pumped at 2090 mW, as a function of P_{input}. 83

5–9 Gain at λ_{signal} = 1460 nm as a function of P_{pump} for various length of Tm:ZBLAN fibre. 85

5–10 Gain at λ_{signal} = 1460 nm as a function of P_{signal} for various length of Tm:ZBLAN fibre. 86

5–11 Wavelength dependance of the low-signal gain increase for 85 cm and 105 cm lengths of fibre. 87

5–12 Ring cavity laser configurations. 88

5–13 Linear cavity laser configurations. 89

5–14 Output power obtained with the ring cavity laser. 90

5–15 Output power obtained with the linear cavity lasers. 91

5–16 Optimized laser configuration used to optimize the output power. . . 92

5–17 Output power graphs of the optimized linear cavity laser configuration. 93

5–18 S-band cascaded cavity dual-wavelength configurations. 96

5–19 Output power and spectrum of the S-Band cascaded cavity laser configuration with 20 cm and 40 cm lengths of Tm:ZBLAN fibre. . 97

5–20 Hysteresis behaviour of the S-band cascaded cavity configuration with 30 cm and 80 cm lengths of Tm:ZBLAN fibre. 98

5–21 Setup for stretched FBG 99

5–22 Regions of oscillations as a function of both pump powers. 100

5–23 Spectra measured during the first set of measurements done with the cascaded cavity configuration at 1487 and 1487.6 nm 101

5–24 Observed thresholds from the cascaded cavity configuration at 1487 and 1487.6 nm 102

5–25 Spectra measured during the second set of measurements done with the cascaded cavity configuration at 1487 and 1487.6 nm . . . 103

CHAPTER 1
Introduction

Lasers have played a vital role in the development of telecommunications during the previous decades. Lasers can emit light with a narrow linewidth and precisely controlled wavelength and focus this light in a specific direction. A narrow linewidth is an important parameter in establishing a coherent communication system and serves to decrease the impact of dispersion, while control over the direction of light helps for coupling the light into a fibre and therefore improve the energy efficiency.

More especially, lasers can be implemented using all-fibre configurations. This of course allows for an easy integration of light sources into fibre networks. Furthermore, single-mode fibre lasers can generate beams with a very good quality, which propagates over long distance in free-space.

The shape of a fibre, with a very large surface to volume ratio, ensures a good heat dissipation and therefore contributes to the high output power limit of fibre lasers. Fibre lasers, since they provide gain through rare earth ions dissolved in a glass host, possess a larger gain bandwidth than lasers with crystal hosts, which is useful both for wavelength tuning and short pulse generation. The rare earth ions which are used in the making of fibres undergo a limited influence from the host, as the electronic transitions involved in optical interactions occur in the 4f shell, which is partially shielded from outside influence by the electrons in outer shells.

This work will focus more specifically on one lanthanide ion, trivalent thulium, and its use as a doping agent in a fluorozirconate glass host called ZBLAN to provide lasing and amplification. Tm, number 69 on the periodic table, has the electronic configuration [Xe]$4f^{13}6s^2$ in its neutral form, and [Xe]$4f^{12}$ in its trivalent form. In the near infra-red region, it can provide gain at 810 nm and 1480 nm.

810 nm is situated in the first telecommunications window, which was used in the 1970's, using GaAs laser diode sources [1]. Even though attenuation in silica glass fibres is greater in the first telecommunications window than in the third window, i.e., at 1550 nm, fibres can be used to transmit signals in the first window for short-reach communication applications. Dual-wavelength lasing, bistable behaviour and wavelength switching at 805 nm and 810 nm in Tm:ZBLAN fibre lasers are presented.

1480 nm corresponds to the S-band of the third communication window, where the amplification provided by erbium doped fibre amplifiers(EDFAs) is significantly lower in value. 1480 nm can also be used to excite the $^4I_{13/2}$ energy level of the Er^{3+} ion, which provides gain at 1550 nm through the $^4I_{13/2} \rightarrow {}^4I_{15/2}$ transition. Dual-wavelegnth operation of cascaded cavity Tm:ZBLAN fibre lasers, at 1476 nm and 1487 nm, and at 1487 nm and 1487.6 nm, which is a record narrow spacing, are demonstrated.

The remainder of this thesis is organized as follows. First, rare earth ion doping will be discussed in chapter 2. The chapter will focus on the properties of glass in its first part and will discuss rare earth ions in its second part. In chapter 3, the fabrication of fibre lasers will be presented. The properties and fabrication

methods of fibre Bragg gratings (FBGs) will first be presented, followed by a discussion on materials that can be used for fibres. The fabrication methods for silica and fluoride fibres will then be explained. The results of experimentation on Tm:ZBLAN fibre lasers and amplifiers will be shown in chapters 4 and 5. Chapter 4 will focus on single and dual-wavelength lasing in the 800-820 nm band, where amplification is provided by the $^3H_4 \rightarrow {}^3H_6$ transition, while chapter 5 will present amplification and both single and dual-wavelength lasing in the 1460-1520 nm band, where the gain is provided by the $^3H_4 \rightarrow {}^3F_4$ transition.

The results of dual-wavelength lasing have been reported in the following conference publications:

B. Frison, A. R. Sarmani, L. R. Chen, X. Gu, S. Thomas, P. Long, M. Saad. "Dual-wavelength lasing around 800 nm in a Tm:ZBLAN fibre laser," in *IEEE Photonics Conference*, Sep. 2012, pp. 668-669.

B. Frison, A. R. Sarmani, L. R. Chen, X. Gu, M. Saad. "Multi-wavelength S-band Tm:ZBLAN fiber lasers," in *Photonics West*, Feb. 2013.

CHAPTER 2
Ion Doping

This chapter will first describe the properties of vitreous solids, also called glasses, and their role in fibre lasers. In the second part, the properties of rare earth ions, which are commonly used as doping agents to provide gain in fibre lasers, will be presented. The various phenomena that can affect their properties, such as their spectra, will be discussed. Ion doping techniques used in the fabrication of fibres will be introduced, followed by a few examples of lasing transitions in the most commonly used ions.

2.1 Glasses

2.1.1 Definition

Glasses are amorphous solid materials exhibiting a glass transition [2]. They are distinguished from crystals by the lack of long range order among their particles. However, glass particles are ordered on a local scale. For example, the glass former for silica is a SiO_4^{2-} tetrahedron, which shares its oxygen corners with its neighbours. It is the variations in length and angle of the bonds between the elementary units of glass that disrupt long range order.

Glasses are not a thermodynamically stable state; they undergo spontaneous crystallization, also called devitrification. The rate of crystallization of a material, however, varies widely over temperature, i.e., it decreases as the temperature is lowered. Below a certain temperature, no crystallization can be observed on a

practical time scale. A glass is formed by cooling a liquid fast enough so that crystallization does not have time to occur when the rate is relatively high. The highest temperature where a mix of crystals and liquid can exist at equilibrium is called the liquidus temperature.

Glasses do not possess a unique melting point like crystals do; the viscosity of a glass varies gradually as the temperature is changed, in a phenomenon called glass transition. The viscosity of a material below the liquidus point has a strong effect on its crystallization rate. A high viscosity slows down the rate at which the particles are able to organize themselves in a crystalline structure. The narrow temperature region between the point where viscosity is high enough for the material to solidify and the one where the material starts flowing at a noticeable rate is called the glass transition temperature [2].

2.1.2 Glass Stability

Particles can act as network formers or network modifiers in a glass. Network formers are responsible for the main structure of the glass while modifiers alter the structure of a glass. For example, adding Al_2O_3 as a network modifier to SiO_2 increases the viscosity of the silicate glasses and therefore decreases the crystallization rate.

Two figures of merit can be used to describe glass stability: the minimum critical cooling rate needed to avoid crystallization and the Hruby factor, which corresponds to the difference between the lowest temperature at which crystallization occurs (T_x) and the glass transition temperature (T_g), divided by the difference between the liquidus (T_l) and the crystallization temperature:

$$Hruby factor = \frac{T_x - T_g}{T_l - T_x} \tag{2.1}$$

Alternatively, $T_x - T_g$ can also serve as figure of merit.

2.1.3 Ion doping

Glasses and crystals possess different characteristics when used as hosts for ions in a laser. On a local scale, the electric fields that are due to host particles and which affect ions can be modelled as crystal fields. However, the exact characteristics of the field surrounding an arbitrary ion depend randomly on the position of the ion in the glass. The statistical variations of the ions' environment create an inhomogenous broadening of the ions' absorption and emission spectra. The linewidth of electronic transition involving ions in suspension in a glass host typically reach a few tens of nanometres. This property can be exploited when designing wavelength tunable lasers. On the other hand, ions in suspension in a crystal host are under the influence of similar fields regardless of position; the smaller variation of local conditions mean much sharper transition spectra, typically of the order of a few nanometres.

Active ions dissolved in a glass act either as network modifiers, or are situated in interstitial spaces between network formers. A high concentration of ions can cause a decrease in the lifetime of excited levels of dissolved ions through a quenching process. This process consists in an non-radiative cross-relaxation between ions which are situated at short distances from each other. An increase of the crystallization rate can also be caused by a high concentration of ions in

a glass, which ultimately leads to a decrease of the glass stability. For example, lanthanide ions, which are larger than the SiO_4^{2-} glass former in silica, break the amorphous structure of silica glass [3].

2.1.4 Comparison with Crystals

The broader spectra of glass lasers make them more suited for pulsed lasers, while crystal lasers enjoy higher cross section within their narrowly defined transitions, making them more suited for continuous wave applications. The generally high thermal conductivity of crystal lasers is useful when designing high power lasers.

The grain boundaries of a polycrystal causes scattering of light, reducing substantially the transmission of the crystal host. Monocrystals are therefore preferred in laser applications. However, the need for monocrystals limits the size of the devices; for this reason glasses allow the fabrication of devices of a larger scale.

2.2 Rare Earths

2.2.1 Introduction

According to the International Union of Pure and Applied Chemists (IUPAC), the term *rare earth* is used to designate elements 57 (La) to 71 (Lu) plus Sc and Y. The term *lanthanides* decribes elements 58 (Ce) to 71(Lu) while *lanthanoids* is used for elements 57 to 71; however lanthanides is often used in the literature to denominate elements 57 to 71. In this thesis, lanthanides will be used with the latter meaning. Lanthanides are known for having very similar chemical characteristics, due to their analogous valence layer configuration. This configuration corresponds to

[Xe]$4f^n6s^2$, where n varies between different lanthanides. The same valence layer of all lanthanides, $6s^2$, explain the similarity of their chemical characteristics.

The particularity of lanthanides is that they possess an incomplete subshell, $4f$, which is situated closer to the core than the valence layer. The electrons in the $4f$ subshell are not implicated in bonding with nearby atoms; they are therefore partially shielded from influence from the local environment. Electrons are free to move between different energy levels of the incomplete $4f$ subshell and these tranistions possess therefore sharply defined energies. In a glass host, trivalent lanthanide ions lose the two $6s$ electrons plus one from the $4f$ subshell. The $5s$ and $5p$ subshells stay intact and their shielding effect on $4f$ electrons remains effective. The transition spectra of lanthanide ions dissolved in a glass are therefore similar to their free ion spectra.

Transition metals (Sc, Ti, V, Cr, Mn, Fe, Co, Ni, Cu, Zn), on the other hand, are not subject to the same shielding phenomenon as lanthanide ions when dissolved in a glass. In their oxidized forms, transition metals lose their $4s$ valence layer and expose directly the incomplete $3d$ subshell to the local crystal field. Transition metals ions in glass hosts therefore have broader spectral lines than lanthanide ions.

2.2.2 Electronic Transitions

According to Laporte's selection rule, electric dipole transitions in centrosymmetric atoms can only occur between two states if their parity is different. A state is said to have g (from the German *gerade*, meaning even) if a point reflection of the wavefunction causes no phase change, and it is said to be u (from *ungerade*,

meaning odd) if a point reflection of the wavefunction would induce a π phase shift. For f states, u parity is observed. This means that according to Laporte's selection rule, $f - f$ transitions are forbidden.

Van Vleck has postulated in 1937 [4] that odd order terms in the crystal field affecting ions cause a parity mixing of $4f$ states with states of higher principal quantum number n, such as states in the $5d$ subshell. In other words, the centrosymmetry of the electrons' wavefunctions is broken by asymmetrical fields, so that transitions which would be forbidden in free ions are weakly allowed in such electric fields.

Several phenomena cause the break of degeneracy between the different $4f$ electronic states in a lanthanide ion. The electrostatic repulsion between electrons causes a split of different **SL** terms (**S** and **L** correspond to the values the spin angular momentum and the orbital angular momentum, respectively) of the order of ~ 10^4 cm^{-1}. The spin-orbit interaction causes further separation between the various values of total angular momentum, represented by the letter **J** . This energy split is usually of the order of ~ 10^3 cm^{-1}.

The various energy levels of the $4f$ subshell can be designated using the Russell-Saunders notation $^{(2S+1)}L_J$. The value of **L** is, under this system, written using the letters from the notation for azimuthal quantum number $\boldsymbol{l}$ of atomic subshell (s=0, p=1, d=2, f=3 ,g=4), but written in capital. A further split of the magnetic quantum number $\mathbf{M}_j$ degeneracy, of the order of ~ 10^2 cm^{-1}, is caused by the local crystal field. The magnitude of this split depends on the strength of the crystal field; a stronger field leads to a larger split.

2.2.3 Spectral Broadening

The amorphous structure of a glass means that ions are subject to different fields depending on their positions. This creates a temperature independent inhomogenous broadening of the transition spectra. This inhomogenous broadening causes a red-shift of the emission spectrum as well as a blue-shift of the absorption spectrum. As electrons rapidly and non-radiatively decay within a Stark manifold, the bottom level of the manifold is populated while the upper levels are left almost empty. Electrons in the upper manifold of a transition are brought closer to the energy of the lower manifold, hence causing a red-shift. The same thermal relaxation creates a blue-shift in the case of absorption.

The ratio between the absorption and stimulated emission cross-sections of a transition can be found using the McCumber relation. This relation states that:

$$\frac{\sigma_e(\lambda)}{\sigma_a(\lambda)} = \left(\frac{N_1}{N_2}\right)_T \exp\left(-\frac{h\nu}{k_B T}\right) \tag{2.2}$$

where σ_a is the absorption cross-section, σ_e is the stimulated emission cross section at wavelength λ, T is the effective temperature of the medium and $\left(\frac{N_1}{N_2}{}_T\right)$ is the thermal steady state ratio of the populations [5]. Interactions between phonons and electrons in the $4f$ subshell also cause spectral broadening, in this case temperature dependent and homogenous.

The absorption and emission spectra of doping ions are red-shifted relative to the free ion spectra by a phenomenon called nephelauxetic effect. The word nephelauxetic is derived from the Greek words $\nu\varepsilon\varphi\acute{\varepsilon}\lambda\eta$ meaning cloud and $\alpha\upsilon\xi\varepsilon\iota\nu$

meaning expansion, and is used to describe an expansion of the wavefunction of electrons in 5d subshells caused by the covalency of the surrounding lattice. This phenomenon decreases the repulsion between electrons in the 5d subshell and therefore their energy [6].

2.2.4 Energy Level Decay Rates

The rate of non-radiative decay of excited ions in suspension in a glass depends on the phonon energy of the host. In the case of a transition involving an energy amount greater than the phonon energy, the decay operates according to a multiphonon process. The rate of this decay follows an exponential relationship of the transition energy, for which the equation is [7]

$$W_{mp} = \beta[1 + n]^p e^{-\alpha \Delta E} \tag{2.3}$$

where n is the number of thermally generated phonon per lattice mode, ΔE the energy gap to the nearest lower Stark manifold, p the number of phonons($\frac{\Delta E}{\hbar \omega_{lattice}}$) necessary to bridge the gap, and α and β material dependent constants. Multiple phonon energies are possible in a given material, but the total decay rate is dominated by the maximum energy, so the maximum phonon energy can be used to estimate the multiphonon rate of decay. This multiphonon decay rate has a strong dependence on the maximum phonon energy.

A competition exists between the various phenomena leading to the decay of electron energy in an ion. The lifetime of an excited electron is dominated by the

fastest of these rates, according to this equation, assuming nonradiative decay is dominated by the multiphonon process:

$$\tau_{total}^{-1} = \tau_{mp}^{-1} + \tau_{r}^{-1} \tag{2.4}$$

where τ_r is the rate of radiative decay. A low multiphonon rate of decay is therefore wanted to obtain a high quantum efficiency.

The magnitude of the amplification that can be obtained through a given transition depends strongly on the upper level's multiphonon rate of decay in the host material. For this reason, certain transitions can lase in materials with low maximum phonon energy but not in materials with higher phonon energy. This is particularly true of long wavelength transitions, since the energy gap is lower and the upper level undergoes fast multiphonon decay. Lasing at shorter wavelengths can also be limited in ions where a Stark manifold lies closely below the upper state of that transition. For example, the $^3H_5$ level of Tm^{3+} lies approximately 4120 cm^{-1} below $^3H_4$ [8]; because of this, the lifetime of the latter state varies between 1350 μs in ZBLAN and 14.2 μs in silica [9]. While many instances of lasing have occurred for $^3H_4 \rightarrow {}^3H_5$ [10], $^3H_4 \rightarrow {}^3F_4$ [11], and $^3H_4 \rightarrow {}^3H_6$ [12] in ZBLAN, no instance of lasing involving $^3H_4$ as the upper level has been reported in silica. Amplification, however, has been observed in silica for both wavelength ranges that were investigated in this thesis: 810 nm [13] and 1480 nm[14].

2.2.5 Doping Methods

Several methods exist to dissolve the doping ions in a glass. Among them, there is the solution method, the dopant carrier chamber, and the frit method.

Solution Method

The solution method [15, 16] consists in first introducing the cladding in the gas phase on the surface of a silica tube. A 1500°C flame scans the surface of the tube, thereby depositing a glassy layer on the walls. The unsintered, and therefore porous, core is then deposited. Following this step, the tube is soaked in a rare earth chloride solution for a few hours. The glass is dried and oxidized in a stream of Cl_2/He/O_2. Finally, it is sintered and collapsed with a flame.

Dopant Carrier Chamber Method

Alternatively, a dopant carrier chamber whose walls are covered by a layer of anhydrous rare earth halide crystals can be attached to one end of a silica tube. The silica tube is cleaned using SF_6 to remove doping ions that attached accidentally to its surface. The cladding is deposited in the way described in the previous paragraph. When the core is being deposited, the dopant carrier chamber is heated to approximately 1000°C to form a rare earth halide vapour that is pushed in the silica tube by a flow of gas and mixes with the unsintered core. The rare earth are then oxidized and incorporated in the core [17].

Frit Method

The frit method [18] is similar to the dopant carrier method. The difference is that rare earth ions are introduced in the silica tube by using another silica tube of smaller radius filled with unsintered glass impregnated with a rare earth halide.

The frit is heated to 900°C to cause the evaporation of the rare earth halide, which then mixes up with the glass forming the core.

2.2.6 Properties of Some Ions

Erbium

Erbium doped fibres play a crucial role in modern optical fibre telecommunication networks. There is a transition in Er^{3+} ions, $^4I_{13/2} \rightarrow {}^4I_{15/2}$, which provides gain in the third telecommunications window. Ions in the $^4I_{13/2}$ state have a lifetime of approximately 10 ms in a silica host, making this state metastable and suitable as the upper level for gain at 1550 nm. The various transitions and the energy levels of Er^{3+} are shown in Table 2–1 and Fig. 2–1, respectively.

A high concentration of Er^{3+} ions in a glass host triggers a quenching process, whereby two ions excited at the $^4I_{13/2}$ level combine their energy into one ion to form a pair of one ion in the ground state and another at $^4I_{9/2}$. In high phonon energy glasses, such as silica, the excited electron quickly decays back into $^4I_{13/2}$. In this case, the efficiency is compromised as two photons are needed to excite one ion. In low phonon energy glasses, the effect is more drastic as ions in $^4I_{9/2}$ directly decay to the ground state through a radiative process, and do not contribute to the gain at all [19].

Table 2–1: Electronic transitions of the Er^{3+} ion

Wavelength (nm)	Transition
3500	$^4F_{9/2} \rightarrow {}^4I_{9/2}$
2700	$^4I_{11/2} \rightarrow {}^4I_{13/2}$
1700	$^4S_{3/2} \rightarrow {}^4I_{9/2}$
1550	$^4I_{13/2} \rightarrow {}^4I_{15/2}$
544	$^4S_{3/2} \rightarrow {}^4I_{15/2}$
470	$^2P_{3/2} \rightarrow {}^4I_{11/2}$
402	$^2P_{3/2} \rightarrow {}^4I_{13/2}$
317	$^2P_{3/2} \rightarrow {}^4I_{15/2}$

Silica Glass Host. Er^{3+} ions were at first pumped using 514 nm Ar ion laser, but this scheme was inefficient [20]. The most common pumping scheme used to excite $^4I_{13/2}$ is using a 980 nm pump to excite $^4I_{11/2}$ from the ground state $^4I_{15/2}$. Since the $^4I_{11/2} \rightarrow {}^4I_{13/2}$ transition corresponds to a 3660 cm^{-1} energy drop, this transition rapidly occurs through multi-phonon decay in a silica host.

Er^{3+} ions' absorption at 980 nm, however, is low. It can be improved by codoping the fibre with Yb^{3+} which has a much better absorption at this wavelength. Yb^{3+} ions absorb light trough the $^2F_{7/2} \rightarrow {}^2F_{5/2}$ transition and transfer their energy to nearby Er^{3+} ions, thereby exciting $^4I_{11/2}$. Er^{3+} ions quickly decay to $^4I_{13/2}$, blocking the way for a transfer back to Yb^{3+} [21].

Pumping at 800 nm and 1450 nm is also possible, but in the case of an 800 nm pump, excited state absorption (ESA) diverts electron to $^2H_{11/2}$, so this scheme suffers from low efficiency.

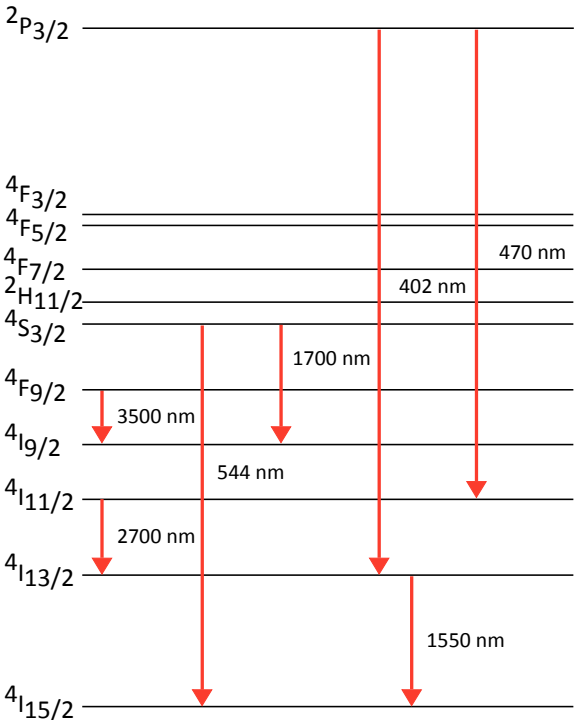

Figure 2–1: Energy levels of the Er^{3+} ion.

Fluoride Glass Host. Many lasing transitions in the mid-infrared are possible in a fluoride host, due to its lower phonon energy. A transition of particular interest is $^4I_{11/2} \rightarrow {}^4I_{13/2}$, which emits light at 2.7 μm. Emission at this wavelength is sought because it is near the peak absorption of water at 3 μm and can be used for laser surgery. One obstacle to the pursuit of lasing at 2.7 μm is the fact that the lasing transition is self-terminating; $^4I_{11/2}$ has a lifetime of 6.9 ms while for $^4I_{13/2}$ the lifetime is 9 ms.

Continuous wave (CW) lasing at 2.7 μm was first observed with an Ar ion pump at 476.5 nm [22]. The laser first excites $^4F_{3/2}$ and $^4F_{7/2}$, and excited electrons decay down to $^4I_{11/2}$. The pump depletes $^4I_{13/2}$ by ESA. The efficiency and maximum power of 2.7 μm fibre lasers can be improved by Er^{3+}/Pr^{3+} codoping. With this scheme, a maximum power and slope efficiency equal to 30 mW and 13% respectively have been achieved [23].

Pumping at 791 nm populates $^4I_{11/2}$ through $^4I_{9/2}$. This pump wavelength also causes two ESA transitions, $^4I_{13/2} \rightarrow {}^4S_3/2$ with a cross section equal to 1×10^{-21} cm^2 and $^4I_{11/2} \rightarrow {}^4F_{3/2}$ with 2×10^{-22} cm^2, compared to 5×10^{-22} cm^2 for the ground state absoprtion (GSA) [24]. Both ESA transitions contribute to the population of $^4S_{3/2}$ since ions in the $^4F_{3/2}$ state rapidly decay into the $^4S_{3/2}$ state. Colasing at 2.7 μm and 850 nm, through the $^4S_{3/2} \rightarrow {}^4I_{13/2}$ transition, saturates the output power of the 2.7 μm signal by increasing the population of the lower level state. This phenomenon can be avoided by colasing at 1.7 μm, which diverts electrons from $^4S_{3/2}$ to the $^4I_{9/2}$ energy level. 150 mW of output power has been observed using this method [25].

Lasing at both 1.66 μm and 1.72 μm through the transitions $^2H_{11/2} \rightarrow {}^4I_{9/2}$ and $^4S_{3/2} \rightarrow {}^4I_{9/2}$, pumped at 514 nm, has been achieved [26].

Lasing at 3.5 μm can be obtained in ZBLAN through the transition $^4F_{9/2} \rightarrow {}^4I_{9/2}$. This wavelength is of particular interest since the absorption bands of many hydrocarbons and hydrochlorides are situated between 3.2 μm and 3.6 μm, and the minimum atmospheric absorption for free-space communications is situated between 3 μm and 4 μm. A room temperature 2.5 mW fibre laser, with a pump threshold of 1 W and a slope efficiency of 2.8% has been achieved [27]. Since the

laser is pumped at 655 nm, and there are no powerful sources available at that wavelength, the output power at this wavelength is very limited.

Emission at 1.55 μm in Er^{3+} doped ZBLAN is not the subject of much investigation since lasing at this transition can be achieved more efficiently in a silica host. A tunable laser, ranging between 1490 nm and 1620 nm has been achieved in ZBLAN [28].

Three visible transitions, $^4S_{3/2} \rightarrow {}^4I_{15/2}$ (λ = 544 nm), $^2P_{3/2} \rightarrow {}^4I_{11/2}$ (λ = 470 nm), $^2P_{3/2} \rightarrow {}^4I_{13/2}$ (λ = 402 nm) and one ultraviolet one $^2P_{3/2} \rightarrow {}^4I_{15/2}$ (λ = 317 nm) are possible with Er^{3+} ions.

$^4S_{3/2}$ can be excited by a two-photon process with an 800 nm pump. Ions are first excited to the $^4I_{9/2}$ level and rapidly decay to $^4I_{11/2}$ and $^4I_{13/2}$, from where most ions reach $^4S_{3/2}$ through ESA. A 23 mW 546 nm laser with a slope efficiency of 11% has been operated with a 801 nm pump [29]. This laser's output saturated, and the cause was attributed to competitive lasing at 850 nm through $^4S_{3/2} \rightarrow {}^4I_{13/2}$. Lasing at 850 nm was inhibited by using a 970 nm pump, which does not depopulate $^4I_{13/2}$.

Red laser sources are effective at exciting the $^2P_{3/2}$ level. Ouput powers above 10 mW have been demonstrated at both 402 nm and 470 nm wavelengths by using a 638 nm laser diode as the pump [30].

Thulium

Silica Glass Host. In a silica host, Tm^{3+} ions are used to generate light near 1.9 μm, emitted through to the transition $^3F_4 \rightarrow {}^3H_6$. $^3F_4$ can either directly be excited by a pump at 1575 nm, or by pumping at 790 nm to excite $^3H_4$. The upper level of

the lasing transition gets populated through the cross relaxation process: $^3H_4 + {}^3H_6 \rightarrow {}^3F_4 + {}^3F_4$. The rate of this cross relaxation process is favoured by high doping concentrations. Each absorbed pump photon can potentially contribute to the emission of two photons at the signal wavelength. This lasing transition therefore can be quite efficient. An output of more than 200 W, with a slope efficiency of 65%, has been achieved [31]. The lasing transitions and the energy levels of Tm^{3+} are shown in Table 2–2 and Fig. 2–2, respectively.

Fluoride Glass Host. Three lasing transitions share the upper level $^3H_4$: $^3H_4 \rightarrow {}^3H_5$ (λ = 2.3 μm), $^3H_4 \rightarrow {}^3F_4$ (λ = 1.48 μm) and $^3H_4 \rightarrow {}^3H_6$ (λ = 0.81 μm). In a silica host, the $^3H_4$ state's lifetime is very short (14.2 μs) due to the host's high phonon energy, which depletes it through a non-radiative $^3H_4 \rightarrow {}^3H_5$ transition. In a ZBLAN host, a much longer lifetime can be observed (1350 μs) [8]. This makes it possible to induce lasing through the three transitions mentioned above. Low concentrations of Tm^{3+} ions are preferred in this case, to avoid the cross relaxation process that depopulates $^3H_4$.

Table 2–2: Electronic transitions of the Tm^{3+} ion

Wavelength (nm)	Transition
2300	$^3H_4 \rightarrow {}^3H_5$
1900	$^3F_4 \rightarrow {}^3H_6$
1480	$^3H_4 \rightarrow {}^3F_4$
810	$^3H_4 \rightarrow {}^3H_6$
784	$^1G_4 \rightarrow {}^3H_5$
515	$^1D_2 \rightarrow {}^3H_5$
480	$^1G_4 \rightarrow {}^3H_6$
455	$^1D_2 \rightarrow {}^3F_4$
365	$^1D_2 \rightarrow {}^3H_6$
350	$^1I_6 \rightarrow {}^3F_4$
284	$^1I_6 \rightarrow {}^3H_6$

Lasing at 2.3 μm has practical applications in eye-safe free-space communications, coherent radars and hydrocarbon gases detection. This wavelength, when pumped at 790 nm through the $^3H_6 \rightarrow {}^3H_4$ transition, has a saturation limit caused by the longer lifetime of electrons in the $^3F_4$ state, which is almost five times as long as in $^3H_4$ [32]. This creates a bottleneck that slows down the return of electrons to the ground level. An output power of 1 mW, with a slope efficiency of 10% has been achieved [33]. $^3F_4$ can be depopulated either by colasing at 1.9 μm [34] or by using a 1064 nm pump [12], which excites the upper laser level through

a two photon process ($^3H_6 \rightarrow {}^3H_5$ and $^3F_4 \rightarrow {}^3F_{2,3}$, with fast multiphonon decays for $^3H_5 \rightarrow {}^3F_4$ and $^3F_{2,3} \rightarrow {}^3H_4$ transitions).

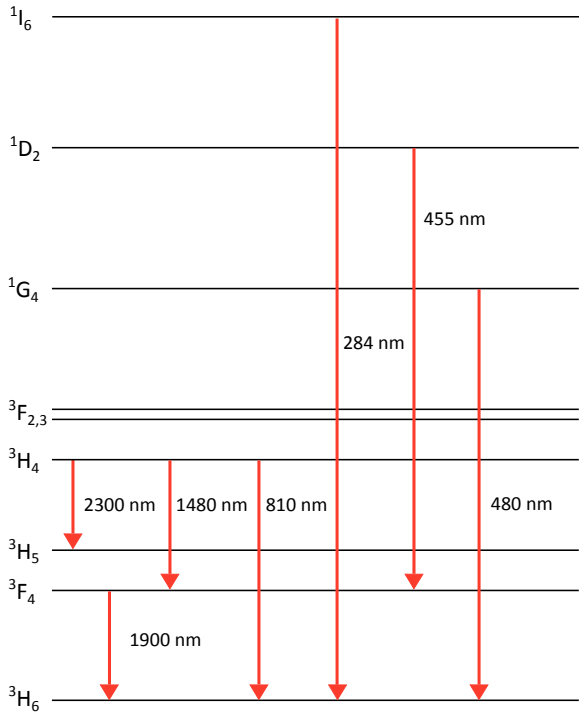

Figure 2–2: Energy levels of the Tm^{3+} ion.

Lasing at 1.48 μm deserves attention as it can serve to pump the $^4I_{11/2}$ level of Er^{3+} ions, or provide gain in S-band amplifiers. This transition suffers from the same bottleneck problem as the emission of 2.3 μm from $^3H_4 \rightarrow {}^3H_5$, and the problem can be solved with the same solutions [35, 36]. An output power of 2.3 W has been achieved with the upconversion process [11].

The $^3H_4 \rightarrow {}^3H_6$ transition can be used to emit light in the first telecommunications window. Contrarily to both previous transitions, there is no need to depopulate $^3F_4$ as electrons directly reach the ground level at the end of the lasing

transition. 1.2 W with a slope efficiency of 37% has been achieved in a ZBLAN fibre laser [10].

A large array of visible and ultraviolet transitions are also possible using Tm^{3+} ions. They are shown in Table 2–2. Two transitions can be used to emit blue light, $^1G_4 \rightarrow {}^3H_6$ (λ = 480 nm) and $^1D_2 \rightarrow {}^3F_4$ (λ = 455 nm). Lasing at 480 nm has been achieved with a 1137 nm diode pump laser through a triple excitation process [37]. Lasing in the blue range in ZBLAN is limited by a photodarkening process which creates colour centres which increase the attenuation of the fibre in the visible range.

Lasing at 455 nm has been achieved by using two pump wavelengths simultaneoulsy, i.e., at 645 nm and 1060 nm [38]. While the 645 nm emission serves to excite $^1D_2$, the 1060 nm source depopulates $^3F_4$ to avoid self-termination.

During the experimentation for this thesis, spontaneous emission of blue light has been observed from the Tm:ZBLAN fibre when pumped at 1064 nm, and also at 630 nm. This can be see in Fig 2–3. Emission in Fig. 2–3b is faint as the 630 nm pump emits only a few mW of power.

For emission at 284 nm and 350 nm, which share $^1I_6$ as the upper level, a high concentration of ion increases the rate of the $^1G_4 + {}^1G_4 \rightarrow {}^1I_6 + {}^3F_4$ cross relaxation process and improves the gain. A 42 μW emission at 284 nm was obtained from a 590 mW 1064 nm pump [39].

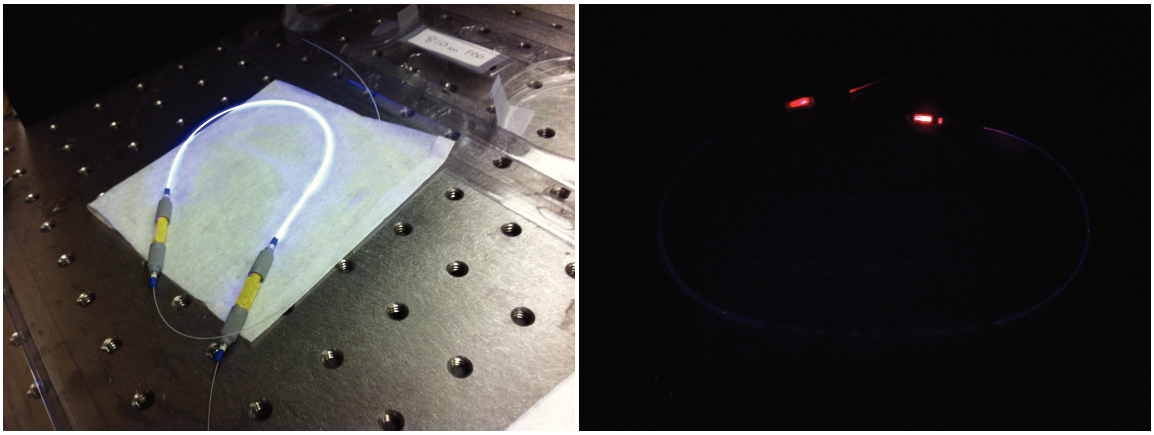

(a) Blue emission from Tm^{3+} ions excited by a 1064 nm pump.

(b) Blue emission from Tm^{3+} ions excited by a 630 nm pump.

Figure 2–3: Visible emission from Tm^{3+} ions.

Neodymium

Neodymium was the rare earth ion that was used for both the first silica fibre [40] laser and the first ZBLAN fibre laser [41]. There are three lasing transitions sharing the $^4F_{3/2}$ upper level: $^4F_{3/2} \rightarrow {}^4I_{13/2}$ ($\lambda = 1319$ nm), $^4F_{3/2} \rightarrow {}^4I_{11/2}$ ($\lambda = 1100$ nm), and $^4F_{3/2} \rightarrow {}^4I_{9/2}$ ($\lambda = 946$ nm). This upper level can either be directly pumped at 869 nm, or through $^4F_{5/2}$ and $^2H_{9/2}$ with a 800 nm pump. The transition $^4F_{3/2} \rightarrow {}^4I_{11/2}$ possesses a high cross section, making lasing through other transitions difficult due to gain competition. Furthermore, lasing at 1319 nm is difficult to achieve as ESA through $^4F_{3/2} \rightarrow {}^4G_{7/2}$ reabsorb light at the signal wavelength. Lasing at 1.315 μm has been achieved in a fluorozirconate fibre [42]. The lasing transitions and energy levels of Nd^{3+} are shown in Table 2–3 and Fig. 2–4, respectively.

Table 2–3: Electronic transitions of the Nd^{3+} ion

Wavelength (nm)	Transition
1319	$^4F_{3/2} \rightarrow {}^4I_{13/2}$
1100	$^4F_{3/2} \rightarrow {}^4I_{11/2}$
946	$^4F_{3/2} \rightarrow {}^4I_{9/2}$
412	$^2P_{3/2} \rightarrow {}^4I_{11/2}$
381	$^4D_{3/2} \rightarrow {}^4I_{11/2}$

The first silica fibre laser to be experimentally tested emitted at 1.06 μm through the transition $^4F_{3/2} \rightarrow {}^4I_{11/2}$. A 16 mW output was obtained for a 140 mW pump input at 514 nm, provided by an argon ion laser. In the case of the first fluorozirconate fibre, lasing at 1.05 μm has been observed with a threshold of 390 mW at 514 nm. Emission at in this wavelength range with Nd^{3+} attract interest since, even though it doesn't benefit from the high quantum efficiency that emission at the same wavelength in Yb^{3+} enjoys, it behaves as a four level system and therefore is excited with a lower threshold than Yb^{3+}.

A neodymium doped ZBLAN fibre laser emitting at 381 nm has been demonstrated in 1994, with a maximum output power of 74 μW for a pump input equal to 275 mW at 590 nm [43]. The next year, violet lasing (at 412 nm) has been achieved with a pump power equal to 320 mW at 590 nm, and a maximum ouput of 0.5 mW [44].

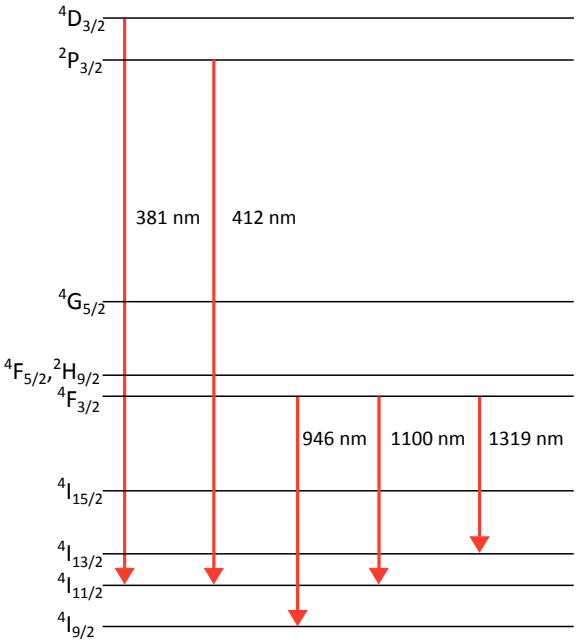

Figure 2–4: Energy levels of the Nd^{3+} ion.

Ytterbium

Yb^{3+}, since it lacks only one electron to fill its $4f$ subshell, does not have many different electronic configurations and has a simple energy diagram, shown in Fig. 2–5. The $^2F_{5/2} \rightarrow {}^2F_{7/2}$ transition provides gain near 1030 nm and can be pumped at 940 nm. Ytterbium doped lasers are characterized by a high quantum efficiency and can achieve high output powers. Yb^{3+} fibre lasers display four-level behaviour for long wavelengths. For shorter wavelengths, where there is more overlap between absorption and emission, three-level behaviour is observed.

Figure 2–5: Energy levels of the Yb^{3+} ion.

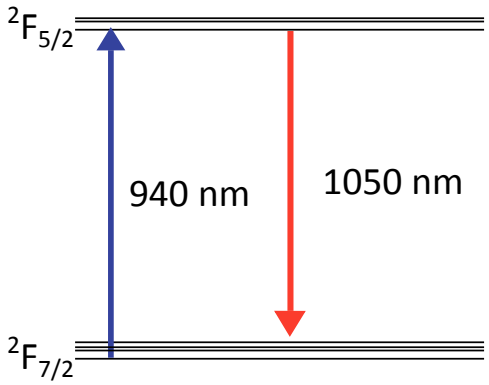

In ZBLAN, lasing at 1.02 μm has been achieved [45]. The emission of ytterbium doped ZBLAN is much stronger at this wavelength than it is in a silica host. A shift of one of the sublevels of $^2F_{5/2}$ in silica is believed to be the cause of the low gain at 1.02 μm in a silica host. An emission of 80 mW for a pump input of 200 mW has been achieved.

2.3 Conclusion

In this chapter, the basic properties of glass hosts and their influence on ion dopant particles have been presented. The necessity of low phonon energy host to sustain certain particular lasing transition, for example with Tm^{3+} ions, has been established. Some of the phenomena affecting the optical properties of ion dopants have been explained. A variety of lasing transitions and the associated pumping schemes for four different lanthanide ions, namely Er^{3+}, Tm^{3+}, Nd^{3+} and Yb^{3+} have been listed. The importance of the glass host can be understood from the information delivered in this chapter.

CHAPTER 3
Fibre Fabrication

This chapter will present the principles behind fibre Bragg gratings (FBGs), which play an important role in fibre optics. Methods of fabrication, both in silica and ZBLAN glasses will then be introduced. Some fibre materials that are used in fibre fabrication, and their relevant properties, will be shown in the next part. The chapter will conclude with a description of the fabrication methods for silica and ZBLAN fibres.

3.1 Fibre Bragg Gratings

3.1.1 Introduction

FBGs play two crucial roles in fibre laser setups; the roles of the reflector and the wavelength filter. FBGs rely on Bragg reflection to reinject a narrow linewidth of light at a specific wavelength back into the cavity. In a simple Bragg reflector, a series of reflection points are situated at equal intervals. When a wave is incident on the reflector, part of it gets reflected at each point. If the wavelength in the transmission medium is equal to twice the grating period, constructive interference leads to a strong reflection of the wave; if the wavelength is not equal to twice the period, destructive interference of the reflection causes the wave to be transmitted by the grating. It is this phenomenon that allows selective reflection of a target wavelength.

3.1.2 Silica based FBGs

Hill Gratings

The first fibre Bragg grating was fabricated in 1978 [46]. Contra-directionally propagating 488 nm Ar-ion laser beams were launched into a Ge doped silica fibre. The ensuing standing wave created a change in the refractive index at the amplitude peaks. The periodic nature of these index changes formed a Bragg grating inside the fibre. As the Bragg grating gradually formed inside the fibre during the experiment, the reflectivity at 488 nm increased. The index change in that case was later proved to be a two photon process since the grating strength increases as a quadratic function of the beam intensity [47]. Fibre gratings that are inscribed with a beam propagating through the core are known as *Hill gratings* [48].

The change in index is due to an absorption by germanium oxygen deficient centres, for which the absorption bands peak at 244 nm and 320 nm [49]. Inscribing FBGs by propagating light at 244 or 320 nm rather than at 488 nm can substantially increase the absorption of the inscribing light by relying on a simpler single photon process. The change in refractive index caused by this photosensitivity phenomenon, when appropriately annealed at temperatures 50°C above maximum operating temperature, can last for periods of 25 years [50].

Hydrogen Loading

The photosensitivity of a fibre can be significantly improved by exposing it to high-pressure, low-temperature (below 100°C) hydrogen before imprinting the grating with ultraviolet (UV). This technique, called hydrogen loading, can

permit the imprinting of gratings in fibres without any germanium doping. The concentration of hydroxyls (OH^-) in the fibre, and the associated loss, is seen to rise significantly after ultraviolet exposure in hydrogen loaded fibres.

Transverse Holographic Method

The drawback of using a beam propagating through the fibre to cause the index change is that the grating period must be equal to half of the wavelength being propagated. Since the wavelength in use must be resonant with the oxygen deficient centre and cannot be tuned very much, this leaves a very narrow band to tune the period of the gratings. This problem has been circumvented by the transverse holographic method, demonstrated by Meltz *et al.* in 1989 [51].

In the transverse holographic method, the interference pattern that determines the grating period is created by two UV beams transversally incident on the fibre. The period is in this case a function of both the angle of incidence and the wavelength of the two beams. This allows one to fix the wavelength at the absorption band and to tune the period by changing the angle. Using this technique, fibre gratings could be fabricated with reflection bands that extended into the near-infrared, thus allowing applications in the telecommunication domain.

Phase Mask Method

Another method for creating in-fibre Bragg gratings is called the phase mask technique. In this technique, the interference pattern is created by a phase mask that is held very close to the fibre, rather than by the interference of two beams.

The advantage of this technique over transverse holographic writing is that the precise alignment between two sources of light is not necessary for accurate

writing. Furthermore, it allows the fabrication of several gratings by depositing them in parallel under the mask. Also, the requirements for the coherence of the ultraviolet light source are less stringent than for the transverse holographic method, which allows the use of cheaper UV laser sources, such as excimer lasers.

However, a new mask must be manufactured for every different period that is to be written in fibre. There is some room for tuning the period using the same mask by applying tension on the fibre during the photo imprinting process. Up to 2 nm of tuning can be achieved in this way [48].

The flexibility of the phase mask technique can be used to vary the period and the amplitude of the index changes throughout the length of the grating. Two applications of that flexibility are apodization and chirping.

Apodization consists in modulating the envelope of the index change throughout the grating to control its exact reflection spectrum. Secondary maxima can be suppressed using this method [52].

Chirping consists in introducing a gradual change in the reflection wavelength throughout the length of the grating. This chirp creates a controllable dispersion of the reflected wave, and can be used to compensate for other sources of dispersion in a network [53].

FBG Types

There is a nomenclature in the literature to classify gratings according to their fabrication methods [49]. The main two categories are Type I for gratings written by exposure to UV under the damage threshold, and Type II for exposure above the damage threshold.

The index change in Type I gratings is due to photon absorption by oxygen deficiency centres. The oxygen deficiency centres are accessible by frequency doubled Ar ion sources (244 nm CW), KrF (248 nm pulsed) and ArF (193 nm pulsed) exciplex, frequency quadrupled (266 nm) and tripled (355 nm) Nd:YAG and HeCd (320 nm) lasers. The exact nature of the defect responsible for the index change has not been determined yet. The prevailing hypothesis in literature is a diamagnetic oxygen site with a lone pair of electrons [54]. Type I gratings can preserve their characteristics in temperatures up to 320°C.

In type II gratings, the exposure to UV intensities above the damage threshold leads to the formation of fractures, voids and filaments in the glass structure. Type II gratings have a higher temperature stability than their type I counterparts; they can sustain temperatures higher than 900°C. These gratings can be written using ArF exciplex lasers as the fibre is being drawn [55]. The damage to the fibre can be localised by exploiting a multiphoton absorption using femtosecond pulsed sources for writing. Most type II gratings are written point by point, rather than presenting a sinusoidal change in index, like type I gratings. This leads to strong lateral diffractive scattering.

3.1.3 Fluoride based FBGs

The fabrication of FBGs in fluoride fibres poses different challenges. The intrinsic photosensitivity of ZBLAN is very low; it is not sensitive to the 248 nm light emitted by KrF exciplex [56] laser and has a very low sensitivity to 193 nm light [57]. It can, however, be doped with photosensitive ions.

A survey [56] of the photosensitivity of Tm^{3+}, Tb^{3+}, Pr^{3+} and Ce^{3+} doped ZBLAN shows that Cerium offers the best photosensitivity. A grating written by a 248 nm laser with the transverse holographic method yielded a 0.8×10^{-5} change in refractive index. The maximum intensity of the beams was approximately 75 $mJ\cdot cm^{-2}$/pulse, with a repetition rate of 2 Hz. The index change saturated after a few minutes of exposure, when the beam was shut off, the index change dropped by 10 to 35% within a minute.

The fact that the initial index change rate is a quadratic function of the beam intensity while the saturated index is a linear function of beam intensity points to a two-photon growth process in competition with a one-photon photo bleaching process. This hypothesis is further supported by the fact that the gratings can be reversed by exposure to a single beam of uniform intensity. Moreover, the process does not seem to rely on the interaction between pairs of ion, as both the initial growth rate and the saturated index increase linearly with cerium ions concentration.

Taunay et al. have fabricated a Ce^{3+} doped ZBLAN fibre grating in 1994. 246 nm lasers used in the transverse holographic method excited a $^2F_{5/2}\rightarrow5d$ transition in the 10 000 ppm Ce^3+ ions used as doping agents in the fibre. An index change of $\Delta n = 1.7\times10^{-5}$ was achieved [58].

A Bragg gratings has been inscribed in an undoped ZBLAN fibre by using femtosecond laser at 800 nm. The index change was 3.6×10^{-4} [59].

3.1.4 Conclusion

FBGs are be fabricated by exploiting interference patterns in UV radiation. The can be made in both silica and ZBLAN fibres. In silica fibres, both Ge doping and hydrogen loading are used to increase the photosensitivity. In ZBLAN, Ce^{3+} doping and femtosecond lasers are both used.

3.2 Fibre Materials

3.2.1 Silica

The most common material used in fibre fabrication is silica. This is due to the relative ease with which silica can be purified, its good mechanical qualities, its glass stability and the availability of the material. These qualities all contribute to the economical viability of silica as a material for the fabrication of optical fibres. The disadvantages of silica are its lack of transmission in the mid-infrared, its low rare earth ions saturation concentration and its high multiphonon energies.

Refractive Index

Intrinsic silica has a refractive index equal to 1.46 at 589 nm [32]. This index can be adjusted by the addition of dopant materials. For example, TiO_2, Al_2O_3, P_2O_5 and GeO_2 increase the refractive index when used as doping agents, while on the other hand B_2O_3 and F decrease the refractive index. When choosing the dopant, it is advantageous to ensure that the core's thermal expansion coefficient be higher than the cladding's coefficient. In this way, a radial compressive stress is generated which increases the threshold for crack propagation through the fibre.

Loss

Minimal loss can be achieved in intrinsic silica at λ =1550 nm, where the loss is predicted to be 0.12 dB/km [60]. Commercial fibres can have losses as low as 0.2 dB/km [32]. Hydroxyl contamination strongly contributes to loss in silica fibres. Its overtone absorptions, including peaks at 1240, 1380 and 1900 nm can generate losses of the order of 1 dB/km-ppm in the 1310 to 1550 nm region [60].

Hydroxyl impurities can be removed through the use of pure reagents, dry gases and chlorine based compounds to dehydrate the soot before sintering. Since molecular hydrogen can react with the glass to form hydroxyl, hydrogen diffusion must be avoided, for example by using hermetic coating.

Dispersion

The zero material dispersion wavelength is centred at 1280 nm. For this reason, the second telecommunications window has been established at 1310 nm, since it is easy to shift the zero dispersion to this value. A third telecommunications window is being used in modern communication networks, at the wavelength of minimal loss, i.e., 0.2 dB/km at 1550 nm rather than 0.35 dB/km at 1310 nm, using fibres whose zero dispersion wavelength is shifted at or near 1550 nm.

Since the material dispersion of silica is anomalous for wavelengths higher than 1280 nm, while step index fibres cause normal waveguide dispersion, the latter can be used to cancel out the former at an arbitrary wavelength. The smaller the V number of a fibre is (or the higher the wavelength is), the more power is contained in the cladding, which has a lower index than the core, and therefore, the faster the wave travels along the fibre axis.

The core and NA of a fibre can be tailored to shift the zero dispersion wavelength to 1550 nm, and therefore enjoy both a low attenuation and zero dispersion. However, it was found out that in step index fibres whose zero dispersion wavelength was switched to 1550 nm, the attenuation is higher than the intrinsic value for silica [61]. This loss is believed to be due to the high concentration of Ge in the core and stress induced defects at the core/cladding interface. More complex index profiles can be used to control the waveguide dispersion without increasing significantly the fibre's attenuation. Graded index, W profile, rings, and trenches can be used to trade-off between the various metrics of the fibre.

While setting the zero dispersion wavelength exactly at 1550 nm allows for good transmission of single-channel fibre, this approach is less successful for multichannel fibres. Four-wave mixing, which causes crosstalk between the channels, is strongest when the dispersion is zero. A certain amount of dispersion helps decreasing four-wave mixing. Non zero dispersion shifted fibres (NZDSF), whose zero-dispersion wavelength is outside the EDFA gain band, were created for this purpose. Typical dispersion values for NZDSF at 1550 nm vary between 3 and 8 $ps{\cdot}nm^{-1}{\cdot}km^{-1}$.

Phonon Energy

Silica's maximum phonon energy, 1100 cm^{-1} [32], considerably limits the range of wavelengths that can be used, since its multiphonon decay rates are higher than for many other glasses. On the one hand, the attenuation increases rapidly with wavelength longer than 2 μm, limiting the usefulness of silica as a material for fibres in the mid-infrared. Also, for ions in a silica glass host, only electronic states

which possess at least 4600 cm^{-1} of difference with the nearest lower state can be metastable [62]. This prevents lasing at wavelengths higher than 2.2 μm.

3.2.2 ZBLAN

Fluoride glass, as the name indicates, is made of fluoride compounds, rather than an oxide like silica. Fluorine is the most electronegative element of the halogen group. It has a strong tendency to attract one electron and complete its valence layer, thereby forming the electronic structure of [Ne].

Fluoroberyllate

Fluoroberyllate (BeF_2) glasses have been known since 1926 [63]. BeF_2 easily forms a stable glass when cooled from the liquid phase. Its basic molecular unit, $[BeF_4]^{2-}$, is tetrahedral in shape. The tetrahedral units link to each other by the corners, in a structure very similar to the one observed in SiO_2. $[BeF_4]^{2-}$ can form complex three-dimensional crystalline structures. BeF_2 glass possess a low refractive index (n_D=1.2747), a low nonlinear refractive index ($(7.6\pm1.0)\times10^{-21}$ m^2/W), and high Abbe number (v = 106.8). The infrared cut-off is situated in the 4 to 5 μm region. The low linear and nonlinear refractive indices make BeF_2 a good candidate for the role of host glass in high power lasers, as they limit thermal lensing effects. However, BeF_2 glass' toxicity and high hygroscopicity limit its use.

Fluorozirconates

Fluorozirconate glasses offer the advantage of not being toxic. Their relative glass stability, compared to other fluoride glasses, makes them a practical material for glass lasers but still less stable than silica. For example, ZBLAN has a Hruby factor of 0.41 and a critical cooling rate of 0.7°C/min [60]. Great care must be taken

during casting and fibre drawing to avoid devitrification of the mix. The narrow set of conditions under which ZBLAN glass is formed makes fusion splicing very impractical.

The discovery that fluorozirconate based compositions can form glasses was reported by Poulain et al in 1975 [64]. A mix of ZrF_4, BaF_2 and NaF, doped by NdF_3, was unexpectedly found to be amorphous after an X-ray examination. The first report of the use of the 5 compounds that form ZBLAN, the most stable fluorozirconate glass in use nowadays, was published in 1984 [65]. The proportions of modern ZBLAN are: 53% ZrF_4, 20% BaF_2, 4% LaF_3, 3% AlF_3 and 20% NaF.

The single charge of the fluoride ion causes bonds in fluoride glasses to be weaker than in silica glass. The most obvious results of this difference are lower mechanical strength and chemical stability. Fluoride glasses are significantly more fragile than silica fibres; ZBLAN's fracture toughness is less than half of silica's [32]. Also, they are very vulnerable to moisture. The leaching rate of ZBLAN in water is 6 orders of magnitude higher than for Pyrex [60].

Structure

Two views exist concerning the structure of amorphous ZBLAN glasses. According to one, the glass is composed of zigzag chains of ZrF_6 cross-linked by BaF ionic bands [66]. Another proposed structure is a network of Zr_2F_{13} composed by the corner sharing of ZrF_7 and ZrF_8 elementary units [67]. Ba^{2+} cations are randomly distributed in the glass and form strong ionic bonds, especially with non-bridging fluorides. The presence of Ba^{2+} and Na^{+} contributes to the breakdown of the ZrF_4 lattices and therefore increase the glass stability. ZrF_4 is

organized in a three dimensional network of ZrF_8^{4-} sharing their corners. As a pure compound, it does not form a glass. However, mixtures of ZrF_4 and BaF_2 have been observed to form glasses. The substitution of Na^+, which has a smaller ionic radius than Ba^{2+} (95 and 135 pm respectively), decreases the glass transition temperature [68].

Refractive Index

ZBLAN's refractive index is equal to 1.499 at 589 nm. It can be tuned by substituting fluorides in its composition. Heavy cations, such as Pb^{2+}, Hf^{4+} and Bi^{3+} will increase the index of the mix, while light ions, for example Li^+ and Al^{3+} decrease the index. HfF_4 and PbF_2 both contribute to a decrease of the glass stability.

Phonon Energy

The weaker bonds, added to the heavier reduced mass of cations, mean that fluoride glasses possess lower phonon energies than silica (the maximum phonon energy is 600 cm^{-1} for ZBLAN compared to 1100 cm^{-1} for silica). This has an influence on optical properties. For one thing, it means that the infrared edge of the transmission window extends further towards longer wavelengths. While the transmission of silica essentially stops at 4 μm (10 dB/mm), ZBLAN's transmission window extends as high as 8 μm [32].

The lower phonon energy also affects the life time of excited states of dopant ions, especially those which possess a small energy gap between them and the next lower state. This allows some lasing transitions that are impossible in a silica host.

Loss

The theoretical minimum loss for intrinsic ZBLAN is much lower than for silica. The total loss of an ideal intrinsic glass can be predicted with the following equation [60]:

$$\alpha = (A/\lambda^4) + B_1 e^{(B_2/\lambda)} + C_1 e^{(-C_2/\lambda)} \tag{3.1}$$

where A, B_1, B_2, C_1 and C_2 are constants. The first term corresponds to loss induced by Rayleigh scattering, the second term is loss due to the Urbach tail and the third term represents the loss caused by multiphonon absorption. In the case of ZBLAN, the wavelength of minimum loss corresponds to the intersection of Rayleigh scattering and multiphonon losses. At this wavelength, losses due to the Urbach tail are negligible compared to the other two sources.

The parameters C_1 and C_2 have been obtained by a fit of measurements over ZBLAN-based glass and fibres of varying path length. The parameters were found to be $\ln C_1 = 23.2$ and $C_2 = 71.6$, leading to 0.007 dB/km at 2.55 μm. With parameter A measured to be 0.72 μm^4 dB/km, the loss induced by Rayleigh scattering is estimated to be 0.017 dB/km, for a total loss of 0.024 dB/km.

This theoretical loss, for ideal intrinsic ZBLAN, has not been achieved in practice. A value of 1 dB/km has been reported [69]. Extrinsic sources of loss are very difficult to control; typical loss values for commercial ZBLAN fibres reach values as high as 10 to 100 dB/km while commercial silica fibres can reach 0.2 dB/km [32].

Many contaminants are responsible for extrinsic losses. OH^- shows a strong absorption of 5000 $dB \cdot km^{-1} \cdot ppm^{-1}$ [70] at 2.87 μm, with combination bands at 2.24 μm (50 $dB \cdot km^{-1} \cdot ppm^{-1}$) and 2.42 μm (53 $dB \cdot km^{-1} \cdot ppm^{-1}$) for Zr-F and Ba-F respectively [71]. A low loss window coincides with the transmission peak of ZBLAN at 2.55 μm.

Reduced Zr species, Zr^{3+} and Zr^0, both absorb and scatter light. Their concentrations in fluorozirconate glass can be decreased by the use of an oxidizing atmosphere during melting.

The two oxidation states of Fe are +2 and +3. Fe^{2+} creates a loss equal to 15 $dB \cdot km^{-1} \cdot ppm^{-1}$ at 2.55 μm, but the concentration of this ion can be controlled by melting the glass under oxidizing conditions. Fe^{3+} contributes less than 0.1 $dB \cdot km^{-1} \cdot ppm^{-1}$ at this wavelength.

Co^{2+} and Nd^{3+} contribute strongly to the loss at 2.55 μm, 17.0 and 22.0 $dB \cdot km^{-1} \cdot ppm^{-1}$ respectively [72, 73]. HF, a byproduct of reactions between water and the fluorozirconate melt, has fundamental abosorption bands at 2.9 μm and 2.61 μm, whether it is associated or not, respectively. Dissolved HF is likely to be hydrogen bonded and to contribute to the 2.87 μm OH^- band [74].

While ZBLAN fibres can transmit light at longer wavelengths and can, in some cases, sustain longer lifetimes for excited states than silica fibre, their fragility makes them significantly harder to handle, limiting their usefulness. Moreover, the complexity of the fabrication process leads to notably higher costs.

3.2.3 Chalcogenides

Chalcogenide glasses are based on elements of the group XVI of the periodic table, namely sulfur, selenium and tellurium. The glasses are formed by reacting with other elements, such as Ge, As, Sb, Ga, La, etc. Chalcogenide glasses are known for their high linear and non-linear refractive indices and for their transmission windows extending far in the infrared. They are chemically durable both in liquid water and open atmosphere, and are mechanically robust. Chalcogenide glasses can be classified based on the relative ionicity of the bonds forming the glass matrix: the more ionic gallium-lanthanum-chalcogenide and the covalently-bonded glasses formed with p-block elements.

The maximum phonon energy for sulfide glasses is generally recognized to be 425 cm^{-1} [75]. Selenides and tellurides have lower maximum phonon energies due to the higher mass of their particles. The maximum phonon energies of selenides and tellurides are situated in the 230-300 cm^{-1} [76] range and permit transmission for wavelengths much further in the infrared than in silica glass.

Non-radiative decay rates of the electronic levels of rare earth ions in chalcogenides host are low due to the low maximum phonon energies of the lattices. This permits lasing transition at long wavelengths. However, no lasing transitions above 3 μm have been observed. This may be explained by the contribution of impurities in the chalcogenide glass, which can be substantially higher than the lattice contribution to non-radiative decay.

The Hruby parameter of gallium-lanthanum-sulfide glass is increased by the addition of La_2O_3 to the mix. Large amounts of lanthanum oxide, typically up

to 30%, are added to Ga:La:S to achieve crystal free fibres. The addition of La_2O_3 increases the vibrational absorption at 8.6 μm (1163 cm^{-1}), therefore also raising the maximum phonon energy to this value. Mixed sulfur-oxygen species are believed to be the cause of this absorption [77]. If we assume that a transition that can be bridged by 4 phonons or less will undergo fast multiphonon decay, then lasing can only be achieved for transitions with energy 4650 cm^{-1} ($\lambda \leq 2.1$ m). This can explain why no lasing has been successfully achieved above 2 μm in Ga:La:S glass fibre lasers.

In the case of p-block chalcogenide glasses, oxide compounds cause extrinsic absorption rather than contributing to the multiphonon edge. Oxides are the most electronegative anions in such glasses, so the real earth cations tend to form strong bonds with O^{2-} ions [78]. RE-O-RE bonds can contribute to relaxation processes between ions.

A 1080 nm ($^4F_{3/2} \rightarrow {}^4I_{11/2}$) laser in a 22 mm fibre made of Nd^{3+} doped Ga:La:S glass was reported in 1997. The $^2H_{9/2}$ and $^4F_{5/2}$ levels were pumped at 815 nm from the ground state $^4I_{9/2}$. Electrons then decayed through a multiphonon process to populate $^4F_{3/2}$, which has a lifetime of 75 μs in gallium-lanthanum-sulfide glass. A maximum slope efficiency of 0.7% was achieved for a threshold of 380 mW.

3.2.4 Tellurite

Tellurites glasses are materials based on the compound TeO_2. The canonical composition of tellurite, called TZN75 is TeO_2(75%)-ZnO(20%)-Na_2O(5%) [79]. Tellurites offer the advantage of a lower phonon energy than silica glass (~ 800 cm^{-1} for tellurite compared to 1100 cm^{-1} for silica) while having a better glass

and chemical stability and better mechanical properties than fluorides and chalcogenides [80]. Tellurite glasses possess a better transmission window (0.35-5 μm) than silica (0.2-3 μm). The non-linear refractive index of tellurite is larger than silica's by a factor of almost 25 ($2.5\times10^{-}19$ m^2/W compared to $10^{-}20$ m^2/W for silica). Up to 50 times more RE ions can be dissolved in tellurite glass than in silica.

However, the glass transition temperature (~ 300°C) of tellurite glasses is situated much lower than silica's (1000°C). This, combined with a low thermal conductivity and damage threshold make tellurite unsuitable for high-power lasers.

3.3 Fabrication Methods

3.3.1 Silica Fibres Fabrication

Silica fibre fabrication is made in two basic steps, the fabrication of a cylindrical preform followed by its drawing into a fibre. Three main techniques exist for the fabrication of the preform, outside vapour deposition (OVD), vapour axial deposition (VAD), and modified chemical vapour deposition (MCVD).

In the OVD technique, the core is first formed by depositing silica soot with a torch to form the core on a rotating silica mandrel, and then depositing the cladding. Subsequently, the mandrel is removed and the soot is dehydrated using a chlorine-based atmosphere. It is then sintered and collapsed at high temperature into a dense glass.

In VAD, the core and cladding can be simultaneously deposited using torches of different vertical orientations. The core forms starting from a seed rod which is later removed, and the cladding forms on the core boule. The dehydration and sintering steps are similar to OVD. The core is formed without a central hole and

therefore does not need to be collapsed, thereby avoiding ”burn off” of volatile components. This technique can produce fibres with very low loss.

In MCVD, a hollow cylindrical seed is used as the external part of the cladding. The layers of soot are then deposited one by one on the inside of this cylinder, while a torch circulates around the seed. Finally, the cylinder is collapsed with a hotter and/or slower flame. MCVD permits a high degree of control over the index profile since the layers are deposited one by one.

A fourth technique, called plasma chemical vapour deposition also exists. It is similar to MCVD, except that a low-pressure plasma is created inside the substrate tube. In this method, deposition of vitreous layers without an intermediate soot stage can be achieved. The thinner layers that get deposited in this technique allow a greater control over the index profile than is possible with MCVD.

Once the preform has been prepared, the fibre in its final form can be pulled from it. The preform is hung on a vertical feed mechanism above the draw furnace, at the top of a draw tower. A small section of the preform protrudes below the furnace and is kept at a temperature where the cladding glass' viscosity ranges between 10^3 to 10^5 Pa·s, which is 1950 to 2300°C for high silica glass.

The preform gets pulled down by the weight of the protruding section and elongates downward. The elongated part, once pulled to approximately the fibre's dimensions, is fed through the coating and curing systems and then to a drive capstan. The fibre's dimensions are controlled by the rate of descent, which itself is tuned through diameter monitoring data that are fed back. The final part of the fibre is spooled at a rate ensuring minimum tension.

3.3.2 Fluoride Glass Synthesis

The production of fluoride glasses requires very high purity of starting material to obtain low-loss fibres. The metal fluorides can be obtained by fluorinating metal oxides or hydroxides with ammonium bifluoride (ABF)($NH_4F{\cdot}HF$). The batches are typically mixed with ABF and heated slowly in a Pt or Au crucible, in an inert atmosphere such as Ar, until they reach glass melting temperature. The presence of H_2O in the atmosphere is very detrimental for the formation of fluoride glass. Three chemical reactions involving water, in three different temperature ranges, inhibit the formation of metal fluorides [81]:

$$MF_n + xH_2O \leftrightarrow MF_n \cdot xH_2O for T < 150°C$$

$$MF_n + xH_2O \leftrightarrow MF_{n-x}(OH)_x + xHF for 150°C < T < 250°C$$

$$MF_n + xH_2O \leftrightarrow MF_{n-2x}O_x + 2xHF for T > 600°C$$

Hydroxyls will also react with fluoride ions, making them unavailable for the fluorination of metals and causing the formation of metal oxides, through this reaction:

$$OH^- + F^- \leftrightarrow O^{2-} + HF$$

Molecular oxygen, contrarily to water, does not contribute to the formation of metal oxides, since the oxidation process involving oxygen is not thermodynamically favourable, except when Cl^- ions are present in the melt.

As the mix is heated, ABF breaks down into NH_3 and HF. The metal oxides and/or hydroxides are fluorinated by the HF. The reaction with metal oxides can be described as follows:

$$MO_n + (n - x/2)NH_4HF_2 \rightarrow MF_{2n} \cdot xNH_4F + nH_2O + (n - x/2)NH_3$$

Water and excess NH_4F and HF are volatilized during the heating cycle. This process tends to be reducing, and chemically reduced fluoride glass shows higher scattering. Later stages of melting expose the glass to an oxidizing atmosphere to correct this.

The use of ABF allows for a wide variety of starting materials for the synthesis of fluoride glasses. However, this technique leads to a large reduction in volume from the starting batches to the final melted glass. The need for a Pt or Au crucible exposes the glass to a risk of contamination by metal particles. Moreover, the ABF itself can be a source of contamination in the process.

If metal fluorides are available, they can be melted under a reactive atmosphere. An inert gas (Ar or N_2) is mixed with a reactive gas, such as CCl_4 [82], a CFC [83], SF_6 [84] or NF_3 [85]. By decomposing at the melting temperature, these gases produce halogens, thereby generating an oxidizing atmosphere. The

oxidizing atmosphere contributes to the removal of hydroxyls and metal oxides. The effect of CCl_4 is represented as follows:

$$O^{2-} + CCl_4 \rightarrow 2Cl^- + COCl_2$$
$$OH^- + CCl_4 \rightarrow Cl^- + COCl_2 + HCl$$

While reactions involving fluorides can be described by those equations:

$$O^{2-} + F_2 \rightarrow 2F^- + \frac{1}{2}O_2$$
$$2OH^- + F_2 \rightarrow 2F^- + H_2O + \frac{1}{2}O_2$$

The use of gases containing chlorine therefore leads to the formation of oxide components during melting in an oxygen atmosphere. In that respect, it is favourable to use gases not containing chlorine.

Since those reactive gases interact strongly with Pt and Au and produce dissolved metal, vitreous carbon is preferred for the crucible. A thin layer of carbon can be present at the glass surface after annealing; it can be removed by grinding, aqueous etching or reactive plasma etching.

3.3.3 Fluoride Fibre Fabrication

Fibre drawing from a preform is the most widespread technique used for the production of ZBLAN fibres [32]. A variety of preform fabrication methods exist; cladding-over-core [86], build-in-casting [87], and rotational casting [88].

Cladding-over-core

The cladding-over-core method has been demonstrated in 1981 by Mitachi *et al*. It consists in pouring the cladding melt over a core rod to obtain the preform. This method can attain a uniform cladding-to-core ratio, but bubbles and impurities are trapped at the cladding/core interface, leading to high losses.

Build-in-casting

The first step of the build-in-casting method is to pour the cladding melt into a mould kept near the glass transition temperature. The mould is then immediately turned upside down and the central part of the melt flows out, leaving a glassy layer on the inside wall of the mold. The core melt is then rapidly poured into the cylindrical void that was left. One serious disadvantage of this method is that the preform ends up being tapered since the radius of the cylindrical hollow part is not uniform. Also, air bubbles are trapped in the core/cladding interface and low-pressure bubbles can be formed at the centre of the core as it contracts during cooling.

A modified build-in-casting method [89] exists that decreases the taper induced in the fibre. In this method, instead of turning the mould upside down, the core melt is poured on top of the cladding melt. The central part of the cladding

melt, which is still fluid, is drained from the bottom, allowing the core melt to flow in the interstice and replace it.

An even more uniform cladding/core ratio can be obtained through the suction casting method [90]. In this method the cladding is poured into a mould with a bottom reservoir, and then the core melt is poured on top of it. It is the contraction of the cladding melt as it cools down that creates the central interstice in which the core melt can flow. The geometry of the fibre is controlled by adjusting the mould length and the reservoir volume.

Rotational Casting Method

In the rotational casting method, the central hollow cylinder is created by a centrifugal force obtained by rotating the mold after the cladding melt has been poured. Once the cladding has been formed, one can either pour the core melt in the central hole, or dip the mold with the cladding into the core melt. The centrifugal force can create a very uniform core radius along the fibre.

Another rotational casting method, called the spin-spin-casting method, is enacted by rotating the mould a second time, once the core melt has been poured inside cylindrical hollow part of the cladding.

The formation of bubbles can be avoided by casting the melt in a vacuum chamber. Outgassing from the melts removes the impurities on the cladding tube before the core melt is cast.

Pouring the core melt onto a glassy cladding creates a risk of crystallization at the interface, since the surface of the cladding can be reheated above the crystallization temperature. The other risk that is created is that the core and the cladding

mix at the interface. Mixing can be avoided by casting at lower temperature but at the expense of increasing the crystallization rate.

Finally, there is the rod-in-tube method. A high-quality fluoride rod fabricated by melting, casting and polishing is introduced inside a cladding tube obtained by the rotational method. The interface is evacuated during collapse. This method avoids bubbles in the core but suffers from interface defects.

Fibres can also be drawn directly from the melt. For example, in the double-crucible method [91], a large crucible contains the cladding melt while a crucible of smaller radius, inserted in the larger one, contains the core melt. Both crucibles have a tapered bottom. During fibre drawing, the tip of the smaller crucible coincides with the tip of the larger one, and the fibre is drawn from a hole in both crucibles.

Whether drawing fibres from a preform or from a crucible, precise control of the temperature is crucial, as the viscosity of the fibre is strongly dependent on temperature. It is preferable to draw fibres whose viscosity lies within 10^2 to 10^5 Pa·s and above the liquidus temperature to avoid crystallization. ZBLAN possesses a viscosity equal to $3 \cdot 10^{-2}$ Pa·s at its liquidus (600°C) temperature, which is much too low for fibre drawing. Drawing is generally done near 320°C, where the viscosity is approximately 10^4 Pa·s. Since this temperature is below the liquidus, fibre drawing must be done fast enough so as to avoid crystallization of the glass during the process. The preform is usually lowered at a speed of a few mm/min, and the fibre is wound around the capstan at approximately 10 m/min.

3.4 Conclusion

In this chapter, the basic principles and fabrication methods of FBGs have been described. The optical properties of silica, ZBLAN, chalcogenides and tellurite glasses have been discussed. The importance of the lower phonon energy of ZBLAN compared to silica, and the reason why it makes ZBLAN more versatile than silica with respect to the wavelengths that can be transmitted and generated in those glass, has been explained. A comparison between the fabrication methods of silica and ZBLAN has been shown. The difficulties in the fabrication of ZBLAN fibres were made evident.

CHAPTER 4
Lasing at 810 nm

4.1 Introduction

Single wavelength lasing in the 800 nm - 820 nm range through the $^3H_4 \rightarrow {}^3H_6$ transition of Tm^{3+} ions has been previously achieved in ZBLAN fibre. In [92], the 800 ppm Tm:ZBLAN fibre was resonantly pumped at 780 nm. A pump threshold value of 13 mW and a slope efficiency of 60% have been measured for a 2 m length. In [10], upconversion pumping at 1064 nm was used. The observed pump threshold was 1.5 W and the slope efficiency 37%, with a 35 cm length of Tm:ZBLAN fibre. At P_{pump} = 4.5 W, the output was 1.2 W.

Dual-wavelength lasing at 785 nm and 810 nm, corresponding to the $^1G_4 \rightarrow {}^3H_5$ and $^3H_4 \rightarrow {}^3H_6$ transitions, respectively, has also been demonstrated. With a 2 m 1000 ppm Tm:ZBLAN fibre, oscillation at 784 nm and 808 nm has been observed when pumped at 1120 nm above the 500 mW threshold [93].

In this work, dual-wavelength lasing at 805 nm and 810 nm through the $^3H_4 \rightarrow {}^3H_6$ transition in a Tm:ZBLAN fibre laser is demonstrated. Wavelength switching capability, as well as the observation of bistable operation are reported.

4.2 Applications

4.2.1 First window of telecommunications

In the beginnings of optical fibre communications, signals were carried by light at 850 nm, the central wavelength of the so-called first telecommunications

Table 4–1: Comparison between three short-reach communications methods [94].

	Plastic	Glass	Copper
Cost	Low	More-expensive	Low
Loss	High - medium	Low - medium	High
Connections	Easy	Difficult, requires tools	High
Handling	Easy	Requires training	Easy
Flexibility	Flexible	Brittle	Brittle
NA	High (0.4)	Low(0.1 - 0.2)	NA
Bandwidth	High (ll Gbps over 100 m)	Large (40 Gbps)	Limited to 100 mbps at 100 m)
Test equipment	Low cost	Expensive	High

window. This wavelength was chosen because it could be conveniently emitted by cheap GaAs diodes. However, it suffers from high loss and dispersion in silica fibres. First window fibre-optic communication systems are therefore more suited to short-reach networks.

Optical fibres compete with copper cables in short-reach communications. They offer advantages over copper cables, namely higher data rates and the lack of susceptibility to electro-magnetic interference. Besides glass optical fibres (GOF), plastic optical fibres (POF) are also used in short-reach communications. The three communication methods are compared in Table 4–1 [94].

POF are cheaper and easier to handle than GOF. Since POF are multimode fibres with a large core radius, they benefit from a large tolerance in alignment when connected to each other, making it easy for untrained persons to install a network. Their greater flexibility also facilitates installation. Poly(methyl methacrylate) (PMMA) fibres operate best when transmitting red signals, making the use of this sort of fibre eyesafe as operators are protected by the blink reflex. On the other

hand, greater loss and dispersion limits POF to distances of hundreds of metres [95].

GOF, when operating in the first window, display attenuations of approximately 2-3 dB/km and dispersion in the 100-120 ps/nm/km range, making them suitable for local area networks (LAN) and metropolitan area networks (MAN) for ranges between 3 to 10 km [13]. The glass transition temperature of silica is much greater than the typical temperature seens for POF (1300°C versus 100-125°C [96], making GOF more stable in high temperature environments.

The direct in-fibre generation and amplification of first window signals can greatly simplify the fabrication of network as fibre lasers and amplifiers can be integrated with the other fibres.

4.2.2 Terahertz Generation

Terahertz radiation, defined as radiation between 0.1 THz and 10 THz, has applications in spectroscopy and in imaging. In spectroscopy, molecules such as H_2O, C, N_2, O_2, O_3, HCl, CO, SO_2, CH_3CN, etc, have a distinctive signature in the THz region. THz spectroscopy can measure the carrier concentration and mobility of semiconductor materials.

In imaging, THz radiation can expose hidden details inside certain materials since it transmits through non-metallic and non-polarizing materials [97].

Thz radiation can be generated both by electronic and optical means. A GaAs Schottky-diode based device succesfully generated micro Watts of power at room temperature and can be tuned between 2.48 and 2.75 THz [98].

One THz generation method consists in using the beat frequency of two closely spaced laser beams to generate the THz output. THz radiation has been generated from the difference frequency of the photocurrent induced by two optical signals at 850 nm in a Ti/Au dual-dipole antenna on a GaAs substrate [99].

A dual-wavelength laser allows the simplification of photomixing based THz generation systems as both pump wavelengths are generated by the same device. Dual-wavelength radiation near 800 nm can exploit the current GaAs based technologies. For example, a 805 nm and 810 nm laser would generate a beat frequency equal to

$$F_{beat} = \nu_1 - \nu_2 = \frac{c_0}{805\ nm} - \frac{c_0}{810\ nm} = 2.3\ THz \tag{4.1}$$

4.3 Experimental Methodology

In both chapters 4 and 5, all experiments were conducted with various lengths of double clad 8000 ppm Tm:ZBLAN fibre, with a core diameter ~ 8 μm, inner cladding diameter of 15 μm,outer cladding diameter of 125 μm, and a numerical aperture (NA) = 0.13.

Since fusion splicing ZBLAN fibres with silica fibre was impossible, mechanical splicing was used instead to attach ZBLAN fibres to other elements of the various setups used in this work. The process consists in introducing both stripped and cleaved ends of the fibres in a plastic conduit where the tips are held face to face. A picture of a mechanical splice can be observed in Fig. 4–1. The Tm:ZBLAN

fibre is excited with light at 1064 nm in the picture, and the characteristic blue glow of excited Tm^{3+} ions can be seen.

The transmission value of the splice can be estimated in real time by transmitting visible light through one of the fibres during the splicing process. Leakage can be observed visually in this way. Mechanical splices are shown as "X" on diagrams in this thesis. Tm:ZBLAN fibres are shown in blue, while silica fibres are shown in black.

The Tm^{3+} ions were pumped at 1064 nm by an Yb^{3+} doped fibre, itself pumped by a 975 nm laser diode. All pump power values indicated in this chapter are measured directly at the output of the pump source. A power meter was used to measure the output power as a function of the diode input current. During experiments, pump powers are derived from the input current based on these measurements.

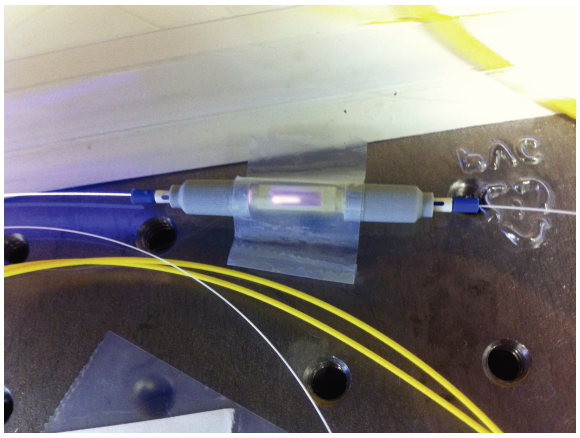

Figure 4–1: A mechanical splicing between a length of SMF-28 and a length of Tm:ZBLAN fibre.

4.4 Amplified Spontaneous Emission

The amplified spontaneous emission (ASE) from the Tm^{3+} ions has been measured using the configuration shown in Fig. 4–2. The pump was coupled into the Tm:ZBLAN fibre using a translation stage. The other end of the Tm:ZBLAN fibre was mechanically spliced to a pigtail that was connected to an optical spectrum analyzer (OSA).

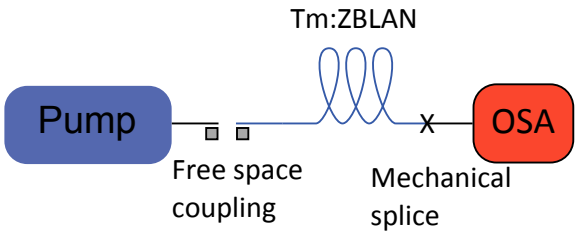

Figure 4–2: Configuration used to measure the ASE from the Tm:ZBLAN fibre

The ASE shown in Fig. 4–3 was obtained from a 22.5 cm length of fibre, pumped by 17 mW of pump at 790 nm, provided by a laser diode. ASE bumps centred at 810 nm and 1480 nm are visible, due to transitions involving $^3H_4$ as the upper level, are clearly visible on this graph. The peak near 1580 nm is a second order of the diode laser emission at 790 nm.

In Fig. 4–4, ASE was obtained by pumping 1.1 m of fibre at 1064 nm. Both peaks, at 810 nm and 1480 nm, are visible. Lasing at 813 nm can be seen for higher pump powers, despite the lack of FBG in the setup. Reflection could have been provided by the mechanical splice on one end and the cleaved facet on the other end. The leftover from the pump and the 975 nm laser diode are seen. A longer piece of fibre has been chosen for 1064 nm pumping than for 790 nm pumping,

since the absorption cross-section is lower at 1064 nm than at 790 nm (see Table 4–2).

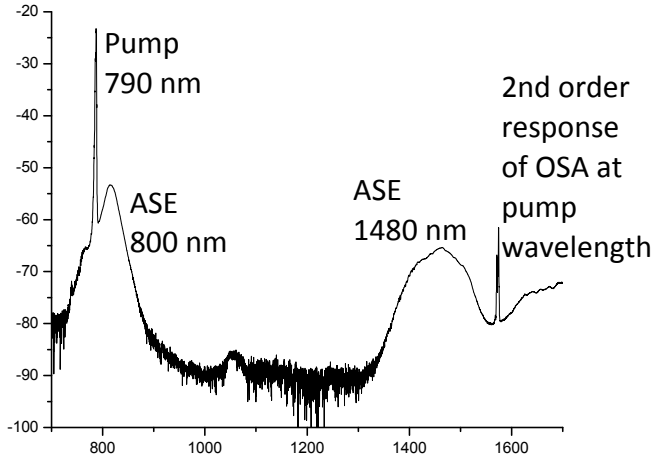

Figure 4–3: ASE obtained by pumping 22.5 cm of Tm:ZBLAN fibre with 17 mW at 790 nm.

Table 4–2: Cross sections of various absorption transition of Tm^{3+} in ZBLAN host.

Transition	Wavelength (nm)	Cross section (cm^2)
$^3H_6 \rightarrow {}^3H_5$	1064	1.06×10^{-23} [11]
$^3F_4 \rightarrow {}^3F_{2,3}$	1064	2.1045×10^{-21} [11]
$^3H_6 \rightarrow {}^3H_4$	800	1.96×10^{-21} [100]

4.5 Lasing Investigation Methodology

When lasing was induced in Tm:ZBLAN fibre near 810 nm, the output contained power both at the pump and the signal wavelength, since there was no filtering method available to separate these two wavelengths. The signal output power therefore could not be directly measured with a power meter. It was

coupled from the Tm:ZBLAN fibre to a pigtail attached to an optical spectrum analyzer (OSA). The two fibres were first placed close to each other at short distance to insure good alignment, then they were moved away up to a fixed distance of 5 mm. The fixed distance was used on the translation stage to ensure a fixed loss; this loss could then be added to the OSA measurement to estimate the output power of the fibre laser. A long distance has been chosen since it results in a more uniform light intensity on the surface of the pigtail which transmits the signal to the OSA; this can minimize the impact of vibrations on the measured output.

An SMF-28 fibre, which possess very similar characteristics (core diamter = 8.3 μm and NA = 0.13) to the Tm:ZBLAN fibre was used to measure the coupling loss for a distance of 5 mm. A 790 nm laser diode was used for this purpose, since its V parameter will be close to the V parameter of a signal at 810 nm.

First of all, the 790 nm signal was directly coupled to the OSA through an intact SMF-28 fibre. Then, the fibre was cut and cleaved, and the translation stage was used to bring both ends to a distance of 5 mm. The measured loss was 36.0 dB.

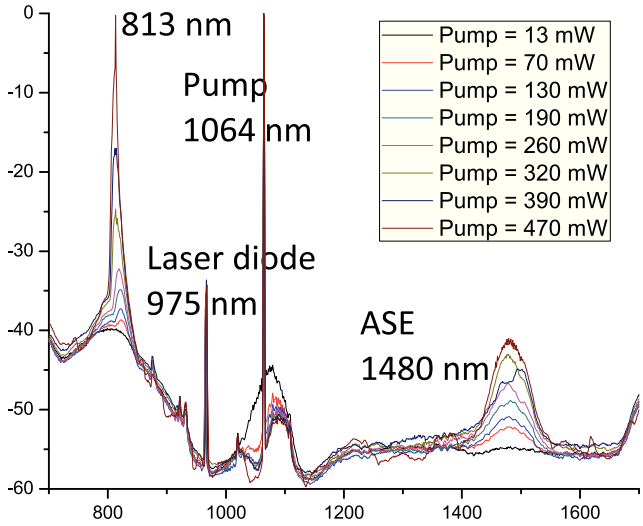

Figure 4–4: ASE obtained by pumping 1.1 m of Tm:ZBLAN fibre at 1064 nm.

4.6 Single Wavelength Lasing

4.6.1 Configuration

Single wavelength lasing, using a linear cavity shown in Fig. 4–5, was achieved at 810 nm. Feedback was provided by an FBG (reflectivity = 99.96% at 810.58 nm) on one side and the Fresnel reflection from a cleaved facet on the other side. The Tm:ZBLAN fibre was directly attached to the FBG by mechanical splicing. A translation stage was used to couple the output from the cleaved facet into an OSA.

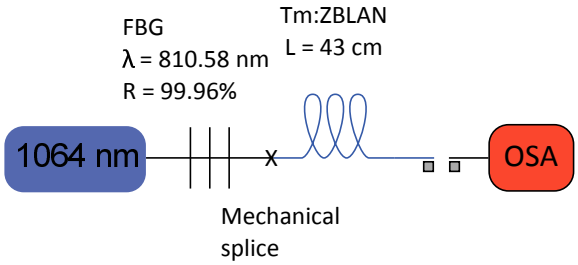

Figure 4–5: Linear cavity configuration used to achieve single wavelength lasing.

Sources of Loss

A mode field mismatch between (MFD) the fibre in which the FBG has been inscribed and the Tm:ZBLAN fibre causes loss in the cavity. The FBG has a nominal mode field diameter of 5 μm at λ = 850 nm. The Tm:ZBLAN fibre has a core diameter of 8 μm and an NA of 0.13. This indicates a V parameter equal to

$$V = \pi \frac{d}{\lambda_0} NA = \pi \times \frac{8\ \mu m}{0.85\ \mu m} \times 0.13 = 3.84$$

and therefore the fibre supports several modes at this wavelength. The mode field diameter of the gaussian mode is equal to [101]:

$$MFD = d \times \left(0.65 + \frac{1.619}{V^{3/2}} + \frac{2.879}{V^{6}}\right) = 6.9\ \mu m$$

which differs from the FBG's MFD at 850 nm.

At the target wavelength, 810 nm, the V parameter is calculated to be:

$$V = \pi \frac{d}{\lambda_0} NA = 4.03$$

4.6.2 Results

The configuration shown in Fig. 4–5, with a 43 cm length of Tm:ZBLAN fibre, started to oscillate at 810 nm when provided with 460 mW of pump power at 1064 nm. A slope efficiency of 4.9% was obtained. The output power graph is shown in Fig. 4–6. When 1 W of pump power was exceeded, a second peak appeared. The output spectra of the laser are shown for P_{pump} = 840 mW and P_{pump} = 1220 mW in Fig. 4–7. The free spectral range (FSR) of the cavity, if we estimate the cavity length to be ~ 1 m, is approximately:

$$\Delta\lambda = \frac{(\lambda_0/n)^2}{2L} \sim \frac{(810\ nm/1.5)^2}{2 \times 1\ m} = 0.15\ pm \tag{4.2}$$

The linewidth of the signal shown in Fig. 4–7a is 43 pm, which is much greater than the FSR of the cavity. The output therefore spans several longitudinal modes. The appearance of two lasing peaks shows that gain competition between these two wavelengths is not pronounced enough to inhibit lasing at both wavelengths. Gain competition may have been limited by inhomogenous broadening.

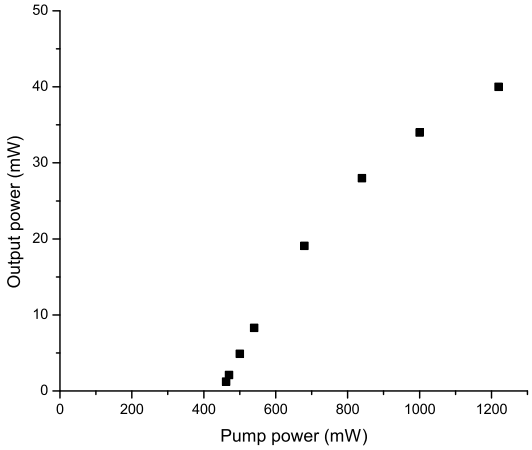

Figure 4–6: Output power obtained with 43 cm of Tm:ZBLAN with a linear cavity.

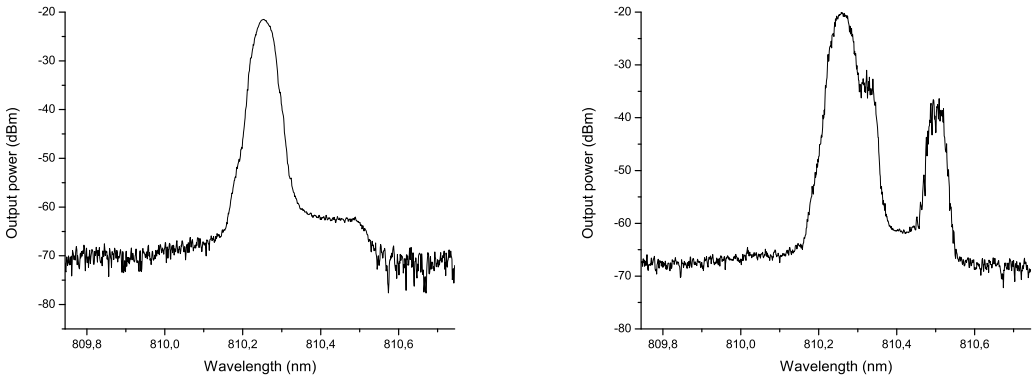

(a) Spectrum of the laser's output at P_{pump} = 840 mW.

(b) Spectrum of the laser's output at P_{pump} = 1220 mW.

Figure 4–7: Spectra obtained from the laser shown in Fig. 4–5.

4.7 Dual-wavelength lasing

4.7.1 Configurations

Two configurations have been considered for testing dual-wavelength lasing, the single cavity configuration and the cascaded cavity configuration, shown in Fig. 4–8.In both configurations, FBG_1 reflects 99.99% at 804.82 nm and FBG_2 reflects 99.96% at 810.58 nm.

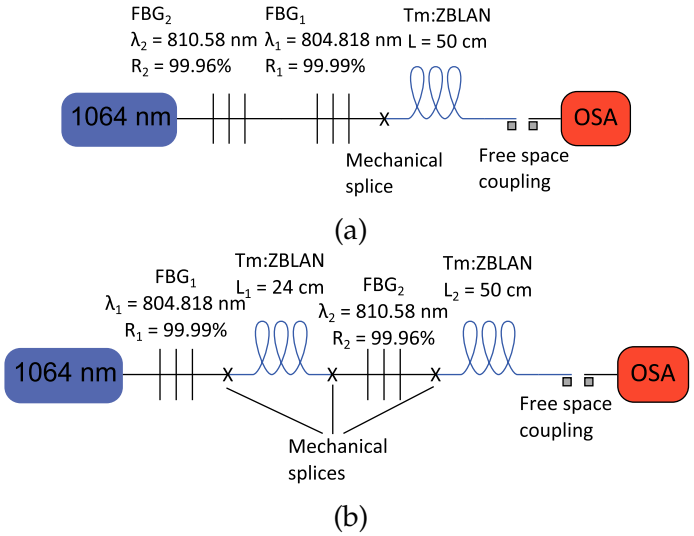

Figure 4–8: Dual-wavelength fibre laser configurations

The single cavity configuration consists in a single 50 cm length of Tm:ZBLAN fibre that provides gain for both wavelengths simultaneously. The FBGs are placed in succession on one side of the Tm:ZBLAN fibre. A higher loss is expected for the wavelength corresponding to the more external FBG. Higher gain is expected at 810 nm than at 805 nm, as can be seen from the ASE graph measured with a 1.1 m length of fibre, shown in Fig. 4–3. For this reason, FBG_2 was placed further from

the TM:ZBLAN fibre. A cleaved facet serves both as a low reflectivity mirror and an output coupler.

The cascaded cavity uses two lengths of fibre to provide gain; a 50 cm length provides gain for both wavelengths, while the 24 cm length provides gain only for λ_2. This gain counteracts the higher loss that is present in this cavity. A similar cascaded cavity design has been used in [102].

4.7.2 Results

Single Cavity Laser

In the case of the single cavity laser, the wavelength switching displayed strongly bistable behaviour, as shown in Fig. 4–9. In the region between 680 mW and 1400 mW of pump power only 810 nm oscillates when the pump power is increased, and only 805 nm oscillates when the pump power is decreased.

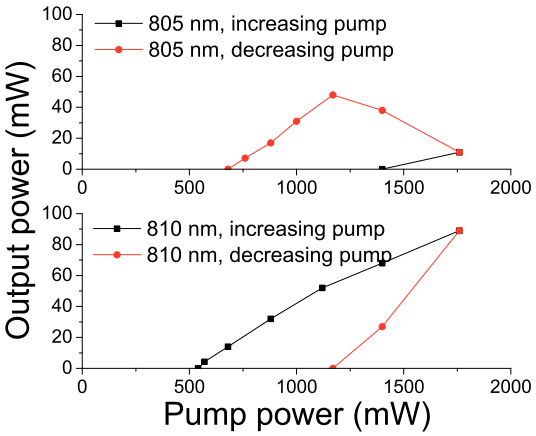

Figure 4–9: Hysteresis behaviour of the output power of the single cavity configuration shown in Fig. 4–8a.

A lasing signal at λ_2 was obtained for a threshold pump power (P_{pump}) of 540 mW; the output power at λ_2 increased with increasing P_{pump} with a slope efficiency

of 7%. When P_{pump} reached 1400 mW, lasing at λ_1 occurred. Once dual-wavelength lasing was achieved, P_{pump} was then decreased. This first caused an increase in output power at λ_1 as this wavelength took over the gain. Next, the output at λ_2 stopped once P_{pump} was decreased to 1170 mW. Finally, lasing at λ_1 stopped once P_{pump} was decreased below 680 mW. A maximum total output power of 100 mW (11.2 mW at 805 nm and 89 mW at 810 nm) was observed when P_{pump} = 1760 mW.

The spectra obtained from the single cavity laser are shown in chronological order in Fig. 4–10.

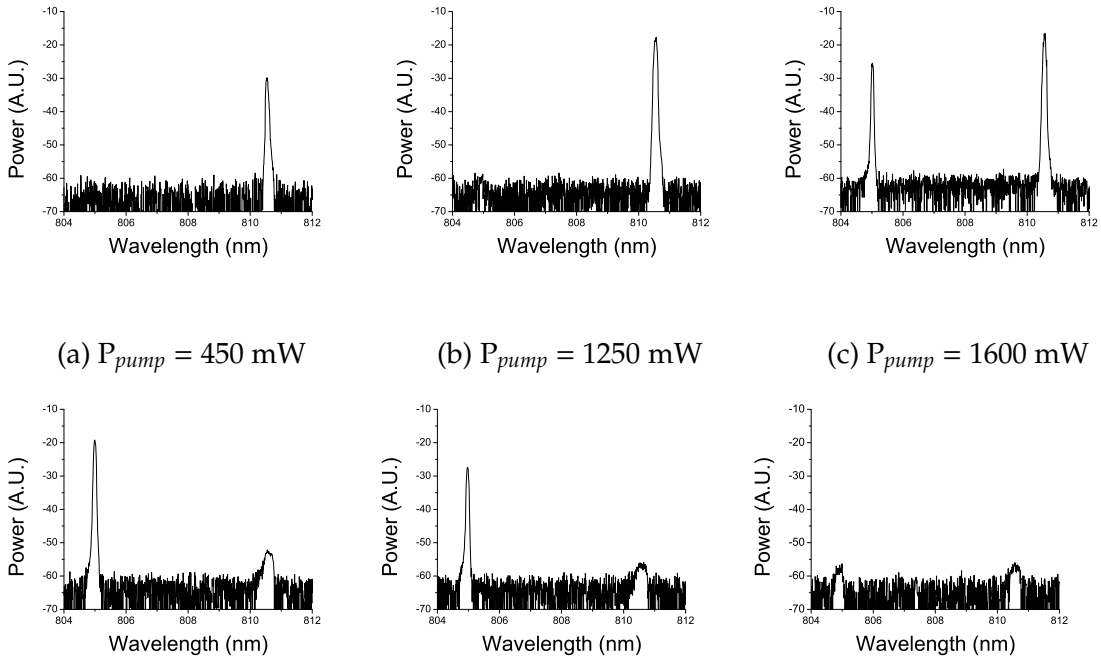

(a) P_{pump} = 450 mW (b) P_{pump} = 1250 mW (c) P_{pump} = 1600 mW

(d) P_{pump} =1020 mW (e) P_{pump} = 600 mW (f) P_{pump} = 550 mW

Figure 4–10: Evolution of the output spectrum of the single cavity as a function of P_{pump}.

Cascaded Cavity Laser

The hysteresis is much less pronounced in the case of the cascaded cavity laser, as can be seen in Fig. 4–11. One can see that contrarily to the single cavity configuration, decreasing the pump does not change the order in which the two signal wavelengths oscillate.

The turn-on and turn off thresholds for the signal at 805 nm were both 680 mW. For 810 nm, the turn on threshold was 920 mW and the turn-off threshold was 800 mW.

The output of the cacaded cavity when the pump was also consistently ramped up as shown in Fig. 4–12. Wavelength switching from 805 nm to 810 nm can clearly be observed here as the pump power is increased. The region between 920 mW and 1120 mw of pump power oscillates at both wavelengths simultaneously. The maximum power that is emitted by the cascaded cavity is 8.1 mW at P_{pump} = 1920 mW.

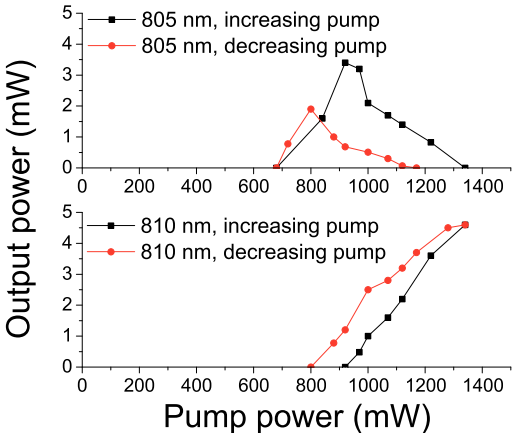

Figure 4–11: Hysteresis behaviour of the output power of the cascaded cavity configuration shown in Fig. 4–8b.

The spectra shown in Fig. 4–13 were obtained from the cascaded cavity laser while increasing P_{pump} from 0 to 1950 mW.

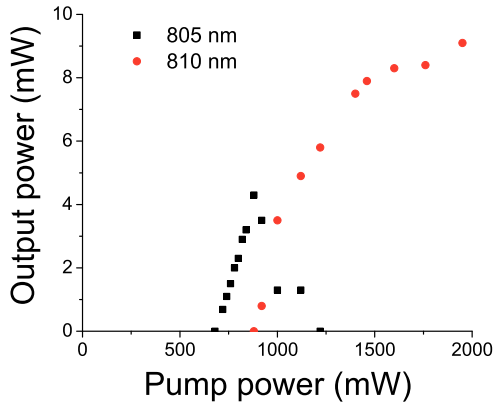

Figure 4–12: Output powers obtained for both wavelengths with the cascaded cavity configuration.

Comparison

The cascaded cavity has significantly lower output power and has a higher threshold than the single cavity design. The FBGs characteristics were not optimized for the fibre laser designs that were tested. As a result, splices between the FBG and the Tm:ZBLAN fibre cause significant losses. The single cavity design has a single point where the mode field diameter changes, between the FBG and the Tm:ZBLAN fibre. In the cascaded cavity, the wavelength that is amplified by both lengths of fibre needs to pass through two points of mode field diameter mismatches, which increases the loss. The cavity for the wavelength that is amplified by only one length of Tm:ZBLAN fibre passes through only one point of mismatch, but the Tm:ZBLAN fibre is not directly attached to the pump. Therefore, only a fraction of the pump can excite this length. These two phenomena decrease the

gain to loss ratio for a given pump input, and explain the reduced performance for the cascaded cavity.

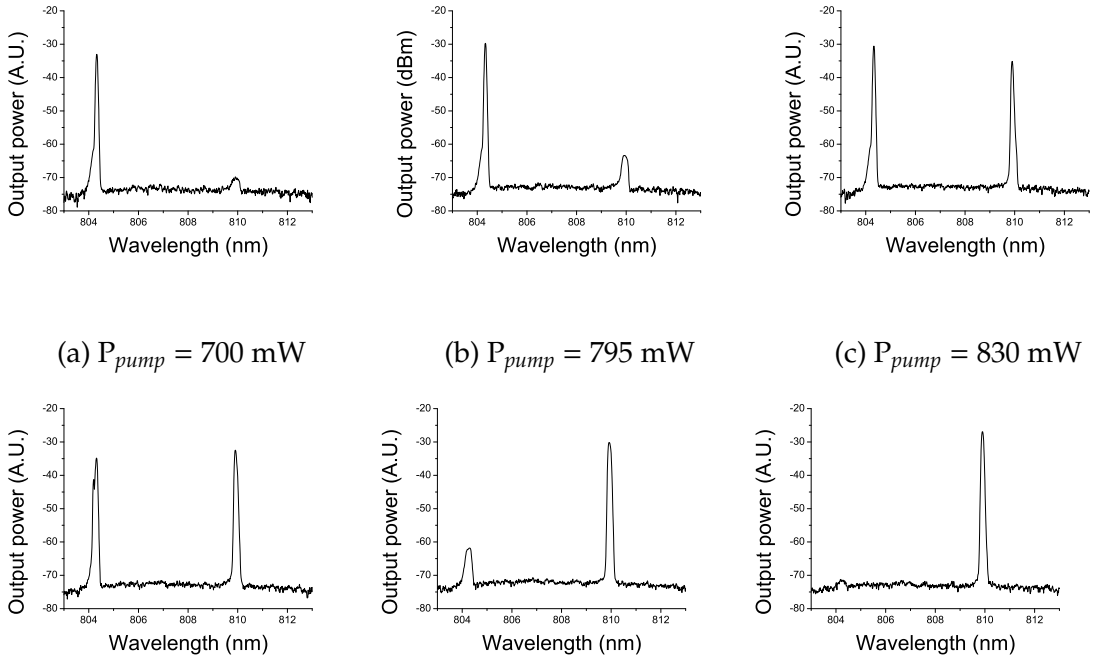

(a) P_{pump} = 700 mW (b) P_{pump} = 795 mW (c) P_{pump} = 830 mW

(d) P_{pump} = 920 mW (e) P_{pump} = 1150 mW (f) P_{pump} = 1950 mW

Figure 4–13: Evolution of the output spectrum of the cascaded cavity as a function of P_{pump}.

The wavelength switching behaviour of the cascaded cavity can be explained by observing the diagram in Fig. 4–8b. First of all, the 25 cm length of fibre is excited by the pump, which provides gain only at 805 nm. As the 25 cm length is saturated, the leftover pump excites the 50 cm length and 810 nm starts to oscillate. The signal at 810 nm ends up inhibiting lasing at 805 nm since gain is higher at 810 nm, as can be seen from the ASE graph shown in Fig. 4–3.

The results of the various laser configuration shown in this chapter are summarized in table 4–3.

Table 4–3: Output characteristics of the third telecommunication window lasers that have been tested.

Configuration	λ_1 Threshold power (mW)	λ_2 Threshold power (mW)
Fig. 4–5	-	460
Fig. 4–8a increasing P_{pump}	1400	540
Fig. 4–8a decreasing P_{pump}	680	1170
Fig. 4–8b, first run, increasing P_{pump}	680	920
Fig. 4–8b, first run, decreasing P_{pump}	680	800
Fig. 4–8b, second run, turn on threshold	720	920
Fig. 4–8b, second run, turn off threshold	1220	-

4.8 Conclusion

The output of a Tm:ZBLAN fibre in the first telecommunications window has been observed in this chapter. First of all, the ASE for two pump wavelengths, 790 nm and 1064 nm, has been shown. After this, single wavelength lasing at 810 nm with a 1064 nm pump has been achieved and the results were presented. Dual-wavelength lasing at 805 nm and 810 nm has been demonstrated with two

configurations, a single cavity configuration and a cascaded cavity configuration. Strong hysteresis was observed in the single cavity configuration, while the behaviour was more stable with respect to pump with the cascaded cavity configuration.

CHAPTER 5
Lasing at 1480 nm

5.1 Introduction

A variety of pumping schemes, with the goal of achieving gain in the S-band from a Tm:ZBLAN fibre, have been demonstrated in the literature. At λ_{pump} = 1.4 μm, 24 dB of gain was obtained in a double-pass scheme in a 3 m long fibre, with 755 mW of pump power. P_{input} was equal to 5 dBm [103].

With a mix of 150 mW at 1410 nm and 40 mW at 1560 nm in 20 m of fibre, 32 dB of gain was obtained with P_{input} = -30 dBm [104]. 110 mW at 1047 nm and 12 mW at 1560 nm yields 32 dB in a 20 m long fibre, for P_{input} = -30 dBm [105]. Pumping at 1560 nm excites $^3F_4$ directly from the ground state, 1047 nm radiation pumps electron from $^3F_4$ to $^3F_{2,3}$ while radiation at 1410 nm directly excites electrons from $^3F_4$ to the $^3H_4$ level.

A pumping scheme based on 1064 nm radiation, with some power at 1117 nm to help populate $^3F_4$ through $^3H_5$ has been demonstrated in [106]. 26 dB of gain have been obtained from a -14 dBm signal input in 12 m of doped fibre.

Using 800 nm to directly populate the gain upper level $^3H_4$, and then 1050 nm to re-excite electrons from $^3F_4$ after stimulated emission, 27 dB were obtained from a 15 m length of fibre and combined pump power of 180 mW [107]. P_{input} = -27 dBm in that case.

As for lasing at 1.48 μm, $^3F_4$ can be depleted by colasing at 1.9 μm. This method has been used in [35] with 0.5 m of Tm:ZBLAN, with a 780 nm pump that directly excited ions to the $^3H_4$ energy level. Lasing at 1.47 μm was obtained with a threshold of 3.2 mW and a slope efficiency of 43% while at 1.82 μm the threshold 8.5 mW and the slope efficiency was 38%. At P_{pump} = 325 mW, the output was 130 mW and 115 mW for 1.47 μm and 1.82 μm.

Ions at the $^3F_4$ energy level can be re-excited to $^3H_4$ with radiation at 1064 nm (see Fig. 5–1 [108]). However, the $^3H_6 \rightarrow {}^3H_5$ transition is centered at 1210 nm, and GSA is limited at 1064 nm, as can be seen in Fig. 5–2 [109]. The overlap between these two absorption spectra allow the excitation of $^3H_4$ with a single wavelength through a two-photon process. In [11], 2.25 W of power at 1480 nm have been obtained from a 2.8 m length of 2000 ppm Tm:ZBLAN fibre by pumping it at 1064 nm with 6.5 W.

No instance of dual-wavelength lasing as been found in the literature.

In this chapter, the gain characterization of various lengths of 1064 nm pumped Tm:ZBLAN fibre is shown. Single wavelength lasing at 1476 nm and 1487 nm and dual-wavelength lasing at 1476 nm and 1487 nm, and at 1487 nm and 1487.6 nm is achieved and the characteristics of the various laser configurations are presented.

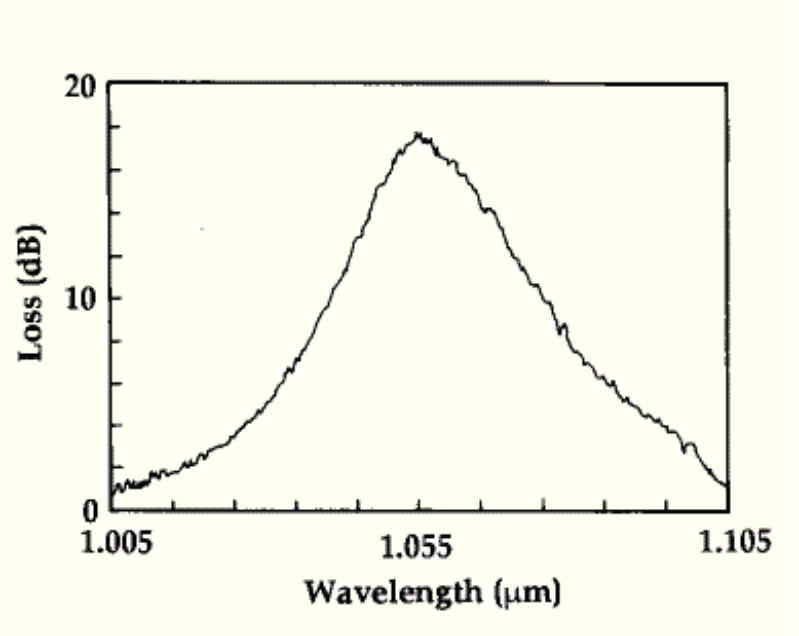

Figure 5–1: Spectrum of the $^3F_4 \rightarrow {}^3F_2$ ESA in Tm:ZBLAN.

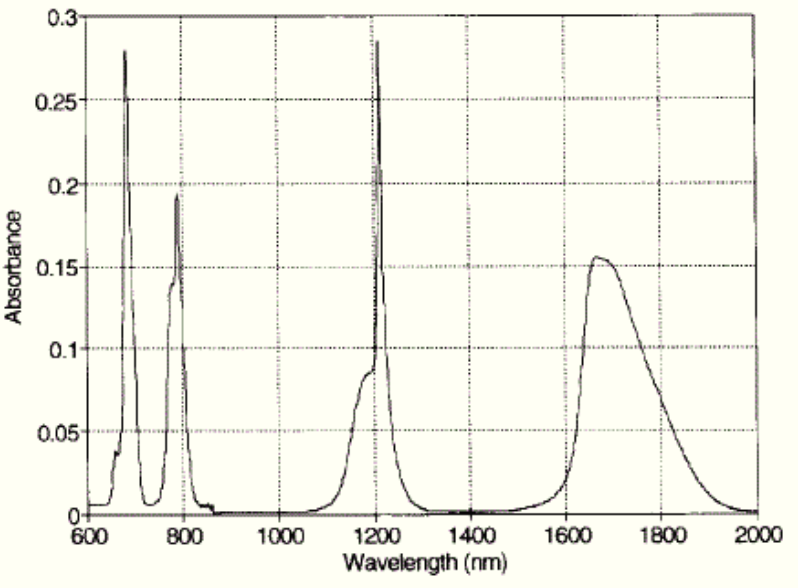

Figure 5–2: GSA spectrum of Tm:ZBLAN.

5.2 Applications

5.2.1 Extension of the Third Window into the S-band

EDFAs are a very widely used means to provide gain in the C and L bands of the third telecommunications window. However, increasing demands for large bandwidths stimulate research aimed at widening the band of carrier wavelengths in fibre optic communication systems. The S-band allows such an extension of the communication window, while being higher than the OH^- absorption band at 1360-1420 nm [110], but is unfortunately outside the amplification range of Er^{3+} ions.

Tm^{3+} ions provide gain that can easily be exploited to amplify signals in the S-band and therefore improve the bandwidth of wavelength division multiplexing systems [111]. Amplification is more effective in low phonon energy glass hosts, as the upper level of the gain transition, $^3H_4$, rapidly decays to $^3H_5$ in high phonon energy hosts. Nonetheless, amplification has been achieved in Tm^{3+} silica fibres. 11.3 dB at 1470 nm has been obtained with 2 W of pump at 1064 nm in [112].

5.2.2 Pumping EDFAs

Two main pumping schemes exist for EDFAs providing gain at 1550 nm: using 980 nm to excite $^4I_{11/2}$ which rapidly decays to $^4I_{13/2}$, or using 1480 nm to directly pump $^4I_{13/2}$.

980 nm provokes no de-excitation of ions at the $^4I_{13/2}$ level, while pumping at 1480 nm causes the deexcitation of ions in this level through stimulated emission. This phenomenon causes EDFA pumped at 1480 nm to have a lower saturated power, as high levels of population inversion increase the stimulated emission

caused by the pump as much as it decreases the absorption. It also has an effect on the spectrum; this de-excitation lowers the gain at shorter wavelengths, flattening the gain with respect to signal wavelength. In Fig. 5–3, the peak in gain at 1530 nm that can be observed when pumped at 980 nm is less prominent with 1480 nm pumping [113].

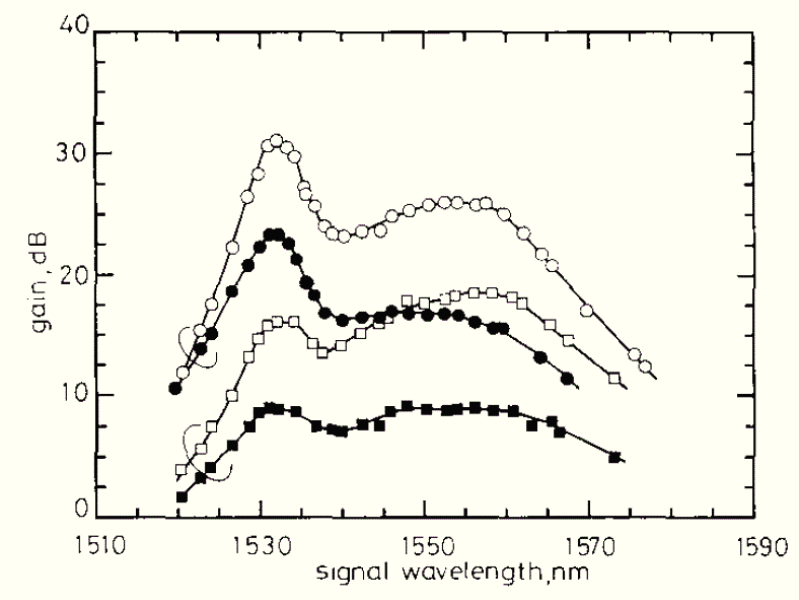

Figure 5–3: Gain spectra for EDFAs pumped at 60 mW with P_{signal} = -40 dBm [113]
○ L = 1 m, ● L = 50 cm: λ_p = 980 nm
□ L = 1 m, ■ L = 50 cm: λ_p = 1480 nm

5.2.3 Terahertz Generation

Terahertz radiation, discussed in section 4.2.2, can be generated by the photomixing of two closely spaced wavelength. An InGaAs photomixer has successfully generated 45 nW of power at 0.5 THz [114] from two wavelengths in the third telecommunications window, in this case at 1.55 μm.

Two signals, at 1476 nm and 1487 nm, can generate a beat frequency equal to:

$$F_{beat} = \nu_1 - \nu_2 = \frac{c_0}{1476\ nm} - \frac{c_0}{1487\ nm} = 1.5\ THz$$

5.3 Amplification

5.3.1 Methodology

Measurements of the gain provided by the Tm:ZBLAN fibre while excited by a 1064 nm pump have been made on 85 and 105 cm lengths. The setup used to make those measurements is shown in Fig. 5–4. The signal was generated by an external cavity laser (ECL). Since the ECL could not emit signals below -7 dBm, an optical attenuator has been introduced between the ECL and the input wavelength-division multiplexer (WDM) coupler for lower signal powers. The gain is defined as the ratio of the signal power measured at the signal port of the output WDM coupler to the signal power measured at the output of the ECL (or attenuator). Measured gain values include gain from the Tm:ZBLAN fibre and splicing losses. The noise figure values of the amplifiers have not been measured.

One set of measurements was made on 85 cm and 105 cm lengths of fibre by sweeping λ_{signal} between 1460 nm and 1520 nm and P_{pump} between 0 mW and 2090 mW. P_{input} was set to -31.8 dBm.

Another set of spectral measurements was made on the 85 cm length of fibre by fixing the pump power to 2090 mW and sweeping P_{input} between -57.8 dBm and 7.6 dBm and λ_{signal} between 1460 nm and 1520 nm.

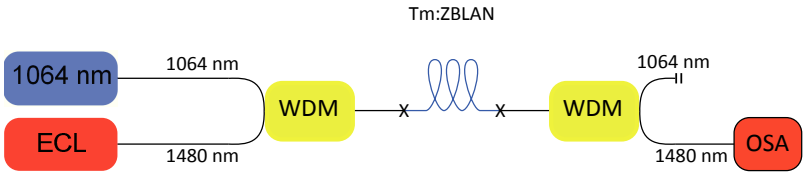

Figure 5–4: Configuration that was used to measure the gain of various lengths of Tm:ZBLAN.

The gain characteristics of the Tm^{3+} ions were investigated at 1460 nm on the 85 cm and 105 cm lengths of fibre with a set measurements made by fixing λ_{signal} to this wavelength nm and sweeping both P_{input} between -57.8 dBm and 3.6 dBm and P_{pump} between 0 and 2090 mW. 1460 nm has been chosen since it was the lowest wavelength available on the ECL, and ESA due to the $^3F_4 \rightarrow {}^3H_4$ is the most prominent at this wavelength.

5.3.2 Spectral measurements

The gain spectra are shown in Fig. 5–5 at P_{input} = -31.8 dBm.

All graphs display a gain peak around λ_{signal} = 1475 nm. An increase in the net attenuation of unexcited fibres can be seen as the wavelength increases. This is consistent with the absorption spectrum of of the $^3H_6 \rightarrow {}^3F_4$ transition. The absorption/emission spectrum of Tm:ZBLAN is shown in Fig. 5–6 [115].

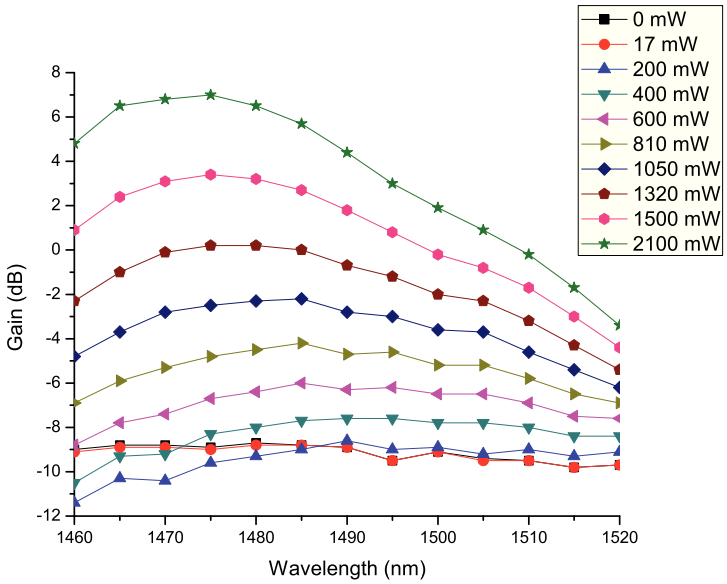

(a) Gain spectrum for a 85 cm length of Tm:ZBLAN.

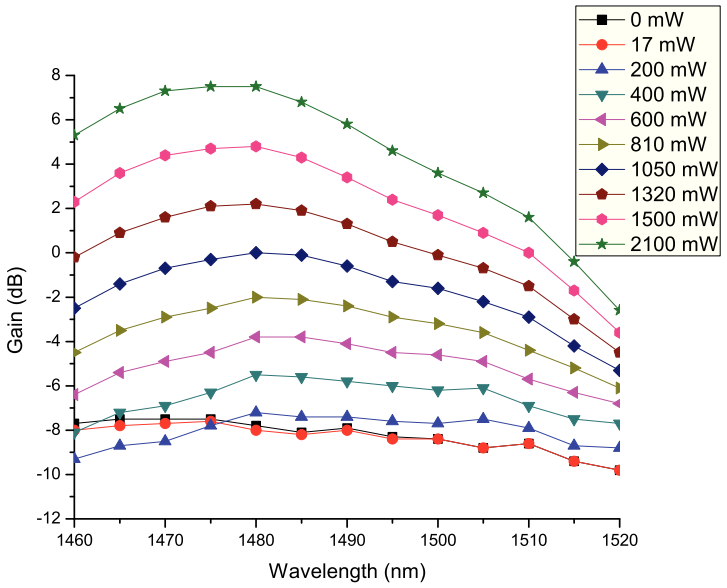

(b) Gain spectrum for a 105 cm length of Tm:ZBLAN.

Figure 5–5: Gain spectra for various lengths of Tm:ZBLAN at P_{input} = -31.8 dBm.

When P_{input} = -31.8 dBm, a noticeable drop in net gain can be observed at 1460 nm when P_{pump} reaches 200 mW. This drop in gain, followed by an increase for higher P_{pump} is consistent with the two photon process that provides amplification in the S-band. It would correspond to ESA by ions excited at the $^3F_4$ level. This drop is greater at wavelengths shorter than the amplification peak, just like the absorption and emission peaks of a single transition as was explained in section 2.2.3.

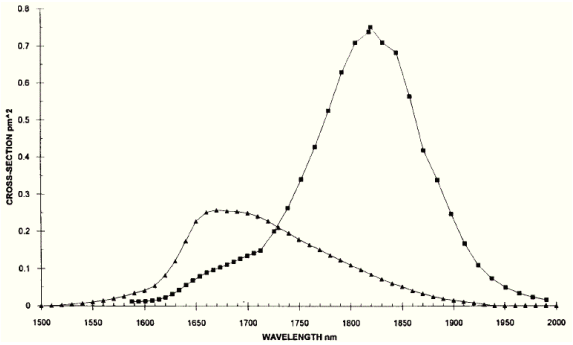

Figure 5–6: Absorption and emission spectra of Tm:ZBLAN.
▲ : Absorption spectrum
■ : Emission spectrum

$^3F_4$ has a very low occupancy at thermal equilibrium at T = 300 K, since its energy gap with the ground state E_g = 0.671 eV [8], which is significantly larger than the thermal energy kT = 0.026 eV, while $^3H_4$ has an even lower occupancy since it lies 1.53 eV above ground state. Transitions between these two energy levels have therefore very little influence on a signal when ions are unexcited.

Low values of P_{pump} populate $^3F_4$ more than they populate $^3H_4$, causing a net decrease in gain. Higher values of P_{pump} cause a net gain through population inversion, as the stimulated emission from $^3H_4 \rightarrow {}^3F_4$ exceeds absorption from $^3F_4 \rightarrow {}^3H_4$.

The spectra for P_{pump} = 2090 mW are shown at various values of P_{input} in Fig. 5–7, for the 85 cm length of fibre. The gain as a function of P_{input} is shown in Fig. 5–8. One can see an increase in gain, relative to the stable small signal value, for $P_{input} < -40$ dBm. Gain compression is observed for P_{input} values with the highest gain. The lowest P_{sat} to be observed is 3.6 dBm at λ_{signal} = 1465 nm. At λ_{signal} = 1475 nm, where the gain is highest, P_{sat} = 4.6 dBm.

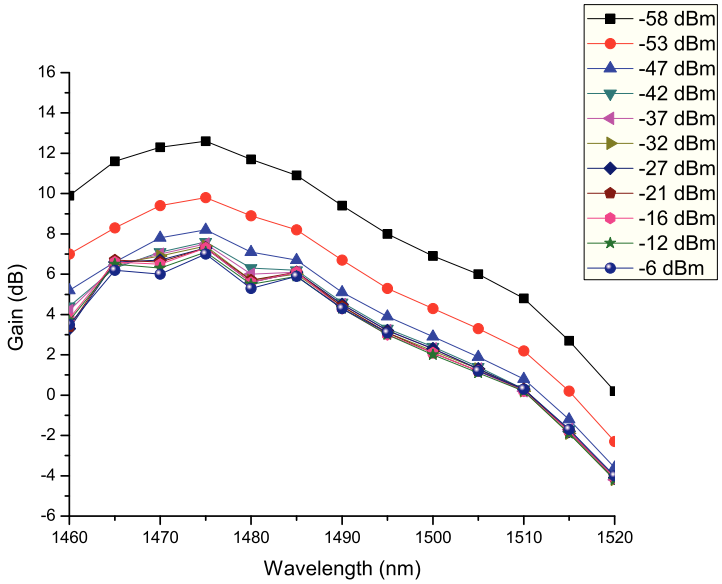

(a) Spectrum at various P_{input} values controlled with an OA and P_{pump} fixed at 2090 mW for an 85 cm length of Tm:ZBLAN fibre.

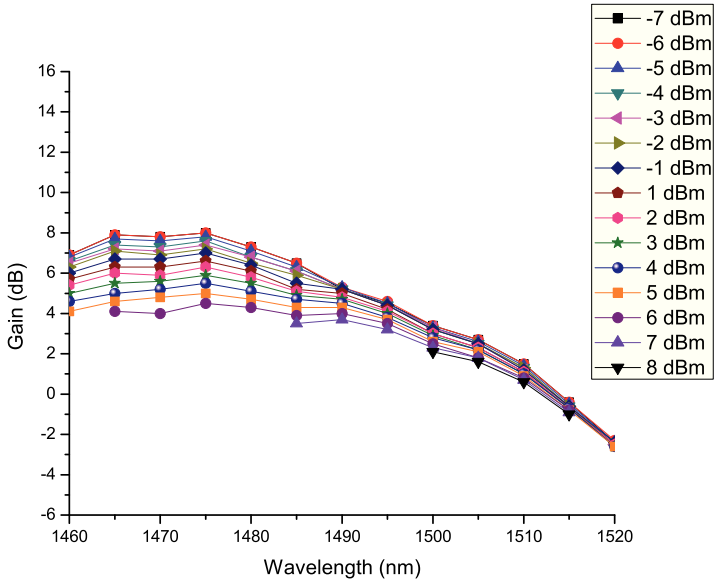

(b) Spectrum at various P_{input} values controlled without an OA and P_{pump} fixed at 2090 mW for an 85 cm length of Tm:ZBLAN fibre.

Figure 5–7: Spectrum for the 85 cm length of Tm:ZBLAN fibre with P_{pump} fixed at 2090 mW

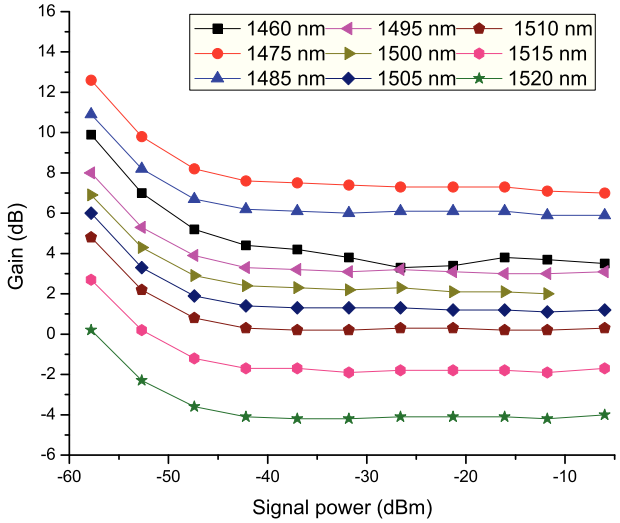

(a) Gain for low values of P_{input} with a 85 cm length of fibre.

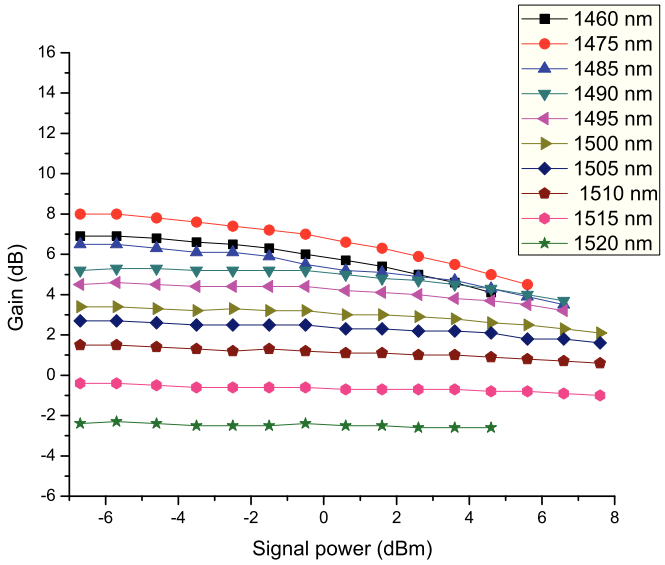

(b) Gain for high values of P_{input} with a 85 cm length of fibre.

Figure 5–8: Gain for the 85 cm length of Tm:ZBLAN fibre pumped at 2090 mW, as a function of P_{input}.

5.3.3 Gain characteristics at 1460 nm

The gain at λ_{signal} = 1460 nm can be seen as a function of P_{pump} in Fig. 5–9, and as a function of P_{input} in Fig. 5–10. A decrease in net gain can be seen for $P_{pump} < 600$ mW for $P_{input} \geq -47dBm$.

At P_{input} = -57.8 dBm, one can notice that the gain is higher than the stable small signal gain and that contrarily to the gain for higher values of P_{input}, no net increase in absorption is visible for low P_{pump}.

The increase in gain is only visible for pump powers above 200 mW, and is therefore triggered by the pump. As can be seen in Fig. 5–11, where the difference between the gain at P_{input} = -57.8 dBm and P_{input} = - 42.2 dBm is plotted as a function of λ_{signal}, this gain increase is much less wavelength dependant than the gain itself.

5.3.4 Conclusion

The characteristics of ion excitation can be observed since it is consistent in both lengths. The data for all lengths fit with a $^3F_4 \rightarrow {}^3H_4$ ESA at shorter wavelengths, triggered by $^3H_6 \rightarrow {}^3H_5$ absorption followed by quick non-radiative decay to $^3F_4$ at low P_{pump} values.

Higher pump values populate $^3H_4$ and cause gain at a longer wavelength values, centred near 1475 nm, through the $^3H_4 \rightarrow {}^3H_6$ transition.

The short-wavelengths edge of absorption from the $^3H_6 \rightarrow {}^3F_4$ transition, centred at 1650 nm (see Fig. 5–6), is seen at longer wavelengths. The $^3H_6 \rightarrow {}^3F_4$ transition is a GSA, therefore it attenuates the signal at P_{pump} = 0 mW.

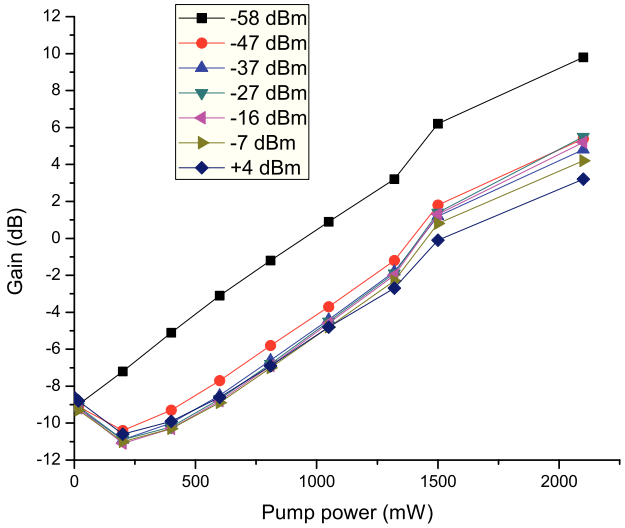

(a) Gain at λ_{signal} = 1460 nm as a function of P_{pump} for an 85 cm length of Tm:ZBLAN fibre.

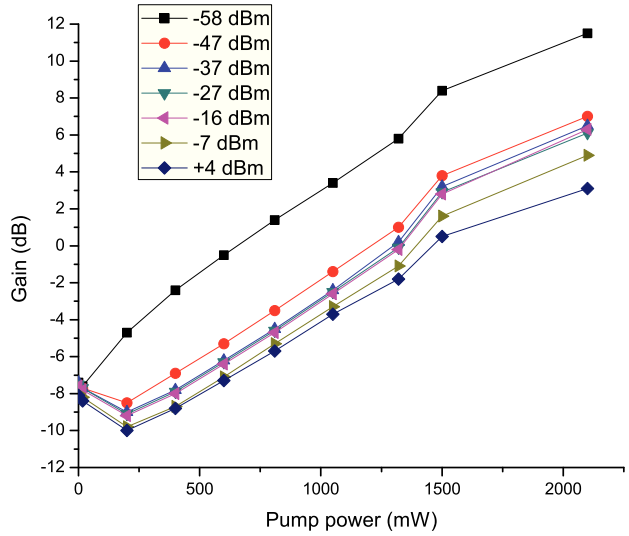

(b) Gain at λ_{signal} = 1460 nm as a function of P_{pump} for a 105 cm length of Tm:ZBLAN fibre.

Figure 5–9: Gain at λ_{signal} = 1460 nm as a function of P_{pump} for various length of Tm:ZBLAN fibre.

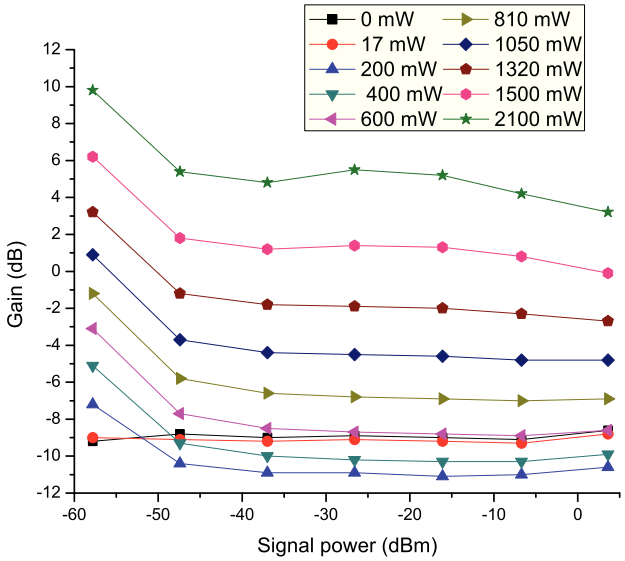

(a) Gain at λ_{signal} = 1460 nm as a function of P_{signal} for an 85 cm length of Tm:ZBLAN fibre.

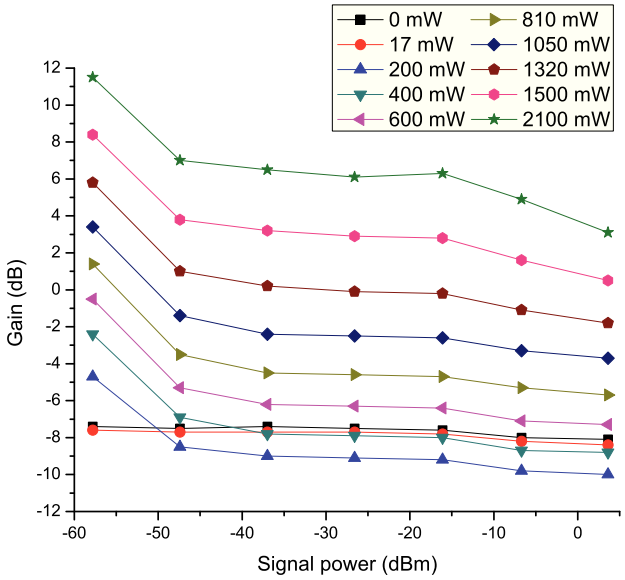

(b) Gain at λ_{signal} = 1460 nm as a function of P_{signal} for a 105 cm length of Tm:ZBLAN fibre.

Figure 5–10: Gain at λ_{signal} = 1460 nm as a function of P_{signal} for various length of Tm:ZBLAN fibre.

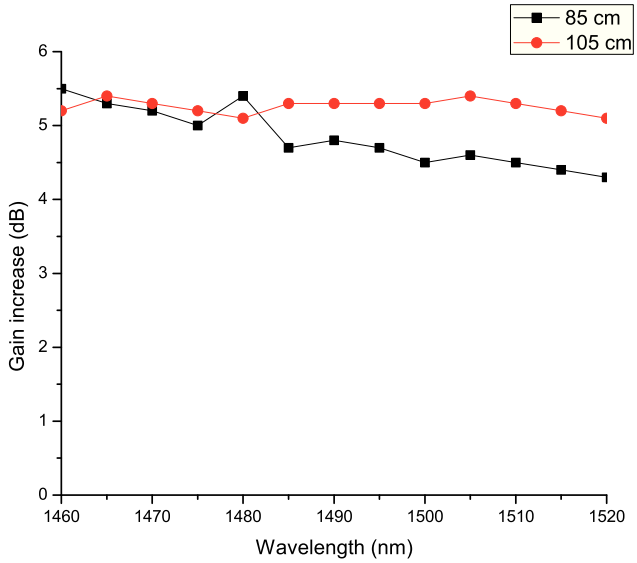

Figure 5–11: Wavelength dependance of the low-signal gain increase for 85 cm and 105 cm lengths of fibre.

5.4 Single wavelength lasing

5.4.1 Methodology

Single wavelength lasing was achieved with a variety of configurations. Ring cavity laser configurations, for both co-propagating and counter-propagating pumping, are shown in Fig. 5–12. The signal was filtered using a 1487 nm FBG. Linear cavity configurations are shown in Fig. 5–13. In Fig. 5–13a, the cavity is bound by a 1475.7 nm FBG on one side, and a combination of a 3 dB coupler and a circulator that nominally reflects 50% of the signal back into the cavity and couples the other 50% out for measurement. A cleaved facet served these two functions in the setup shown in 5–13b. The pump power values for sections 5.4 and 5.5 were

measured at the output of the WDM coupler that was used to separate λ_{pump} and λ_{signal}.

In the both ring cavity and linear cavity configurations, all connections between the various elements of the design were made with angle polished connectors (APC). In the setup shown in Fig. 5–13b, the signal output of the WDM was connected with an APC to a pigtail whose end facet was cleaved. Both sides of the Tm:ZBLAN fibres were mechanically spliced to pigtails with APCs so as to be connected with the rest of the device.

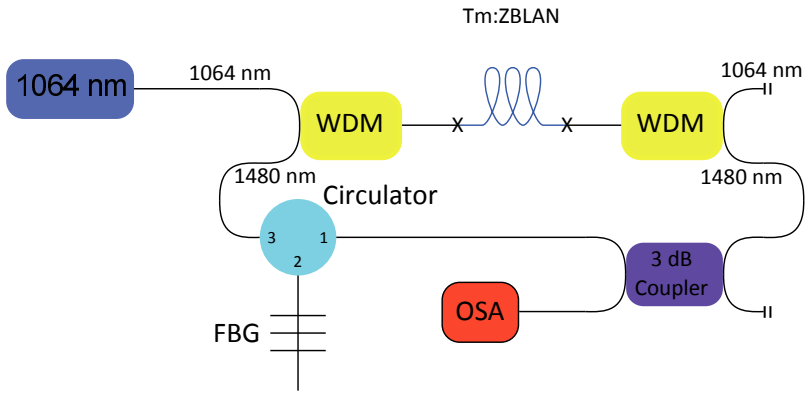

(a) Ring cavity laser configuration, with co-propagating pumping.

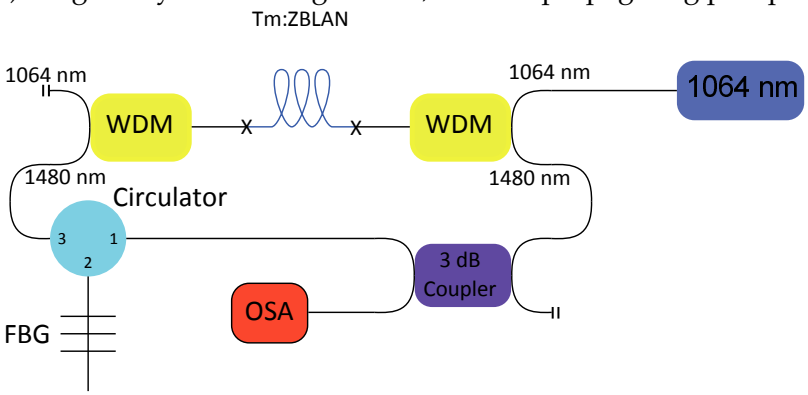

(b) Ring cavity laser configuration, with counter-propagating pumping.

Figure 5–12: Ring cavity laser configurations.

5.4.2 Ring Cavity Lasers

Lengths of 95 cm and 2 m of Tm:ZBLAN fibre were used in the ring cavity configurations. The FBG reflection wavelength was 1487 nm. When using co-propagating pumping to excite the Tm:ZBLAN fibre, a threshold of 600 mW has been observed with the 95 cm length and 690 mW with the 2 m length. The efficiencies were measured to be 5.3% and 1.47% for both lengths, respectively. For the counter-propagating configuration, the thresholds were 575 mW and 655 mW for 95 cm and 2 m, and the efficiencies 11.4% and 9% respectively. The output power graph for ring cavity laser configurations is shown in Fig. 5–14.

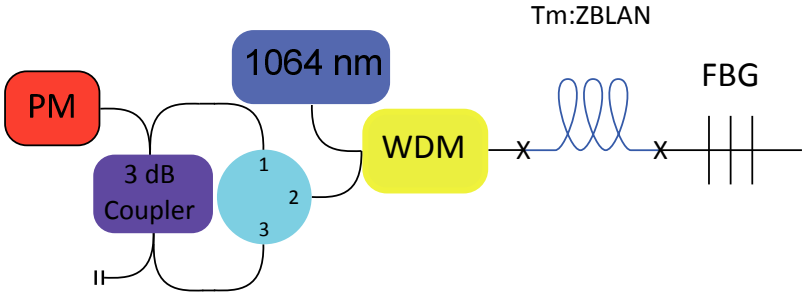

(a) Linear cavity laser configuration, with a 3 dB coupler and a circulator serving for signal reinjection and output coupling.

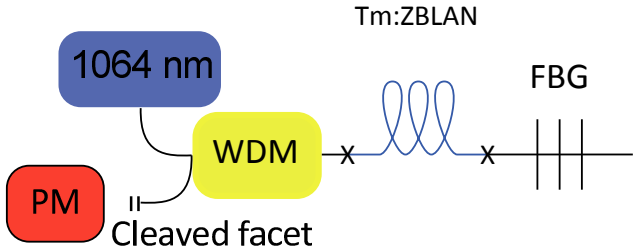

(b) Linear cavity laser configuration, with a cleaved facet serving for reinjection and output coupling.

Figure 5–13: Linear cavity laser configurations.

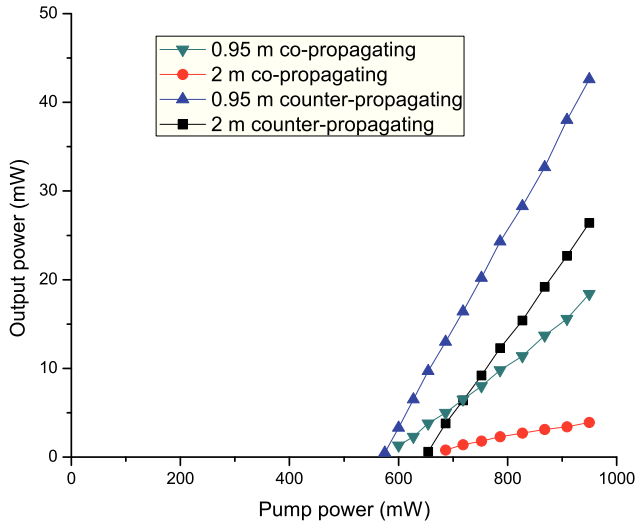

Figure 5–14: Output power obtained with the ring cavity laser.

5.4.3 Linear Cavity Lasers

Lengths of 40 cm and 95 cm of Tm:ZBLAN fibre were used in the linear cavity configurations. The FBG reflection wavelength was 1476 nm. In configuration 5–13a, the thresholds were 270 mW for the 40 cm length and 350 mW for the 95 cm. The efficiencies were measured to be 7.9 percent and 5.9 percent for both lengths, respectively. In configuration 5–13b, which provides 4% reflection back into the cavity through Fresnel reflection, the thresholds were higher in value. They were 750 mW and 500 mW for 40 cm and 95 cm lengths of Tm:ZBLAN fibre, respectively. We can observe that the thresholds decrease for the designs with higher reflection at the output coupler, as the total cavity loss is decreased. The 4% reflection shows a

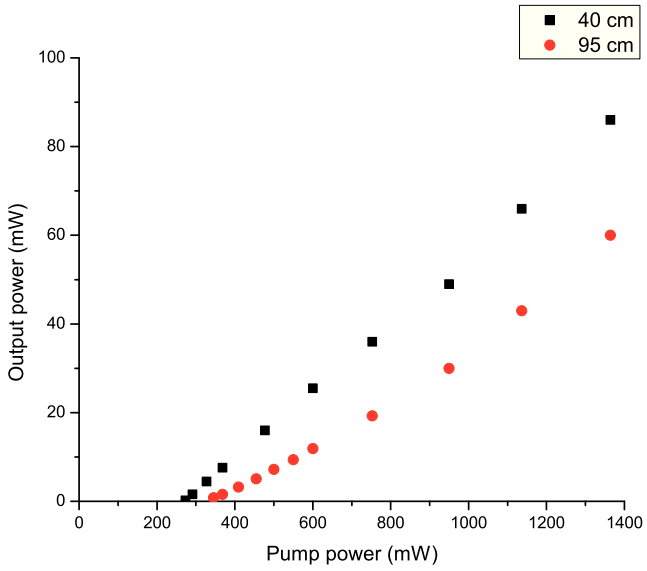

(a) Output power obtained with the linear cavity laser using a 3 dB coupler.

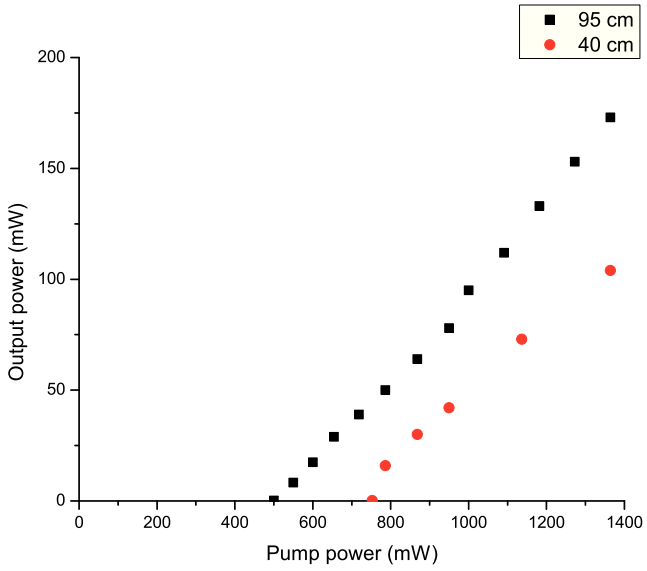

(b) Output power obtained with the linear cavity laser with a cleaved facet.

Figure 5–15: Output power obtained with the linear cavity lasers.

higher efficiency than the 50% reflection, which shows that the optimal reflection is lower than 50%. The output power graphs are shown in Fig. 5–15.

5.4.4 Optimized Linear Cavity Laser

A low loss design has been attempted, using the configuration shown in Fig. 5–16, to optimize the output power of the fibre laser. The FBG reflection wavelength was 1476 nm. The TM:ZBLAN fibre was pumped through the FBG rather than the WDM, to minimize insertion loss. The common port of the WDM was cut and cleaved to bypass the APC. It was then directly mechanically spliced to a 40 cm length of Tm:ZBLAN fibre. The signal port of the WDM was also cut and cleaved to bypass the APC, and the resulting facet was used as a low-reflectivity mirror and output coupler. With this configuration, a threshold power of 350 mW was achieved. A maximum P_{signal} = 340 mW was obtained for P_{pump} = 1360 mW. The slope efficiency was 40%. The output power graph is shown in Fig. 5–17.

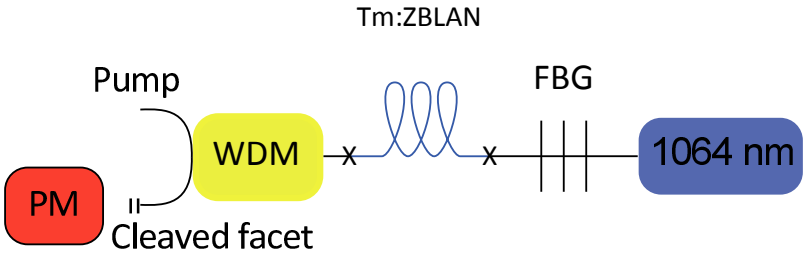

Figure 5–16: Optimized laser configuration used to optimize the output power.

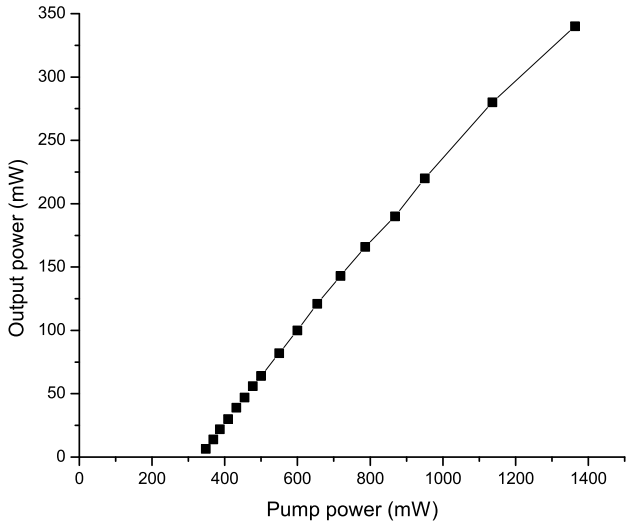

Figure 5–17: Output power graphs of the optimized linear cavity laser configuration.

5.4.5 Summary

The characteristics of all the above-mentioned designs are summarized in Table 5–1.

Table 5–1: Output characteristics of the various S-band lasers that have been tested.

Configuration	Fibre length (cm)	Threshold power (mW)	Slope efficiency (%)	Max P_{pump} (mW)	Max P_{signal} (mW)
RCL, co-prop.	95	600	5.3	950	18.4
RCL, co-prop.	200	690	1.47	950	3.9
RCL, counter-prop.	95	575	11.4	950	43
RCL, counter-prop.	200	655	9	950	26
LCL (3 dB coupler)	40	270	7.9	1360	86
LCL (3 dB coupler)	95	760	5.9	1360	60
LCL (cleaved facet)	40	750	16.9	1360	104
LCL (cleaved facet)	95	500	20	1360	173
LCL (optimized)	40	765	40	1360	340

5.5 Dual-Wavelength Lasing

5.5.1 Methodology

Dual-wavelength lasing in the S-band has been achieved with two pairs of wavelength: 1476/1487 nm, and 1487/1487.6 nm. In all cases, a linear cavity using a combination of 3 dB coupler and circulator was used at one end of the cavity to provide both reflection and output coupling. Output powers were measured with an OSA.

Gain competition was a greater obstacle when the wavelength separation was 0.6 nm than it was for 11 nm. Bi-directional pumping was necessary to achieve dual-wavelength with the smaller separation.

5.5.2 Dual-Wavelength Lasing at 1476 nm and 1487 nm

Dual-wavelength lasing has been achieved with cacaded cavity designs, shown in Fig. 5–18. In Fig. 5–18a, L_1 provided gain only for 1476 nm while L_2 provided gain for both wavelength. L_1 was first excited by the pump, and as P_{pump} was gradually increased, the leftover pump power would also excite L_2. The output power, while P_{pump} was gradually increased, is shown as a function of P_{pump} in Fig. 5–19a. The spectrum for P_{pump} = 1950 mW is shown in Fig. 5–19b.

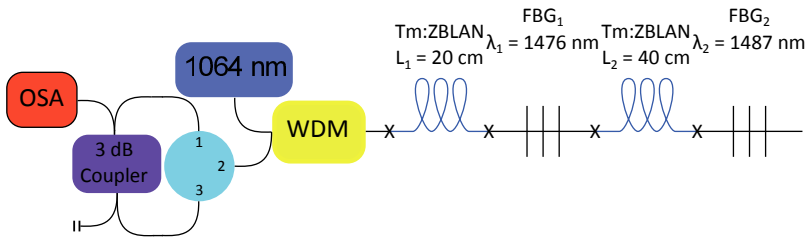

(a) Configuration with 20 cm and 40 cm lengths of Tm:ZBLAN fibre.

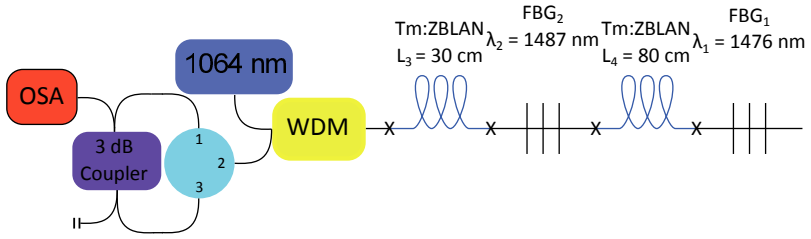

(b) Configuration with 30 cm and 80 cm lengths of Tm:ZBLAN fibre.

Figure 5–18: S-band cascaded cavity dual-wavelength configurations.

In Fig. 5–18b, L_3, which was the first length of fibre to be excited at lower values of P_{pump}, provided gain only for 1487 nm. L_4 provided gain for both wavelengths.

The hysteresis behaviour of config. 5–18b can be seen in Fig. 5–20. The power values have been measured with an OSA. The points shown in blue and green are expressed in arbitrary units, as the laser device's output connector has been slightly pulled away from the OSA input connector, in such a way as to limit the input of power into the OSA and avoid damaging it.

The values shown were all measured in one instance with constant distance between both connectors. They are proportional to the power value measured in dBm. The alignment between the left and right parts of the graphs is arbitrary. P_{pump} was gradually increased from 0 mW to 1950 mW and then decreased back to 0 mW in one instance.

The hysteresis in the behaviour of the laser is limited. One does not see a qualitative change in behaviour between the P_{pump} increase and its decrease. The maximum total power that has been measured was 75 mW at 1650 mW of pump power. The signal powers were 12 mW and 63 mW for 1476 nm and 1487 nm, respectively.

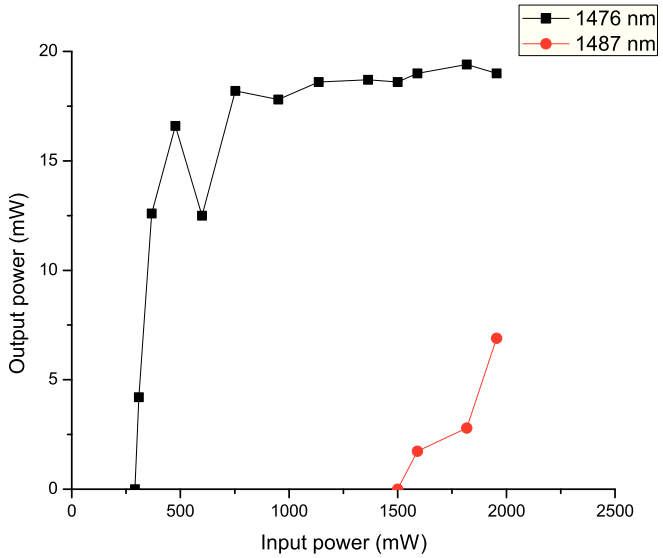

(a) Output powers from the laser in config. 5–18a.

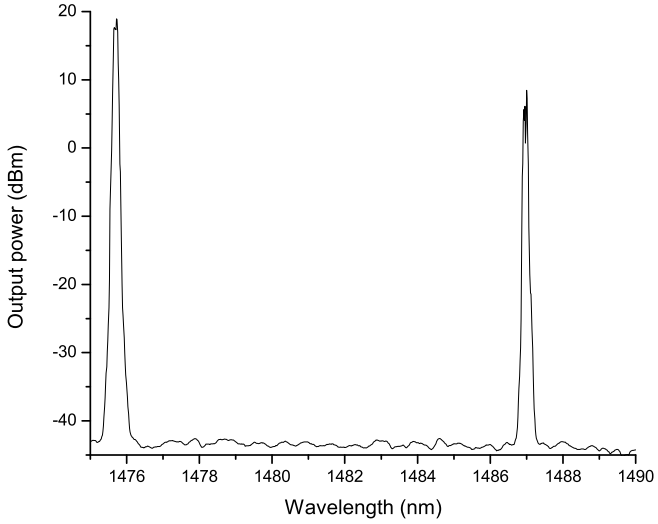

(b) Output spectrum of the dual-wavelength laser of config. 5–18a when P_{pump} = 1950 mW

Figure 5–19: Output power and spectrum of the S-Band cascaded cavity laser configuration shown in Fig. 5–18a.

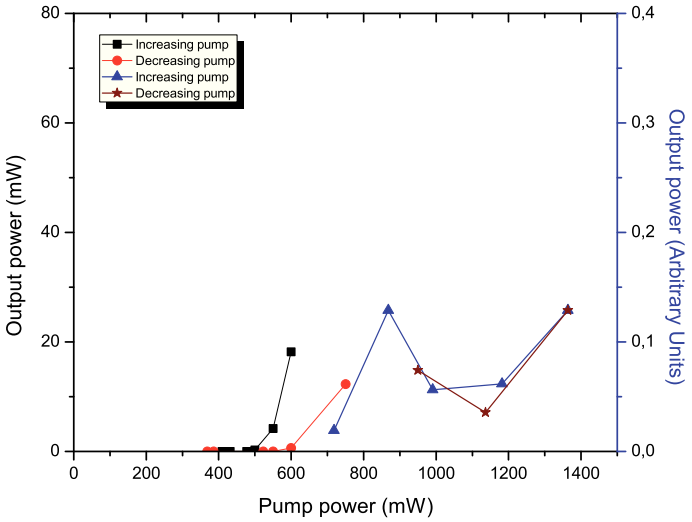

(a) Hysteresis behaviour for 1476 nm.

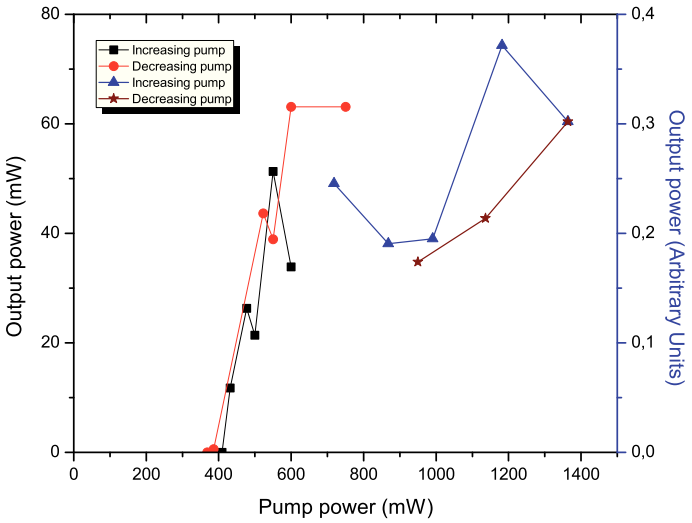

(b) Hysteresis behaviour for 1487 nm.

Figure 5–20: Hysteresis behaviour of the 5–18b configuration.

5.5.3 Dual-Wavelength Lasing at 1487 and 1487.6 nm

Dual-wavelength at 1487 nm and 1487.6 nm, using bidirectional pumping, has been achieved with the configuration shown in Fig. 5–21. In this section, pump powers will be indicated in the format P_{pump1}/P_{pump2} and output powers in the format $P_{1487}/P_{1487.6}$.

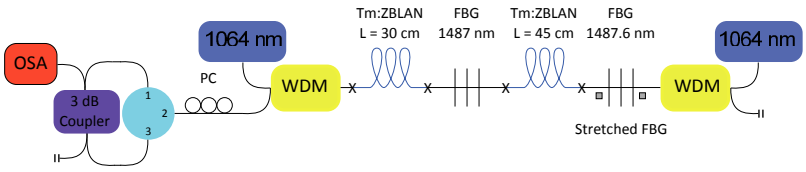

Figure 5–21: Setup for stretched FBG

Regions of Lasing

In Fig. 5–22, one can see which wavelengths are oscillating as a function of both pump powers. The region of interest has been scanned in a raster pattern, by increasing the input current of the second pump's laser diode by 0.2 A per step (~ 100 mW of pump), with fixed P_{pump1}. The input current of pump 1's laser diode was increased by 0.2 A and a new increasing scan of P_{pump2} values was made, until the whole range P_{pump} = 0/0 mW to 950/700 mW was covered. In the graph, black regions represent regions where no oscillation is observed, blue regions where only 1487 nm oscillates, red regions where only 1487.6 nm oscillates, and green regions represent simultaneous oscillation of both wavelength.

The spectrum at the lowest value of P_{pump1} where dual-wavelength lasing was achieved, which corresponds to the left tip of the green region on Fig. 5–22 is shown in Fig. 5–23a. In Fig. 5–23b, we can see the spectrum for the highest value of P_{pump1}, when P_{pump2} was adjusted to equalize both P_{signal} values as much

as possible. Fig. 5–23c shows the spectrum when both P_{pump} are maximized. Only 1487.6 nm can be seen to lase in this figure.

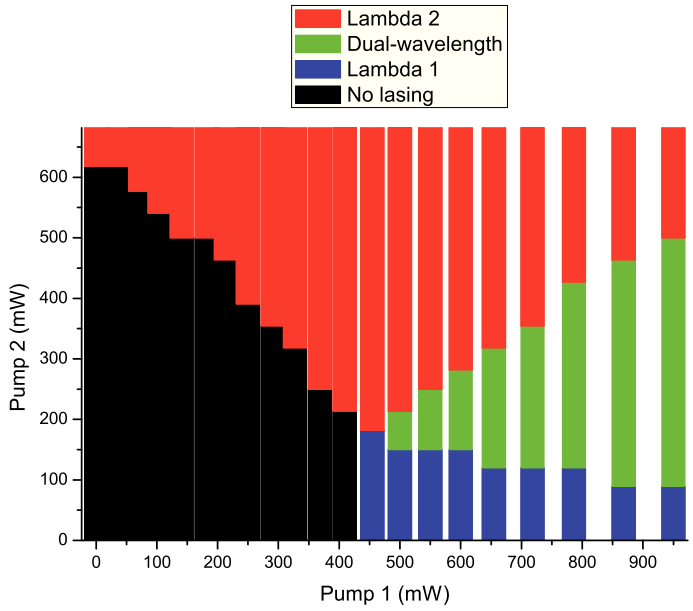

Figure 5–22: Regions of oscillations as a function of both pump powers.

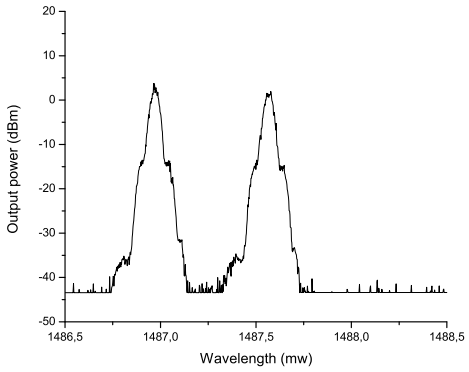

(a) Spectrum for P_{pump} = 500/200 mW.

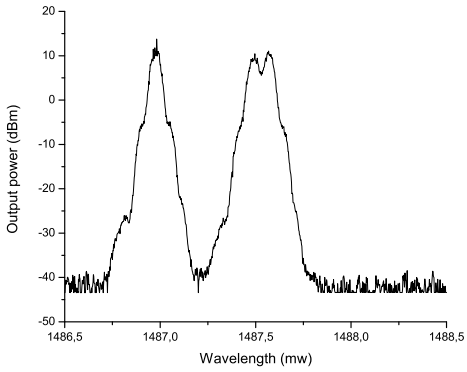

(b) Spectrum for P_{pump} = 950/340 mW.

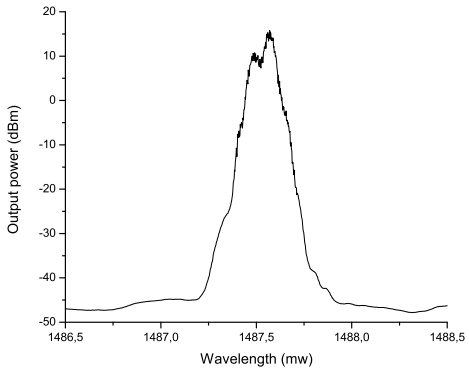

(c) Spectrum for P_{pump} = 950/700 mW.

Figure 5–23: Spectra measured during the first set of measurements done on config. 5–21

Pump Thresholds

Fig. 5–24 shows the thresholds between the different regions of lasing for config. 5–21, over the range P_{pump} = 0/0 mW to 2430/2050 mW. Short refers to 1487 nm and long to 1487.6 nm.

The border between lasing at 1487 nm and dual-wavelength lasing was first measured by decreasing P_{pump1}. The border between no lasing and lasing at 1487.6 nm was then measured by decreasing P_{pump1}. The next step was measuring the border between 1487.6 nm and dual operation by decreasing P_{pump1}. After that, the border between no lasing and lasing at 1487 nm was measured by increasing P_{pump2}. With P_{pump1} = 2430 mW, P_{pump2} was increased by increment of 0.5 A (~ 250 mW). The last step was to decrease P_{pump1} by increment of 0.5 A when P_{pump2} was kept at 2050 mW.

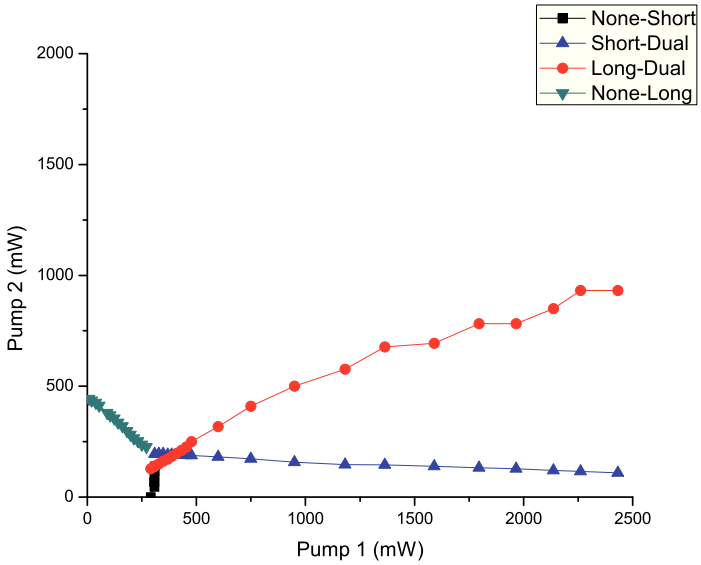

Figure 5–24: Observed thresholds for the laser configuration shown in Fig. 5–21

Three spectra obtained during the second set of measurements are shown in Fig. 5–25. In Fig. 5–25a, we see the spectrum observed at the lowest P_{pump1} value where dual-wavelength lasing is achieved. Fig. 5–25b shows the spectrum when P_{pump1} is increased to 2140 mW from the previous value. Fig. 5–25c shows the spectrum where both values of P_{pump} are maximized.

Excitation Dynamics

In both sets of measurements, we can see a qualitatively similar behaviour. If one increases P_{pump2} enough to achieve lasing at 1487.6 nm, and then increases P_{pump1}, dual-wavelength operation is achieved. When P_{pump2} is very high, the highest P_{pump1} value has failed to achieve lasing, as the longest piece of Tm:ZBLAN

fibre provides so much gain at 1487.6 nm that it inhibits lasing at 1487 nm through gain competition.

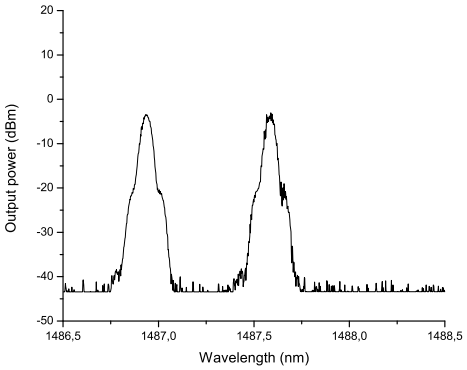

(a) Spectrum for P_{pump} = 410/140 mW.

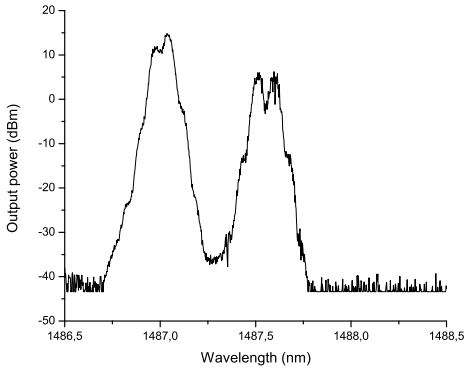

(b) Spectrum for P_{pump} = 2140/140 mW.

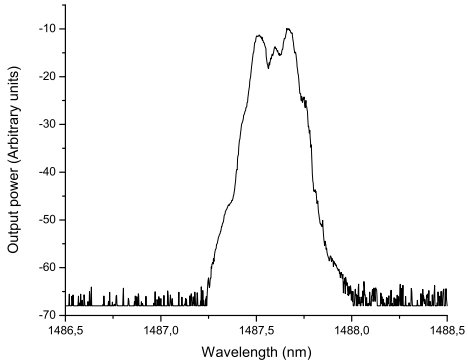

(c) Spectrum for P_{pump} = 2430/2050 mW.

Figure 5–25: Spectra measured during the second set of measurements done with the cascaded cavity configuration at 1487 and 1487.6 nm

Spectra measured during the second set of measurements done on config. 5–21

When P_{pump1} is increased enough to achieve lasing at 1487 nm, and then P_{pump2} is increased, dual-wavelength is first achieved. For higher values of P_{pump2}, lasing at 1487 nm is eventually inhibited by gain competition. Higher values of P_{pump1} both decrease the dual-wavelength threshold and the extinction threshold of 1487 nm, with respect to P_{pump2}.

On the one hand, pump leftover from the short fibre excites the long fibre, making it easier to achieve lasing conditions for 1487.6 nm. On the other hand, a higher P_{pump1} value means the short length of fibre is more excited, and therefore provides more gain only for 1487 nm, making it more resilient to gain competition.

5.6 Conclusion

In this chapter, the amplification of various lengths of Tm:ZBLAN fibre pumped at 1064 nm has been studied. Comparison between the lengths cannot be made since the loss induced by mechanical splices was uncontrollable. The characteristics of the gain, with respect to wavelength and pump power, was consistent with the theory explaining gain through the $^3H_4 \rightarrow {}^3H_6$ transition, for $P_{signal} > -40$ dBm.

Single wavelength lasing has been achieved at 1487 nm in a ring cavity laser, and at 1476 nm in a linear cavity laser. An optimized configuration, where loss was minimized, was tested and 340 mW of output at 1476 nm was obtained for a $P_{pump} = 1360$ mW.

Dual-wavelength lasing was demonstrated for two pairs of wavelengths: 1476/1487 nm and 1487/1487.6 nm. In both cases, cascaded cavities were used. Weak hysteresis was observed for the 1476/1487 nm pair. Lasing at 1487/1487.6 nm

was more difficult to achieve due to gain competition. Bidirectional pumping was used to control precisely the amount of excitation in both lengths of Tm:ZBLAN fibre. The behaviour as a function of these two pump powers was recorded and presented in this work.

CHAPTER 6
Conclusion and Future Work

This thesis has presented several fibre laser designs with Tm:ZBLAN fibre as the gain medium. In chapter 2, a theoretical background is established. The properties of glass hosts and how they affect ion dopant particles are described. The advantages of ZBLAN fibres, in particular the low phonon energy, which is necessary for lasing at both 810 nm and 1480 nm with Tm^{3+} ions. The lasing transitions and pumping schemes of four ions, Er^{3+}, Tm^{3+}, Nd^{3+} and Yb^{3+}, have been presented.

In chapter 3, the writing methods of FBGs have been explained. The properties of four materials used in fibre fabrication, silica, ZBLAN, chalcogenides and tellurites, have been exposed. This was followed by a comparison between the fibre fabrication methods of the most commonly used material, silica, and the material used to frabricate the fibres that were investigated in this thesis, ZBLAN, which underlined the difficulty in fabricating ZBLAN fibres.

In chapter 4, the ASE spectra from two lengths of Tm:ZBLAN fibres, one pumped at 790 nm and the other at 1064 nm, have been shown. The challenges of measuring the laser output without a WDM coupler to separate the signal and pump wavelengths are explained. Single-wavelength lasing at 810 nm with a single cavity configuration has been achieved and the results were presented. Dual-wavelength lasing at 805 nm and 810 nm, with both a single-cavity and a

cascaded cavity configurations has been demonstrated. The cascaded cavity was shown to have less hysteresis in its behaviour.

Further investigation, involving Tm:ZBLAN fibre that is optimized for operation at 810 nm rather than 1480 nm, would improve performance. The MFD loss between the Tm:ZBLAN fibre and FBG would be reduced. The fibre that was used could support more than one mode at 810 nm; further work may involve investigating the spatial modal properties of the laser's output. Use of a 800/1064 nm coupler would allow more different configurations wot be used and tested.

In chapter 5, the gain of several lengths of fibre in amplification configuration was presented. The uncontrollable loss of the mechanical splices prohibited comparison between the various lengths. The variations in gain, relative to the P_{pump} and λ_{signal}, were consistent with the theory for the $^3H_4 \rightarrow {}^3H_6$ transition when $P_{signal} > -40$ dBm.

At 1487 nm, single wavelength lasing was demonstrated in a ring cavity laser, and at 1476 nm in a linear cavity laser. The linear cavity configuration has been optimized to reduce loss, and better performance was obtained.

Dual-wavelength operation was also demonstrated with cascaded cavities, for two pairs of wavelengths: 1476/1487 nm and 1487/1487.6 nm. Weak hysteresis was observed for the 1476/1487 nm pair. Gain competition made lasing at 1487/1487.6 nm more difficult, so bidirectional pumping was used to control the excitation of both fibres indvidally. The effect of both pumps on the laser's behaviour was presented.

Further research may involve dual-wavelength lasing involving two bands sharing the same upper level, such as 810 nm and 1480 nm, to see how gain competition affects the performance.

References

[1] M.-J. Li and D. Nolan, "Optical transmission fiber design evolution," *Lightwave Technology, Journal of*, vol. 26, no. 9, pp. 1079–1092, May 2008.

[2] R. Zallen, *The Physics of Amorphous Solids*, ser. Physics textbook. John Wiley & Sons, 1998.

[3] N. S. Hussain and J. D. Da Silva Santos, *Physics and Chemistry of Rare-Earth Ions Doped Glasses*, ser. Materials Science Foundations. Trans Tech Publications, 2008.

[4] J. H. V. Vleck, "The puzzle of rare-earth spectra in solids." *The Journal of Physical Chemistry*, vol. 41, no. 1, pp. 67–80, 1937.

[5] D. E. McCumber, "Einstein relation connecting broadband emission and absoprtion spectra," *Physical Review*.

[6] A. L. Tchougréeff and R. Dronskowski, "Nephelauxetic effect revisited," *International Journal of Quantum Chemistry*, vol. 109, no. 11, pp. 2606–2621, 2009.

[7] C. B. Layne, W. H. Lowdermilk, and M. J. Weber, "Multiphonon relaxation of rare-earth ions in oxide glasses," *Phys. Rev. B*, vol. 16, pp. 10–20, Jul 1977. [Online]. Available: http://link.aps.org/doi/10.1103/PhysRevB.16.10

[8] B. M. Walsh and N. P. Barnes, "Comparison of Tm:ZBLAN and Tm:Silica fiber lasers; spectroscopy and tunable pulsed laser operation around 1.9 μm," *Applied Physics B: Lasers and Optics*, vol. 78, no. 3-4, pp. 325–333, 2004.

[9] P. Peterka, I. Kasik, A. Dhar, B. Dussardier, and W. Blanc, "Theoretical modeling of fiber laser at 810 nm based on thulium-doped silica fibers with enhanced $^3H_4$ level lifetime," *Optics Express*, vol. 19, no. 3, pp. 2773–2781, 2011.

[10] M. L. Dennis, J. W. Dixon, and I. Aggarwal, "High power upconversion lasing at 810 nm, in Tm:ZBLAN fibre," *Electronics Letters*, vol. 30, no. 2, pp. 136–137, Jan 1994.

[11] G. Androz, M. Bernier, D. Faucher, and R. Vallée, "2.3 W single transverse mode thulium-doped ZBLAN fiber laser at 1480 nm," *Optics Express*, vol. 16, no. 20, pp. 16 019–16 031, 2008.

[12] R. M. El-Agmy and N. M. Al-Hosiny, "2.31 μm laser under up-conversion pumping at 1.064 μm in Tm^{3+}:ZBLAN fibre lasers," *Electronics Letters*, vol. 46, no. 13, pp. 936–937, Jun 2010.

[13] R. Percival, S. Oliver, and R. Wyatt, "High-speed operation of an optically amplified system in the first telecommunications (800-850 nm) window," *Photonics Technology Letters, IEEE*, vol. 8, no. 7, pp. 956–958, Jul 1996.

[14] B. Cole and M. Dennis, "S-band amplification in a thulium doped silicate fiber," in *Optical Fiber Communication Conference and Exhibit, 2001. OFC 2001*, vol. 2, Mar. 2001, p. TuQ3.

[15] J. Stone and C. A. Burrus, "Neodymium-doped silica lasers in end-pumped fiber geometry," *Applied Physics Letters*, vol. 23, no. 7, pp. 388–389, 1973.

[16] J. Townsend, S. Poole, and D. Payne, "Solution-doping technique for fabrication of rare-earth-doped optical fibres," *Electronics Letters*, vol. 23, no. 7, pp. 329–331, Mar 1987.

[17] S. B. Poole, D. N. Payne, and M. E. Fermann, "Fabrication of low-loss optical fibres containing rare-earth ions," *Electronics Letters*, vol. 21, no. 17, pp. 737–738, Aug 1985.

[18] S. Poole, D. Payne, R. Mears, M. Fermann, and R. Laming, "Fabrication and characterization of low-loss optical fibers containing rare-earth ions," *Journal of Lightwave Technology*, vol. 4, no. 7, pp. 870–876, Jul 1986.

[19] W. J. Miniscalco, "Erbium-doped glasses for fiber amplifiers at 1500 nm," *Journal of Lightwave Technology*, vol. 9, no. 2, pp. 234–250, Feb 1991.

[20] R. J. Mears, L. Reekie, S. B. Poole, and D. N. Payne, "Low-threshold tunable CW and Q-switched fibre laser operating at 1.55 μm," *Electronics Letters*, vol. 22, no. 3, pp. 159–160, Jan 1986.

[21] W. H. Loh, B. N. Samson, L. Dong, G. J. Cowle, and K. Hsu, "High performance single frequency fiber grating-based erbium/ytterbium-codoped fiber lasers," *Journal of Lightwave Technology*, vol. 16, no. 1, pp. 114–118, Jan 1998.

[22] M. C. Brierley and P. W. France, "Continuous wave lasing at 2.7 μm in an erbium-doped fluorozirconate fibre," *Electronics Letters*, vol. 24, no. 15, pp. 935–937, Jul 1988.

[23] J. Schneider, D. Hauschild, C. Frerichs, and L. Wetenkamp, "Highly efficient Er^{3+}:Pr^{3+}-codoped CW fluorozirconate fiber laser operating at 2.7 μm," *International Journal of Infrared and Millimeter Waves*, vol. 15, no. 11, pp. 1907–1922, 1994.

[24] S. Bedö, M. Pollnau, W. Lüthy, and H. Weber, "Saturation of the 2.71 μm laser output in erbium-doped ZBLAN fibers," *Optics Communications*, vol. 116, no. 1-3, pp. 81–86, 1995.

[25] M. Pollnau, C. Ghisler, G. Bunea, M. Bunea, W. Lüthy, and H. P. Weber, "150 mw unsaturated output power at 3 μm from a single-mode-fiber erbium cascade laser," *Applied Physics Letters*, vol. 66, no. 26, pp. 3564–3566, 1995.

[26] R. G. Smart, J. N. Carter, D. C. Hanna, and A. C. Tropper, "Erbium doped fluorozirconate fibre laser operating at 1.66 and 1.72 μm," *Electronics Letters*, vol. 26, no. 10, pp. 649–651, May 1990.

[27] H. Tobben, "Room temperature CW fibre laser at 3.5 μm in Er^{3+}-doped ZBLAN glass," *Electronics Letters*, vol. 28, no. 14, pp. 1361–1362, Jul 1992.

[28] N. J. Vasa, S. Nagaoka, T. Okada, Y. Kubota, N. Nishimura, and T. Teshima, "Widely tunable Ce and Er codoped fluorozirconate fiber laser with 975 nm laser diode pumping," *Photonics Technology Letters, IEEE*, vol. 17, no. 4, pp. 759–761, Apr 2005.

[29] T. J. Whitley, C. A. Millar, R. Wyatt, M. C. Brierley, and D. Szebesta, "Upconversion pumped green lasing in erbium doped fluorozirconate fibre," *Electronics Letters*, vol. 27, no. 20, pp. 1785–1786, Sep 1991.

[30] S. Ferber, V. Gaebler, and H. J. Eichler, "Violet and blue upconversion-emission from erbium-doped ZBLAN-fibers with red diode laser pumping," *Optical Materials*, vol. 20, no. 3, pp. 211–215, 2002.

[31] T. S. McComb, R. A. Sims, C. C. C. Willis, P. Kadwani, L. Shah, and M. Richardson, "Atmospheric transmission testing using a portable, tunable, high power thulium fiber laser system," in *Conference on Lasers and Electro-Optics (CLEO) and Quantum Electronics and Laser Science Conference (QELS)*, May 2010, pp. 1 –2.

[32] X. Zhu and N. Peyghambarian, "High-power ZBLAN glass fiber lasers: Review and prospect," *Advances in OptoElectronics*, vol. 2010, 2010.

[33] R. Allen and L. Esterowitz, "CW diode pumped 2.3 μm fiber laser," *Applied Physics Letters*, vol. 55, no. 8, pp. 721–722, Aug 1989.

[34] R. Percival, S. Carter, D. Szebesta, S. Davey, and W. Stallard, "Thulium-doped monomode fluoride fibre laser broadly tunable from 2.25 to 2.5 μm," *Electronics Letters*, vol. 27, no. 21, pp. 1912–1913, Oct 1991.

[35] R. Percival, D. Szebesta, and S. Davey, "Highly efficient CW cascade operation of 1.47 and 1.82 μm transitions in Tm-doped fluoride fibre laser," *Electronics Letters*, vol. 28, no. 20, pp. 1866–1868, Sep 1992.

[36] R. Percival, D. Szebesta, and J. Williams, "Highly efficient 1.064 μm up-conversion pumped 1.47 μm thulium doped fluoride fibre laser," *Electronics Letters*, vol. 30, no. 13, pp. 1057–1058, Jun 1994.

[37] S. Sanders, R. G. Waarts, D. G. Mehuys, and D. F. Welch, "Laser diode pumped 106 mw blue upconversion fiber laser," *Applied Physics Letters*, vol. 67, no. 13, pp. 1815–1817, 1995.

[38] M. P. L. Flohic, J. Y. Allain, G. M. Stéphan, and G. Mazé, "Room-temperature continuous-wave upconversion laser at 455 nm in a Tm^{3+} fluorozirconate fiber," *Opt. Lett.*, vol. 19, no. 23, pp. 1982–1984, Dec 1994.

[39] R. M. El-Agmy, "Upconversion CW laser at 284 nm in a Nd:YAG-pumped double-cladding thulium-doped ZBLAN fiber laser," *Laser Physics*, vol. 18, no. 6, pp. 803–806, 2008.

[40] J. Stone and C. Burrus, "Neodymium-doped fiber lasers: Room temperature CW operation with an injection laser pump," *IEEE Journal of Quantum Electronics*, vol. 10, no. 9, p. 794, Sep 1974.

[41] M. C. Brierley and P. W. France, "Neodymium-doped fluoro-zirconate fibre laser," *Electronics Letters*, vol. 23, no. 16, pp. 815–817, Jul 1987.

[42] T. Komukai, Y. Fukasaku, T. Sugawa, and Y. Miyajima, "Highly efficient and tunable Nd^{3+} doped fluoride fibre laser operating in 1.3 μm band," *Electronics Letters*, vol. 29, no. 9, pp. 755–757, Apr 1993.

[43] D. S. Funk, J. W. Carlson, and J. G. Eden, "Ultraviolet (381 nm), room temperature laser in neodymium-doped fluorozirconate fibre," *Electronics Letters*, vol. 30, no. 22, pp. 1859–1860, Oct 1994.

[44] ——, "Room-temperature fluorozirconate glass fiber laser in the violet (412 nm)," *Opt. Lett.*, vol. 20, no. 13, pp. 1474–1476, Jul 1995.

[45] J. Y. Allain, M. Monerie, and H. Poignant, "Ytterbium-doped fluoride fibre laser operating at 1.02 μm," *Electronics Letters*, vol. 28, no. 11, pp. 988–989, May 1992.

[46] K. O. Hill, Y. Fujii, D. C. Johnson, and B. S. Kawasaki, "Photosensitivity in optical fiber waveguides: Application to reflection filter fabrication," *Applied Physics Letters*, vol. 32, no. 10, pp. 647–649, May 1978.

[47] D. K. W. Lam and B. K. Garside, "Characterization of single-mode optical fiber filters," *Appl. Opt.*, vol. 20, no. 3, pp. 440–445, Feb 1981.

[48] K. Hill and G. Meltz, "Fiber Bragg grating technology fundamentals and overview," *Journal of Lightwave Technology*, vol. 15, no. 8, pp. 1263–1276, Aug 1997.

[49] J. Canning, "Fibre gratings and devices for sensors and lasers," *Laser and Photonics Reviews*, vol. 2, no. 4, pp. 275–289, 2008.

[50] T. Erdogan, V. Mizrahi, P. J. Lemaire, and D. Monroe, "Decay of ultraviolet-induced fiber Bragg gratings," *Journal of Applied Physics*, vol. 76, no. 1, pp. 73–80, Jul 1994.

[51] G. Meltz, W. W. Morey, and W. H. Glenn, "Formation of Bragg gratings in optical fibers by a transverse holographic method," *Opt. Lett.*, vol. 14, no. 15, pp. 823–825, Aug 1989.

[52] M. Matsuhara and K. O. Hill, "Optical-waveguide band-rejection filters: Design," *Appl. Opt.*, vol. 13, no. 12, pp. 2886–2888, Dec 1974.

[53] J. A. R. Williams, I. Bennion, K. Sugden, and N. J. Doran, "Fibre dispersion compensation using a chirped in-fibre Bragg grating," *Electronics Letters*, vol. 30, no. 12, pp. 985–987, Jun 1994.

[54] L. Skuja, "Optically active oxygen-deficiency-related centers in amorphous silicon dioxide," *Journal of Non-Crystalline Solids*, vol. 239, no. 1-3, pp. 16–48, 1998.

[55] C. G. Askins, T.-E. Tsai, G. M. Williams, M. A. Putnam, M. Bashkansky, and E. J. Friebele, "Fiber Bragg reflectors prepared by a single excimer pulse," *Opt. Lett.*, vol. 17, no. 11, pp. 833–835, Jun 1992.

[56] G. M. Williams, T. E. Tsai, C. I. Merzbacher, and E. J. Friebele, "Photosensitivity of rare-earth-doped zblan fluoride glasses," *Journal of Lightwave Technology*, vol. 15, no. 8, pp. 1357–1362, Aug 1997.

[57] M. Zeller, T. Lasser, H. G. Limberger, and G. Maze, "UV-induced index changes in undoped fluoride glass," *Journal of Lightwave Technology*, vol. 23, no. 2, pp. 624–627, Feb 2005.

[58] T. Taunay, P. Niey, P. Bernage, E. X. Xie, H. Poignant, S. Boj, E. Delevaque, and M. Monerie, "Ultraviolet-induced permanent Bragg gratings in cerium-doped ZBLAN glasses or optical fibers," *Optics Express*, vol. 19, no. 17, pp. 1269–1271, Sep 1994.

[59] M. Bernier, D. Faucher, R. Vallée, A. Saliminia, G. Androz, Y. Sheng, and S. L. Chin, "Bragg gratings photoinduced in ZBLAN fibers by femtosecond pulses at 800 nm," *Optics Letters*, vol. 32, no. 5, pp. 454–456, 2007.

[60] J. Sanghera and I. Aggarwal, *Infrared Fiber Optics*. CRC Press, 1998.

[61] L. G. Cohen, C. Lin, and W. G. French, "Tailoring zero chromatic dispersion into the 1.5-1.6 μm low-loss spectral region of single-mode fibres," *Electronics Letters*, vol. 15, no. 12, pp. 334–335, Jul 1979.

[62] A. B. Seddon, Z. Tang, D. Furniss, S. Sujecki, and T. M. Benson, "Progress in rare-earth-doped mid-infrared fiber lasers," *Opt. Express*, vol. 18, no. 25, pp. 26 704–26 719, Dec 2010.

[63] H. Rawson, *Inorganic glass-forming systems*, ser. Non-metallic solids. Academic Press, 1967.

[64] M. Poulain, M. Poulain, and J. Lucas, "Verres fluorés au tetrafluorure de zirconium, propriétés optiques d'un verre dopé au Nd^{3+}," *Materials Research Bulletin*, vol. 10, no. 4, pp. 243–246, 1975.

[65] K. Ohsawa and T. Shibata, "Preparation and characterization of ZrF_4-BaF_2-LaF_3-NaF-AlF_3 glass optical fibers," *Journal of Lightwave Technology*, vol. 2, no. 5, pp. 602–606, Oct 1984.

[66] R. M. Almeida and J. D. Mackenzie, "Vibrational spectra and structure of fluorozirconate glasses," *The Journal of Chemical Physics*, vol. 74, no. 11, pp. 5954–5961, 1981.

[67] J. Lucas, "Fluoride glasses," *Journal of Materials Science*, vol. 24, no. 1, pp. 1–13, 1989.

[68] M. C. Gonçalves and R. M. Almeida, "Influence of the modifying cations on physical properties of fluorozirconate glasses," *Materials Research Bulletin*, vol. 31, no. 5, pp. 573–580, 1996.

[69] T. Kanamori and S. Sakaguchi, "Preparation of elevated NA fluoride optical fibers." *Japanese Journal of Applied Physics, Part 2: Letters*, vol. 25, no. 6, pp. 468–470, 1986.

[70] T. A. Fjeldly, A. Hordvik, and M. G. Drexhage, "Stability of IR transparent fluoride glasses in humid air studied by Auger electron spectroscopy," *Materials Research Bulletin*, vol. 19, no. 6, pp. 685–691, 1984.

[71] S. Mitachi and T. Miyashita, "Preparation of low-loss fluoride glass fibre," *Electronics Letters*, vol. 18, no. 4, pp. 170 –171, Feb 1982.

[72] Y. Ohishi, S. Mitachi, T. Kanamori, and T. Manabe, "Optical absorption of 3d transition metal and rare earth elements in zirconium fluoride glasses." *Physics and Chemistry of Glasses*, vol. 24, no. 5, pp. 135–140, 1983.

[73] P. W. France, S. F. Carter, and J. M. Parker, "Oxidation states of 3d transition metals in ZrF_4 glasses." *Physics and Chemistry of Glasses*, vol. 27, no. 1, pp. 32–41, 1986.

[74] A. M. Buswell, R. L. Maycock, and W. H. Rodebush, "Infra-red absorption studies X. the infra-red absorption of hydrogen fluoride in the vapor state and in solution in an inert solvent," *The Journal of Chemical Physics*, vol. 8, no. 5, pp. 362–365, 1940.

[75] B. G. Aitken and C. W. Ponader, "Physical properties and Raman spectroscopy of GeAs sulphide glasses," *Journal of Non-Crystalline Solids*, vol. 256 & 257, no. 0, pp. 143–148, 1999.

[76] V. Q. Nguyen, J. S. Sanghera, J. A. Freitas, I. D. Aggarwal, and I. K. Lloyd, "Structural investigation of chalcogenide and chalcohalide glasses using Raman spectroscopy," *Journal of Non-Crystalline Solids*, vol. 248, no. 2-3, pp. 103–114, 1999.

[77] H. H. Adler and K. P. F., "Variations in infrared spectra, molecular symmetry and site symmetry of sulfate minerals," *The American Mineralogist*, vol. 50, no. 1-2, pp. 132–147, Jan 1965.

[78] Z. Tang, N. C. Neate, D. Furniss, S. Sujecki, T. M. Benson, and A. B. Seddon, "Crystallization behavior of Dy^{3+}-doped selenide glasses," *Journal of Non-Crystalline Solids*, vol. 357, no. 11-13, pp. 2453–2462, 2011.

[79] J. Toulouse, A. Lin, A. Ryaznyanskiy, A. Belwalkar, C. Guintrand, C. Lafontaine, W. Misiolek, and I. Biaggio, "Development of new tellurite fibers for mid-IR applications," in *Winter Topicals (WTM), 2011 IEEE*, Jan 2011, pp. 185–186.

[80] J. S. Wang, E. M. Vogel, and E. Snitzer, "Tellurite glass: a new candidate for fiber devices," *Optical Materials*, vol. 3, no. 3, pp. 187–203, 1994.

[81] G. Mazé, V. Cardin, and M. Poulain, "Low-OH^- absorption fluoride glass infra-red optical fibres," *Electronics Letters*, vol. 20, no. 21, pp. 884–885, Nov 1984.

[82] M. Robinson, R. C. Pastor, R. R. Turk, D. P. Devor, M. Braunstein, and R. Braunstein, "Infrared-transparent glasses derived from the fluorides of zirconium, thorium, and barium," *Materials Research Bulletin*, vol. 15, no. 6, pp. 735–742, 1980.

[83] M. Robinson and G. L. Tangonan, "Light scattering in fluoride glass," *Materials Research Bulletin*, vol. 23, no. 7, pp. 943–951, 1988.

[84] D. C. Tran and C. Fisher, "SF_6 process for dehydration of fluoride glasses," Patent US 4 539 032, Sep 03, 1985.

[85] T. Nakai, Y. Mimura, H. Tokiwa, and O. Shinbori, "Dehydration of fluoride glasses by NF_3 processing," *Lightwave Technology, Journal of*, vol. 4, no. 1, pp. 87–89, Jan 1986.

[86] S. Mitachi, S. Shibata, and T. Manabe, "Preparation of preforms for fluoride glass fibers," *Japanese Journal of Applied Physics*, vol. 20, no. 5, pp. L337–L339, 1981.

[87] S. Mitachi, T. Miyashita, and T. Kanamori, "Fluoride-glass-cladded optical fibres for mid-infrared ray transmission," *Electronics Letters*, vol. 17, no. 17, pp. 591–592, Aug 1981.

[88] D. Tran, C. Fisher, and G. Sigel, "Fluoride glass preforms prepared by a rotational casting process," *Electronics Letters*, vol. 18, no. 15, pp. 657–658, Jul 1982.

[89] S. Sakaguchi and S. Takahashi, "Low-loss fluoride optical fibers for midinfrared optical communication," *Journal of Lightwave Technology*, vol. 5, no. 9, pp. 1219–1228, Sep 1987.

[90] Y. Ohishi, S. Sakaguchi, and S. Takahashi, "Transmission loss characteristics of fluoride glass single-mode fibre," *Electronics Letters*, vol. 22, no. 20, pp. 1034 –1035, Sep 1986.

[91] H. Tokiwa, Y. Mimura, T. Nakai, and O. Shinbori, "Fabrication of long single-mode and multimode fluoride glass fibres by the double-crucible technique," *Electronics Letters*, vol. 21, no. 24, pp. 1131 –1132, Nov 1985.

[92] R. Smart, A. Tropper, D. Hanna, J. Carter, S. Davey, S. Carter, and D. Szebesta, "High efficiency, low threshold amplification and lasing at 0.8 μm in monomode Tm^{3+}-doped fluorozirconate fibre," *Electronics Letters*, vol. 28, no. 1, pp. 58–59, Jan 1992.

[93] G. Qin, S. Huang, Y. Feng, A. Shirakawa, and K.-I. Ueda, "Multiple-wavelength up-conversion laser in Tm^{3+}-doped ZBLAN glass fiber," *Photonics Technology Letters, IEEE*, vol. 17, no. 9, pp. 1818–1820, Sep 2005.

[94] Z. Jing, P. Ramana, J. Chandrappan, T. C. Wei, C. Y. Yoon, T. W. Liang, J. Lau, P. Gomex, W. Ting, and V. Ramkumar, "Development of optical subassembly for plastic optical fiber in high speed applications," in *Electronics Packaging Technology Conference, 2008. EPTC 2008. 10th*, Dec 2008, pp. 1220–1225.

[95] J. Mateo, M. Losada, and A. Lopez, "Application of the plastic optical fibre in domestic multimedia networks," in *ICTON Mediterranean Winter Conference,2009. ICTON-MW 2009. 3rd*, Dec 2009, pp. 1–5.

[96] J. Blyler, L.L., "Plastic optical fiber technology for telecommunications," in *Optical Fiber Communication Conference and Exhibit, 1998. OFC '98., Technical Digest*, Feb 1998, pp. 306–307.

[97] D. Dragoman and M. Dragoman, "Terahertz fields and applications," *Progress in Quantum Electronics*, vol. 28, no. 1, pp. 1– 66, 2004.

[98] A. Maestrini, I. Mehdi, J. Siles, J. Ward, R. Lin, B. Thomas, C. Lee, J. Gill, G. Chattopadhyay, E. Schlecht, J. Pearson, and P. Siegel, "Design and characterization of a room temperature all-solid-state electronic source tunable from 2.48 to 2.75 THz," *Terahertz Science and Technology, IEEE Transactions on*, vol. 2, no. 2, pp. 177 –185, Mar. 2012.

[99] H. Tanoto, Q. Wu, J. Teng, M. Sun, Z. Chen, T. Htoo, S. Chua, J. Lampin, A. Gokarna, and E. Dogheche, "Continuous wave terahertz photomixer from low temperature grown GaAs with high carrier mobility," in *Infrared Millimeter and Terahertz Waves (IRMMW-THz), 2010 35th International Conference on*, Sep 2010, pp. 1 –2.

[100] M. Eichhorn, "Numerical modeling of tm-doped double-clad fluoride fiber amplifiers," *Quantum Electronics, IEEE Journal of*, vol. 41, no. 12, pp. 1574 – 1581, dec. 2005.

[101] D. Marcuse, "Loss analysis of single-mode fiber splices," vol. 56, no. 5, May 1977.

[102] Q. Mao and J. Lit, "Optical bistability in an L-band dual-wavelength erbium-doped fiber laser with overlapping cavities," *IEEE Photonics Technology Letters*, vol. 14, no. 9, pp. 1252–1254, Sep 2002.

[103] S. Aozasa, H. Masuda, I. Sakamoto, K. Shikano, and M. Shimizu, "Gain-shifted TDFA employing high concentration doping technique with high internal power conversion efficiency of 70pp. 361–363, Apr 2002.

[104] T. Tamaoka and S. Tanabe, "Comparison of gain characteristics of tm-doped fiber amplifier by different pumping schemes," in *Optical Fiber Communications Conference, 2003. OFC 2003*, march 2003, pp. 630 – 631 vol.2.

[105] T. Kasamatsu, Y. Yano, and T. Ono, "1.49- μm-band gain-shifted thulium-doped fiber amplifier for WDM transmission systems," *Journal of Lightwave Technology*, vol. 20, no. 10, pp. 1826–1838, Oct 2002.

[106] F. Roy, D. Bayart, and P. Baniel, "Novel pumping schemes for thulium doped fiber amplifier," in *Optical Fiber Communication Conference, 2000*, vol. 2, 2000, pp. 14 –16 vol.2.

[107] A. Gomes, M. Carvalho, M. Sundheimer, C. Bastos-Filho, J. Martins-Filho, M. Costa e Silva, J. von der Weid, and W. Margulis, "Characterization of efficient dual-wavelength (1050 + 800 nm) pumping scheme for thulium-doped fiber amplifiers," *Photonics Technology Letters, IEEE*, vol. 15, no. 2, pp. 200 –202, feb. 2003.

[108] T. Komukai, T. Yamamoto, T. Sugawa, and Y. Miyajima, "Upconversion pumped thulium-doped fluoride fiber amplifier and laser operating at 1.47 μm," *IEEE Journal of Quantum Electronics*, vol. 31, no. 11, pp. 1880–1889, Nov 1995.

[109] R. Allen, L. Esterowitz, and I. Aggarwal, "An efficient 1.46 μm thulium fiber laser via a cascade process," *IEEE Journal of Quantum Electronics*, vol. 29, no. 2, pp. 303–306, Feb 1993.

[110] D. Bayart, P. Baniel, A. Bergonzo, J.-Y. Boniort, P. Bousselet, L. Gasca, D. Hamoir, F. Leplingard, A. Le Sauze, P. Nouchi, F. Roy, and P. Sillard, "Broadband optical fibre amplification over 17.7 Thz range," *Electronics Letters*, vol. 36, no. 18, pp. 1569–1571, Aug 2000.

[111] A. Sharma, N. Singh, and S. Singh, "S-band distributed raman fiber amplifier," in *Recent Advances in Information Technology (RAIT), 2012 1st International Conference on*, Mar 2012, pp. 722–724.

[112] P. Watekar, S. Ju, and W.-T. Han, "Experimental realization of silica-glass tm-doped fiber amplifier with 11.3-dB gain," *Photonics Technology Letters, IEEE*, vol. 19, no. 19, pp. 1478–1480, Oct 2007.

[113] Y. Kimura and M. Nakazawa, "Gain characteristics of erbium-doped fibre amplifiers with high erbium concentration," *Electronics Letters*, vol. 28, no. 15, pp. 1420–1422, Jul 1992.

[114] J. Mangeney, A. Merigault, N. Zerounian, P. Crozat, K. Blary, and J. F. Lampin, "Continuous wave terahertz generation up to 2 Thz by photomixing on ion-irradiated $In_{0.53}Ga_{0.47}As$ at 1.55 μm wavelengths," *Applied Physics Letters*, vol. 91, no. 24, p. 241102, 2007.

[115] R. Percival, D. Szebesta, C. Seltzer, S. Perin, S. Davey, and M. Louka, "A 1.6 μm pumped 1.9-μm thulium-doped fluoride fiber laser and amplifier of very high efficiency," *IEEE Journal of Quantum Electronics*, vol. 31, no. 3, pp. 489–493, Mar 1995.